THESIS

PREDICTION OF TOTAL LIGHTNING IN COLORADO AND ALABAMA THUNDERSTORMS BASED ON STORM DYNAMICAL AND MICROPHYSICAL VARIABLES

Submitted by

Brett Michael Basarab

Department of Atmospheric Science

In partial fulfillment of the requirements

For the Degree of Master of Science

Colorado State University

Fort Collins, Colorado

Spring 2015

Master's Committee:

Advisor: Steven Rutledge

Wiebke Deierling
Sonia Kreidenweis
Steven Reising

ABSTRACT

PREDICTION OF TOTAL LIGHTNING IN COLORADO AND ALABAMA THUNDERSTORMS BASED ON STORM DYNAMICAL AND MICROPHYSICAL VARIABLES

Thunderstorms impact their environment in a variety of ways, including the production of nitrogen oxides (NO_x) by lightning (LNO_x). Accurate prediction of total lightning flash rate in thunderstorms is important to improve estimates of LNO_x from the storm scale to the global scale. New flash rate parameterization schemes have been developed based on observed relationships between lightning flash rate and storm parameters for Colorado thunderstorms during the Deep Convective Clouds and Chemistry (DC3) experiment. Storm total flash rates are determined using an automated flash counting algorithm that clusters very high frequency (VHF) radiation sources emitted by electrical breakdown in clouds and detected by the northern Colorado lightning mapping array (LMA). Storm parameters such as hydrometeor echo volumes and ice masses are calculated from polarimetric radar retrievals. Measurements of updraft strength are obtained by synthesizing radial velocity retrievals from the CSU-CHILL and CSU-Pawnee radars to determine three-dimensional wind fields.

Bulk storm parameters including the graupel echo volume, 30-dBZ echo volume, and precipitating ice mass are found to be robustly correlated to flash rate ($R^2 \sim 0.8$). It is shown that simple flash rate parameterization schemes based on these quantities predict gross flash rate behavior reasonably well. Updraft intensity-based flash rate schemes are also developed, but updraft parameters were not as strongly correlated to flash rate as storm volume quantities. The use of multiple storm parameters to predict flash rate is also investigated, since flash rate may be sensitive to multiple processes or characteristics within thunderstorms. A simple approach is found to be most

effective: graupel and reflectivity echo volumes were split up into representative area and height dimensions and regressed against flash rate. The combined quantities predict flash rate variability somewhat better than simpler single-parameter flash rate schemes. All new flash rate schemes are tested against observations of Alabama thunderstorms documented during DC3 to examine their potential regional limitations. The flash rate schemes developed work best for strong Colorado storms with sustained high flash rates. Finally, relationships between total flash rate and flash size are discussed, with implications for the improved prediction of LNO_x.

ACKNOWLEDGMENTS

My advisor, Dr. Steven Rutledge, deserves the greatest thanks for his unwavering support throughout this research. Dr. Rutledge has fostered my growth as a researcher while being supportive of me as a graduate student. I thank the members of my master's committee, Dr. Wiebke Deierling, Dr. Sonia Kreidenweis, and Dr. Steven Reising for the time they have taken to review and improve this thesis.

Brody Fuchs of the CSU Radar Meteorology group deserves special thanks for his development and willingness to share analysis software that proved essential to carry out this study. I am also grateful to Paul Hein for assistance with software and programming issues throughout this work. Paul's patience and enthusiasm in answering my many questions is admirable. Dr. Brenda Dolan of the Radar group and Pat Kennedy of the CSU-CHILL radar facility provided invaluable suggestions and assistance with the processing of the radar data. Pat was also responsible for providing the Colorado radar data used in this study. Other current and past members of the Radar group have been crucial sources of support and motivation: thank you to Doug Stolz, Liz Thompson, Alyssa Matthews, Dr. Weixin Xu, and Nick Beavis.

I would also like to thank several collaborators who have been strongly invested in this work and have provided many interesting discussions and suggestions for improvement: Dr. Mary Barth, Dr. Wiebke Deierling, Dr. Ken Pickering, Dr. Larry Carey, Retha Matthee, Kristin Cummings, and Dr. Eric Bruning. Finally, friends and family have been incredibly supportive of my passion for atmospheric science and my decision to pursue it as a career. For that I will always be grateful.

Alabama radar and lightning data were provided by Retha Matthee, Lamont Bain, and Dr. Larry Carey of the University of Alabama, Huntsville. This research was supported by the National Science Foundation under grant AGS-1010657.

TABLE OF CONTENTS

LIST OF TABLES

LIST OF FIGURES

CHAPTER 1

INTRODUCTION

Thunderstorms strongly impact their environment and play an important role in global climate. In recent years, one of the most well studied effects of thunderstorms has been the production of nitrogen oxides (NO + NO_2 = NO_x) by lightning and subsequent transport of NO_x to the upper troposphere (Pickering et al. 1998; DeCaria et al. 2000; Dye et al. 2000; Fehr et al. 2004; DeCaria et al. 2005; Schumann and Huntrieser 2007; Zhao et al. 2009; Jourdain et al. 2010; Ott et al. 2010; Cummings et al. 2013). NO_x exerts a significant control on the ozone (O_3) content in the atmosphere; a localized increase in NO_x in the upper troposphere, where initial NO_x concentrations are low, can lead to net O_3 production (Liu et al. 1987; Pickering et al. 1990; Seinfeld and Pandis 2006). Ozone functions effectively as a greenhouse gas in the upper troposphere, where its absorption of upwelling longwave radiation is most important (Schumann and Huntrieser 2007). Since surface dry bulb temperature has been found to correlate positively to lightning activity (Williams 1994; Williams et al. 2005), an increase in lightning in a warmer climate (due to an increase in thunderstorm intensity or frequency) is possible (Toumi et al. 1996; Williams 2005). The increase in lightning could drive a positive climate feedback to the warming as lightning NO_x production (LNO_x) increases. For this reason, accurate estimates of LNO_x are essential. Accurate knowledge of lightning frequency in storms is one crucial component in estimating LNO_x.

1.1. PRODUCTION OF NITROGEN OXIDES BY LIGHTNING

NO_x is produced during a lightning discharge when temperatures in the lightning channel rise to tens of thousands of degrees Celsius, sufficient to break the chemical bonds of molecular oxygen and nitrogen (O_2 and N_2) (Rakov and Uman 2003). Some of the resulting atomic oxygen and

nitrogen recombines as NO_x. Although many studies have sought to constrain the contribution of lightning to the global NO_x budget (Schumann and Huntrieser (2007) and references therein), large uncertainty in LNO_x remains. The most commonly accepted best estimate for LNO_x is 5 $\pm$ 3 Tg Nitrogen mass per year (Schumann and Huntrieser 2007). Lightning is the largest source of NO_x in the upper troposphere, and with most estimates of total global NO_x emissions between 30 and 60 Tg yr^{-1}, the contribution of lightning to the global NO_x budget is significant (Schumann and Huntrieser 2007).

There are many factors leading to the large uncertainty in global LNO_x, perhaps most fundamentally the incomplete knowledge of total lightning flash rate within storms. Some past studies have indirectly estimated total flash rate by assuming a fixed ratio of intracloud (IC) to cloud-to-ground (CG) flashes (f_{IC}/f_{CG}, Boccippio et al. (2001)), since many lightning detection systems detect mostly CG flashes (e.g. Ridley et al. 2004). Cloud-resolving modeling studies investigating NO_x production by thunderstorms also typically prescribe a fixed ratio of NO_x produced by IC versus CG flashes (P_{IC}/P_{CG}). Earlier studies (e.g. Price et al. 1997; Pickering et al. 1998) assumed a P_{IC}/P_{CG} ratio of 0.1 based on arguments that IC flashes dissipated less energy and therefore produced less NO_x than CG flashes (Holmes et al. 1971). More recent studies have suggested that production of NO_x by IC flashes is comparable to production by CG flashes. In their model simulations of six thunderstorms, Ott et al. (2010) found that a mean P_{IC}/P_{CG} ratio of 0.93 best reproduced observations of NO_x vertical profiles following convection. Cummings et al. (2013) used a P_{IC}/P_{CG} ratio of one to reproduce airborne observations of NO_x mixing ratios in their simulation of a strong tropical thunderstorm. Finally, although most studies have assumed constant NO_x production by all flashes of a single type (IC or CG), it is uncertain whether NO_x production per flash varies due to the varying properties of individual IC or CG flashes. Some studies have assumed a

constant amount of NO_x produced per unit energy dissipated (e.g. Ott et al. 2010), and multiplied by an assumed constant value of total energy dissipated by each CG flash. However, laboratory evidence indicates that NO_x produced per unit flash channel length may be a more invariant quantity than NO_x produced per unit energy dissipated, and an additional strong dependence on ambient pressure may be important (Wang et al. 1998; DeCaria et al. 2005). These findings suggest that each individual flash may produce a different amount of NO_x, depending on its size and altitude within the storm. It should be evident that improving estimates of lightning flash frequency within storms is only one, albeit essential, component in reducing LNO_x uncertainty.

Given the recent evidence of near equal NO_x production by IC and CG flashes, this study focuses on estimating total (IC plus CG) lightning flash frequency (flash rate) within storms. Estimation of total lightning flash rate in models remains challenging due to the need to represent the processes leading to bulk charge separation and the eventual lightning discharge. These processes occur on the sub-molecular scale (Takahashi 1978; Baker and Dash 1994; Bruning et al. 2014) and are therefore impractical to represent explicitly, even in convection-resolving model simulations. Most models attempting to simulate total lightning instead rely on lightning flash rate *parameterization schemes*, whereby flash rates are predicted based on other macroscopic variables (*storm parameters*) predicted by the model, such as peak thunderstorm updraft speed (e.g. Pickering et al. 1998). Studies implementing explicit electrification schemes in models are comparatively less common (e.g. Fierro et al. 2013). Lightning parameterizations are typically derived empirically from observations of the correlation between lightning flash rate and storm parameters (e.g. Price and Rind 1992). Parameterization schemes have been implemented in a number of cloud-resolving chemistry simulations and have been tested in operational models as a lightning forecasting aid (e.g. McCaul et al. 2009).

1.2. PREVIOUS WORK TO PARAMETERIZE LIGHTNING ACTIVITY

Charge transfer in thunderstorms is thought to occur via the non-inductive charging mechanism (NIC) whereby riming ice hydrometeors (predominantly graupel, or soft hail particles) undergo rebounding collisions with small ice crystals, with the presence of sufficient quantities of supercooled liquid water (SLW) allowing for significant charge transfer to occur (Reynolds et al. 1957; Takahashi 1978; Jayaratne et al. 1983; Saunders et al. 1991; Williams et al. 1991). It is thought that a thin quasi-liquid layer (QLL) residing on the surface of colliding ice particles and containing a negative surface charge results in net negative charge transfer during collision from the particle containing the thicker QLL to the thinner QLL. The surface thermodynamic states of the colliding graupel and ice crystal determine which particle carries the thicker QLL (Baker et al. 1987; Williams et al. 1991; Baker and Dash 1994). Since ice hydrometeors are the dominant charge carriers, charging processes occur in the mixed-phase region of storms (defined herein as the region bounded by the $-5^{\circ}\mathrm{C}$ and $-40^{\circ}\mathrm{C}$ temperature levels), where both ice and SLW can coexist. The strong convective updrafts observed in thunderstorms supply the mixed-phase region with sufficient quantities of SLW and result in strong differential vertical motions and turbulence, promoting frequent collisions between ice particles (Bruning et al. 2014). The thunderstorm updraft lofts the smaller charged ice crystals to high levels, while oppositely charged large graupel particles slowly descend, creating distinct charge centers between which strong electric fields can develop. Electrical breakdown of air (i.e., lightning) typically occurs when the local electric field exceeds 300 kV m^{-1} (Rakov and Uman 2003). Non-inductive charging processes are represented in part by the idealized equation (Wallace and Hobbs 2006)

$$\frac{\partial Q}{\partial t} = \pi R^2 n_g n_i (V_{t,g} - V_{t,i}) q E, \tag{1.1}$$

where $\partial Q/\partial t$ is the rate of charge transfer (Coulombs s^{-1} m^{-3}), R is the radius of a graupel particle, n_g and n_i are the number concentrations of graupel particles and ice crystals, $V_{t,g}$ and $V_{t,i}$ are the terminal fall speeds of graupel and ice crystals, respectively, q is the assumed constant charge transferred per collision, and E is the collision efficiency between graupel and ice crystals. This equation describes the number of collisions and subsequent charge transfer that would occur as a graupel particle sweeps out a volume $\pi R^2(V_{t,g} - V_{t,i})$ per second as it falls. A successful electrification and lightning parameterization must account for the various microphysical and dynamical processes represented in Eq. 1.1. For this reason, macroscopic indicators of updraft intensity, amount of charge carriers (ice hydrometeors) in storms, and quantities related to the bulk separation of differently sized hydrometeors should be strong indicators of lightning activity (specifically, the charging rate and resulting frequency of lightning discharges).

Various studies have derived robust quantitative relationships between lightning flash rate and storm parameters implicitly representative of non-inductive charging processes. Price and Rind (1992) derived lightning parameterizations relating flash rate to thunderstorm cloud top height (H) and to the maximum thunderstorm updraft speed (W_{max}). Deierling and Petersen (2008) found strong relationships between total lightning flash rate and the volume of updraft greater than 5 m s^{-1} ($UV5$) and 10 m s^{-1} ($UV10$) for storms in northern Alabama and eastern Colorado. A somewhat weaker but still robust correlation was found between lightning flash rate and W_{max}. Linear correlation coefficients (r) between flash rate and W_{max} and $UV5$ were found to be 0.82 and 0.93, respectively. Deierling et al. (2008) developed empirical relationships between flash rate and the polarimetric radar-derived precipitating ice mass (graupel and hail, referred to herein as PIM) as well as the product of the upward flux of non-precipitating ice (ice crystals and aggregates) and downward flux of precipitating ice (P_{flux}). That study found these quantities to be especially

well correlated to flash rate (r = 0.94 and r = 0.96 for PIM and P_{flux}, respectively). Carey and Rutledge (1996) noted a correlation between intracloud flash rate and graupel echo volume for a multi-cell thunderstorm in Colorado. In their study of a severe supercell thunderstorm observed during the Severe Thunderstorm Electrification and Precipitation Study (STEPS) campaign, Wiens et al. (2005) reported a strong correlation between graupel echo volume and total flash rate, even after these quantities were detrended from total storm volume. In contrast to the hail echo volume, the correlation between lightning and graupel volume peaked at zero lag, suggesting that graupel particles were the most important charge carriers within that storm, despite the presence of significant amounts of hail. These various correlations between lightning and storm parameters lend support to the hypothesis that updraft intensity and storm ice quantities control total lightning activity.

Typically, linear or power-law fits between flash rate and storm parameters have been developed, yielding equations of the form

$$f = \beta_0 + \beta_1 \times (sp) \text{ or } f = \beta_0 \times (sp^{\beta_1}) \tag{1.2}$$

where f is total flash rate, sp represents the value of a storm parameter, and β_0 and β_1 are coefficients. Barthe et al. (2010) tested a number of the flash rate parameterizations discussed above in cloud-resolving model simulations of an airmass thunderstorm in Alabama and a severe storm in Colorado. Their study found variable results: in particular, some schemes predicted flash rates well for one storm but not the other, possibly suggesting a regional limitation of some flash rate schemes. The Price and Rind (1992) cloud top height scheme successfully predicted flash rates only for the Alabama storm, while a scaled version of the Price and Rind (1992) W_{max} scheme predicted flash rates well only for the Colorado storm. This current study will evaluate five of the

lightning-storm parameter relationships summarized above as potential predictors of flash rate and develop new flash rate parameterizations specific to the Colorado domain. All the schemes selected were tested by Barthe et al. (2010) and are deserving of further evaluation against observations. The five schemes include the Price and Rind (1992) W_{max} and cloud top height schemes (referred to herein as PR92W and PR92H), the Deierling and Petersen (2008) $UV5$ scheme (DP08) and the Deierling et al. (2008) PIM and P_{flux} schemes (D08P and D08F). Each of these five parameterizations is summarized in Table 1.1.

1.3. Recent observations: the Deep Convective Clouds and Chemistry Experiment

The Deep Convective Clouds and Chemistry (DC3) experiment (Barth et al. 2014) took place in May and June 2012 in northeastern Colorado, central Oklahoma, and northern Alabama. The primary goals of DC3 were to examine the relationship between the microphysical and dynamical structure of thunderstorms and the resulting transport of chemical species, the impact of convective transport on the composition of the upper troposphere/lower stratosphere, as well as the production of NO_x by lightning. The three distinct regions studied in DC3 provided the opportunity to sample a broad range of storms with different dynamics, microphysical characteristics, electrical structures, and background tropospheric chemistry. Particular emphasis is given by this study to storms observed in the Colorado domain.

Thunderstorms in the Central-High Plains of the United States, which includes northeastern Colorado, sometimes exhibit markedly different electrical behavior than storms in other regions of the US. Central-High Plains storms are more frequently observed to possess anomalous charge structures that produce predominantly positive CG (+CG) lightning flashes and large IC/CG ratios (Lang and Rutledge 2002; Lang et al. 2004b; Fuchs 2014). These anomalously electrified storms

are often characterized by the presence of a region of positive charge at mid-levels (at temperatures around $-20^{\circ}\mathrm{C}$) with negative charge above (and at times also below). This is in contrast to the "normal" polarity tripole observed in most thunderstorms, characterized by a mid-level region of negative charge bounded by an upper and lower region of positive charge (Wilson 1920; Williams 1989; Bruning et al. 2014). A much larger fraction of severe weather in the central United States has been associated with +CG lightning than in other regions (Carey and Rutledge 2003; Carey et al. 2003). This trend suggests that the combination of relatively large thermodynamic instability and high cloud base heights unique to the Central-High Plains supports both organized, severe convection and anomalous electrification (Williams et al. 2005).

More generally, past studies (e.g. Williams et al. 2005; Fuchs 2014) have documented the regional variability and strong influence on lightning flash rate of environmental quantities such as warm cloud depth, cloud base height, and the vertical distribution of convective available potential energy (CAPE). For example, Fuchs (2014) documented significantly higher median flash rates in Colorado than in Alabama, accompanied by shallower warm cloud depths and higher cloud bases in Colorado. Given the strong regional variability of lightning flash rate and the suspected role of thermodynamics, an open question is whether a single flash rate parameterization can consistently predict total lightning behavior across different regions. Price and Rind (1992) have already advocated different cloud top height-based lightning parameterizations for oceanic versus continental environments.

The observations taken during DC3 provide the means to improve understanding of thunderstorm charging, the relationship of storm parameters to lightning across different regions, and the processing of chemical species by thunderstorms. The observational networks in each of the three domains consisted of multiple radars for the retrieval of dual-Doppler winds, at least one radar

with dual-polarization capability for the determination of hydrometeor types and microphysical characteristics of storms, aircraft observations of the chemical species within storm inflow and outflow regions, environmental soundings on days of active convection, and three-dimensional (3-D) lightning mapping arrays (LMAs) (Barth et al. 2014). These combined observations afford an unprecedented opportunity to better constrain lightning NO_x production on the storm scale, and possibly on larger scales.

Lightning mapping arrays are a ground-based observational means to detect most lightning flashes occurring within storms and to infer bulk storm charge structures. An LMA is capable of detecting IC flashes in addition to some CG flashes, making it a superior means to estimate total lightning flash rate in storms. Electromagnetic radiation is emitted during electrical breakdown in clouds when the stepped leader propagates in a discontinuous fashion, creating an ionized channel through the air and eventually leading to lightning (Krehbiel et al. 2000). The discontinuous propagation of the stepped leader results in frequent time rate of changes of current, giving rise to the emission of nearly impulsive radiation sources in the VHF region of the radio band (60-66 MHz) (Thomas et al. 2004). An LMA consists of a network of stations that detect the VHF radiation. Since VHF radiation is emitted along a stepped leader's path, the spatial extent and duration of an entire breakdown event can be determined (Krehbiel et al. 2002). By clustering all VHF sources associated with each flash in a storm, a total number of flashes can be determined. Additionally, since the 3-D location of each VHF source is known, estimates can be made of individual flash sizes (characteristic flash volumes, areas, and length scales).

1.4. GOALS OF THIS STUDY

The recent research discussed above has documented robust relationships between flash rate and a variety of different storm parameters. The DC3 dataset provides the opportunity to evaluate

and possibly improve these existing flash rate parameterizations. This study expands upon recent work by investigating whether bulk quantities representative of the updraft strength and mixed-phase microphysics in Colorado thunderstorms can consistently be used to quantify the magnitude and trend of total lightning flash rate. The following questions will be addressed:

(1) Do relationships between lightning flash rate and simple bulk storm parameters derived in the literature, or modified relationships derived from the Colorado DC3 dataset, function as reliable predictors of lightning activity in northeastern Colorado thunderstorms?

(2) What other storm parameters or combinations of storm parameters not considered by previous studies are reliable predictors of lightning activity in Colorado storms?

(3) Are flash rate parameterizations developed for a single region (Colorado) applicable to storms in other regions (i.e., Alabama) with different thermodynamic environments?

Questions 1) and 2) are important components in reducing uncertainty in total LNO_x produced by individual thunderstorms. The large regional variability in total lightning activity found by Fuchs (2014) underscores the importance of answering question 3). Chapter 2 of this work focuses on the methods used to calculate storm dynamical and microphysical parameters and total lightning flash rates. Chapter 3 presents the results of testing modified and new flash rate parameterizations against observations of Colorado and Alabama thunderstorms. In Chapter 4, the relative predictive capabilities of various storm parameters are analyzed, along with recommendations for constraining the use of some flash rate parameterizations to different storm environments. Additionally, a possible means of incorporating this work into an improved LNO_x parameterization scheme is discussed. A summary of key findings and recommendations for future work are provided in Chapter 5.

TABLE 1.1. Summary of flash rate parameterization schemes from the literature that were tested against observations of storms in this study. The first column lists the storm parameter used to predict flash rate, the second column lists the derived mathematical relationship between each parameter and flash rate (f), and the final column lists the reference for each flash rate scheme.

Parameter used to predict lightning flash rate (units)	Equation	Reference
Maximum vertical velocity (m s^{-1})	$f = (5.0 \times 10^{-6}) \times W_{max}^{4.5}$	Price and Rind (1992) (PR92W)
Cloud top height (km)	$f = (3.44 \times 10^{-5}) \times H^{4.9}$	Price and Rind (1992) (PR92H)
Updraft volume > 5 m s^{-1} (m^3)	$f = (6.75 \times 10^{-11}) \times UV5 - 13.9$	Deierling and Petersen (2008) (DP08)
Precipitating ice mass (kg)	$f = (3.4 \times 10^{-8}) \times PIM - 18.1$	Deierling et al. (2008) (D08P)
Ice mass flux product (kg^2 m s^{-2})	$f = (9.0 \times 10^{-15}) \times P_{flux} + 13.4$	Deierling et al. (2008) (D08F)

CHAPTER 2

DATA AND METHODS

To examine relationships between lightning and storm parameters, gridded polarimetric radar observations and three-dimensional wind retrievals were merged with LMA data for eleven storms in northeastern Colorado and four storms in the region of northern Alabama/southern Tennessee. Colorado data only were used to develop new lightning parameterizations and included 183 storm volume scans from the eleven Colorado thunderstorms. Dual-Doppler wind retrievals were possible for seven of the eleven Colorado cases for a total of 96 volume scans. Three-dimensional winds could not be retrieved for some cases either because a storm was not located in a region suitable for accurate wind retrievals (Figure 2.1), or multiple radars were not available for synchronized scanning. Nine of the eleven Colorado case studies were observed during the DC3 observational period (May-June 2012), and two were observed during summer 2013 during the CHILL Microphysical Investigation of Electrification (CHILL-MIE) field project (Brody Fuchs, personal communication). The primary goals of CHILL-MIE were to observe microphysical processes associated with storm electrification and to examine the environmental factors leading to anomalous charge structures within storms (Bruning et al. 2014). However, the availability of synchronized dual-Doppler scans combined with polarimetric radar data and LMA data during CHILL-MIE motivated the inclusion of these additional cases. A map of the DC3 Colorado experimental domain is provided in Figure 2.1.

All Alabama storms analyzed occurred during DC3; dual-Doppler data were available for two of the four Alabama storms. For the Alabama cases, quality-controlled, gridded radar data and dual-Doppler derived wind fields were obtained from the University of Alabama, Huntsville (UAH) (Retha Matthee; Larry Carey, personal communication). The primary radar used in Alabama was

the UAH Advanced Radar for Meteorological and Operational Research (ARMOR) C-band dual-polarization Doppler radar. Radial velocity data collected by the Huntsville, AL KHTX National Weather Service (NWS) Weather Surveillance Radar 1988-Doppler (WSR-88D) radar were incorporated for dual-Doppler wind retrievals. Details of the Alabama radar data, the data processing, and the observational domain are given in Bain (2013).

2.1. RADAR DATA

This study makes use of radar volume scans consisting of multiple radar sweeps through a constant azimuth range. The sweeps occur at ascending elevation angles; each volume scan occurs at regularly spaced time intervals to sample a storm throughout its lifetime. Volume scans were gridded to a 3-D Cartesian grid for analysis of bulk storm microphysical and dynamical quantities. During the DC3 field project, the primary radars employed in the Colorado domain were the CSU-CHILL S-band dual-polarization Doppler radar located in Greeley, CO and the CSU-Pawnee S-band Doppler radar, located about 50 km to the north-northwest. CHILL has a beamwidth of 1.1° and can operate at two frequencies (S- and X-band) but by design, operated in S-band only mode during DC3. CHILL operated in dual S- and X-band mode during CHILL-MIE, but only S-band data are used in this study. Pawnee operates at vertical polarization with a beamwidth of 1.26°. The CHILL and Pawnee radars were used for all dual-Doppler wind retrievals, and CHILL was used for all polarimetric retrievals during DC3. The orientation of CHILL and Pawnee allows for Doppler wind retrievals to the west, over a large swath of the Colorado Front Range, and to the east over the Colorado northeast plains (Figure 2.1). During both field projects, CHILL operated in alternating horizontal and vertical transmit mode to retrieve radar reflectivity (Z), radial velocity (VR), spectrum width (SW), differential reflectivity (Z_{DR}), propagation differential phase (ϕ_{DP}), correlation coefficient (ρ_{HV}), and linear depolarization ratio (LDR). Polarimetric

retrievals were also obtained for one CHILL-MIE case study from the NWS Weather Surveillance Radar 1988-Doppler Polarimetric (WSR-88DP) radars in Cheyenne, WY (KCYS) and near Denver, CO (KFTG). These radars were used for polarimetric retrievals when CHILL volume scans were unavailable. The WSR-88DP radars operated in simultaneous transmit and receive mode to retrieve the same polarimetric quantities as CHILL except for LDR.

The radar data were first inspected manually and any aliased velocity fields were corrected using the National Center for Atmospheric Research (NCAR) SOLO3 software. Before gridding the data, the specific differential phase (K_{DP}) was calculated from the ϕ_{DP} field using the method of Wang and Chandrasekar (2009). Once the velocity fields were corrected and K_{DP} calculated, for CHILL data, the Z (dBZ), VR, Z_{DR}, K_{DP}, ρ_{HV}, LDR, and particle fall speed (V_t, estimated from the hydrometeor identification field, see section 2.2) fields were gridded to a 3-D Cartesian grid using the NCAR Sorted Position Radar INTperolation (SPRINT) software. The SPRINT software interpolates the data using a nearest-neighbor interpolation method. WSR-88DP data were gridded using the NCAR REORDER software package (a large grid domain was desired for the 3 August 2013 case for which WSR-88DP data were used; SPRINT has limited maximum grid bounds). REORDER uses a Cressman closest point interpolation scheme (Cressman 1959). All Colorado radar data were gridded to 0.5 km resolution in the horizontal and vertical; Alabama data obtained from UAH were gridded to 1.0 km in the horizontal and vertical. As part of the gridding and interpolation process, Colorado radar data fields were automatically thresholded on a flag designed to indicate regions of noise and non-meteorological targets such as range aliased echo (second trip) and ground clutter. This flag was created based on values of the normalized coherent power (NC). The gridded data were manually inspected and it was confirmed that non-meteorological echo had been sufficiently removed.

2.2. IDENTIFICATION OF HYDROMETEOR TYPES

In order to calculate storm total ice contents and relate microphysical properties to the wind fields, gridded polarimetric radar variables were used to determine the dominant hydrometeor types within storms. For all Colorado and Alabama storms, polarimetric radar retrievals (Z, Z_{DR}, K_{DP}, and ρ_{HV}) combined with temperature data from NWS soundings closest to the storms were input to a fuzzy logic Hydrometeor IDentification algorithm (HID) developed by Dolan et al. (2013). LDR data were also retrieved by the CHILL and ARMOR radars but were not used in the HID because 1) LDR data were unavailable for simultaneous transmit and receive WSR-88DP data and 2) LDR fields were sometimes unsatisfactory or incomplete throughout storm volumes. The HID outputs 10 hydrometeor categories: drizzle, rain, ice crystals, aggregates, wet snow, vertically oriented ice crystals, low density graupel, high density graupel, hail, and big drops. For each hydrometeor category, a membership beta function (MBF) was constructed from electromagnetic scattering simulations as a function of each polarimetric variable and temperature (Dolan and Rutledge 2009). Different MBFs appropriate for S- versus C-band radar data were used for the Colorado and Alabama case studies. MBFs range from zero to one and indicate the probability that a certain hydrometeor type exists for values of the various polarimetric variables. For example, the S-band hail MBF is equal to one for $Z > 50$ dBZ but is equal to zero for $K_{DP} > 1.5$ degrees per km. At each grid point, the values of all MBFs for each hydrometeor type are weighted and summed to arrive at a score for that type. The weights given to the variables Z, Z_{DR}, K_{DP}, ρ_{HV}, and temperature are, respectively, 1.5, 0.8, 1.0, 0.1, and 0.5. These weights were chosen subjectively by Dolan et al. (2013) to reflect the confidence in the accuracy of each measured variable. The score for each hydrometeor type is then multiplied by the weighted MBF value for Z and temperature alone, since these variables most strongly indicate the presence of different hydrometeor

types. At each grid point, the hydrometeor type with the highest score is determined to be the dominant category.

2.3. Retrieval of three-dimensional wind fields

In order to measure storm updraft intensity, the 3-D wind field was synthesized from gridded radial velocity data. Radial velocity data from at least two properly positioned Doppler radars can be combined through trigonometric relationships to determine the horizontal (u, v) velocity fields at each grid point (Rinehart 2010). The convergence calculated from the velocity fields can then be input into the mass-continuity equation and integrated to diagnose vertical motion (w). However, radial velocity fields can contain a contribution from particle fall speeds, particularly for high elevation angles. For this reason, estimates were made of particle fall speeds, and any fall speed contribution to the radial velocity fields was removed, based on knowledge of the elevation angle of each radar scan. Estimates of particle fall speeds were determined by first running the 10-category HID (section 2.2) in radial space and reducing the output into four simpler categories: rain, graupel/hail, dry snow, and wet snow. Then, for all radar pixels containing rain, graupel, or hail, the following reflectivity-fall speed relationships from Giangrande et al. (2013) were assumed:

$$V_t = 3.15 \times \{10^{(0.1 \times Z(dBZ))}\}^{0.098} \text{ (rain)} \tag{2.1}$$

$$V_t = 2.2 + \{10^{\frac{[Z(dBZ)-33.0]}{10.0}}\}^{0.5} \text{ (graupel/hail)} \tag{2.2}$$

For dry and wet snow, constant fall speeds of 1 and 2 m s^{-1} were assumed, respectively. These four reflectivity-fall speed relationships were deemed appropriate since they were derived for deep convective cores in Oklahoma thunderstorms.

Gridded radial velocity fields from the CHILL and Pawnee radars and particle fall speed fields were read into the Custom Editing and Display of Reduced Information in Cartesian Space (CEDRIC) software (Mohr et al. 1986). The particle fall speed estimates were incorporated to generate linear equations in u, v, and w at each point on the Cartesian grid. The vertical velocity estimate at each point was initially assumed to be zero so that u and v could be explicitly calculated. The horizontal divergence was computed, allowing an initial estimate of w to be obtained by integration of the anelastic mass continuity equation

$$\frac{\partial u}{\partial x} + \frac{\partial v}{\partial y} + \frac{\partial w}{\partial z} = -\frac{w}{\rho_0}\frac{\partial \rho_0}{\partial z}, \tag{2.3}$$

where air density ρ_0 is a function of z but assumed to be invariant in the horizontal. A downward integration method was used which assumes boundary conditions of w = 0 at the top of the radar domain. The resulting w field was used to recompute u and v from the system of linear equations, and the u and v solutions were again input into the continuity equation to solve for w. The process was repeated iteratively until solutions for u and v converged. Solutions for the u and v fields were retained only where the beam-crossing (between-beam) angle exceeded 31 degrees. Imposing a beam-crossing angle threshold sets an upper bound on the allowable combined error in u and v (Davies-Jones 1979). Finally, the divergence was calculated from the iterative solutions for u and v and integrated to obtain a final solution for w.

2.4. OBJECTIVE IDENTIFICATION OF STORMS

To accurately calculate storm parameters and attribute detected lightning flashes to storms, reflectivity regions corresponding to individual storm cells were objectively identified. Cell identification was accomplished using the Colorado State University (CSU) Lightning, Environmental,

Aerosol, and Radar (CLEAR) framework developed by Lang and Rutledge (2011) and revised by Fuchs (2014). The CLEAR framework is able to ingest large amounts of data of various types and attribute these data to features of interest identified and tracked by the software. The CLEAR framework is used herein to identify contiguous regions of gridded radar reflectivity data throughout time (storm tracks) and to attribute lightning data to the identified storms. In this way, the relationship between storm parameters and flash rates can be analyzed. CLEAR was shown by Fuchs (2014) to consistently and successfully track isolated convective storms. That study gives a more detailed description of CLEAR and its capabilities.

In the present work, the CLEAR tracking algorithm was used to identify storms based on the composite radar reflectivity field. The composite field was constructed using reflectivity data retrieved either by CHILL or a WSR-88DP radar. Individual storm "cells" were identified from the composite reflectivity and assigned to a particular storm "track". The cell and its characteristics represent the storm at one particular time, and the track contains cell information over the entire lifetime of a storm. Potential cells were initially identified based on contiguous 35-dBZ composite reflectivity areas. Within an identified 35-dBZ area, if the 45-dBZ region exceeded a specified area threshold, then the 35-dBZ region was counted as a convective cell. This area threshold was chosen for each case to adequately track the storm through its initiation, mature phase, and dissipation stages. For some cases (particularly weaker storms), different upper-reflectivity thresholds were used (e.g., 40-dBZ) so that these cases were better tracked in a subjective sense. Once a cell area was identified, this region of the gridded data was labeled with a unique number and the cell was assigned to a track. The CLEAR software retains information about the motion of previously identified tracks to determine whether a new cell should be part of an existing track or become a new track. Track information can be indexed to get all the cell numbers corresponding to one particular

storm. An example of the output of the CLEAR cell-tracking algorithm, including identified cells and tracks, is provided in Figure 2.2.

2.5. Environmental data

Environmental sounding data were used to calculate CAPE, vertical wind shear, and to identify temperature height levels in order to identify the mixed-phase region of storms. For all DC3 Colorado cases, environmental data were derived from NCAR/EOL Mobile GPS Advanced Upper-Air Sounding System (MGAUS) or Mobile Integrated Sounding System (MISS) soundings launched during DC3. University of Alabama-Huntsville (UAH) mobile soundings launched during DC3 were used to calculate environmental parameters for Alabama storms. These soundings exhibited excellent vertical resolution and were usually launched within an hour and from locations close to storm initiation. The sounding subjectively determined to be closest in time and space to storm initiation was chosen, in order to best represent the environment in which the storm developed. Temperature levels derived from each selected sounding were interpolated to the radar data grid to be used in storm parameter calculations. For the CHILL-MIE cases, no special soundings were taken, so the closest-in-time soundings launched by the NWS in Denver, Colorado were used to calculate temperature levels. CAPE and shear quantities for the CHILL-MIE cases were calculated by attributing time-interpolated environmental analyses from the Rapid Refresh (RAP) model (Benjamin et al. 2007). Data were attributed to each tracked cell by determining the model grid point in the inflow of a storm's forecasted position (Potvin et al. 2010). A more complete discussion of this environmental data attribution method is given in Fuchs (2014). Although this method is objective and properly samples storm inflow air, model-derived environmental quantities (especially vertical wind shear) sometimes differed significantly from observations. For this reason, observed environmental quantities were used whenever possible.

2.6. CALCULATION OF STORM PARAMETERS

Storm parameters were calculated by indexing the gridded updraft, HID, and reflectivity data over the cell areas identified by the CLEAR software. An identified cell area was expanded into all vertical levels to arrive at a cell volume. Using temperature levels interpolated from the environmental soundings, the cell volume was constrained to levels within the mixed-phase region. Since the volume bounded by 35-dBZ was chosen as the cell volume, cell volumes were representative of the high-reflectivity convective core, which is desirable for relating storm parameters to lightning activity. Many storm parameters were calculated; an overview of the calculation methods for several storm parameters that are eventually related to lightning activity is given here.

Thunderstorm hydrometeor echo volumes, reflectivity echo volumes, updraft volumes, and precipitating ice mass were calculated by this study because they have been found to correlate well to total lightning activity (see section 1.2). Each of these quantities was calculated only within the mixed phase region of storms ($-5^{\circ}\mathrm{C}$ to $-40^{\circ}\mathrm{C}$). To calculate graupel echo volume, the number of grid boxes within the mixed-phase storm volume for which the HID identified graupel as the dominant particle type was determined. This number was multiplied by the volume of a single grid box to arrive at the total echo volume. Using combined HID output and reflectivity data, the precipitating ice mass (defined herein as graupel and hail) was calculated as well. For each grid box identified as containing graupel or hail, the reflectivity was converted to mass using separate reflectivity-mass (Z-M) relationships for graupel and hail derived by Heymsfield and Miller (1988). These particular Z-M relationships were chosen because they were derived for High Plains thunderstorms in Montana with microphysical characteristics likely similar to Colorado storms (Deierling et al. 2008). The resulting mass per cubic meter was converted to kg by multiplying by the volume of the grid box. The masses in all identified grid boxes were then summed. The 30-dBZ

echo volume was calculated by summing the number of grid boxes with reflectivity above 30-dBZ and multiplying by the grid box volume. Updraft volumes above a given vertical velocity threshold were determined the same way. The maximum vertical velocity was calculated by simply finding the absolute maximum in updraft for all grid points in the mixed-phase region.

The product of precipitating ice mass flux and non-precipitating ice mass flux was calculated following the divergence method used by Deierling et al. (2008), although in contrast to that study, the flux product calculation herein was constrained to the identified 35-dBZ cell region (section 2.4). Non-precipitating ice mass flux within the mixed-phase region of storms is not directly observed since reflectivity in these regions is dominated by larger graupel and hail particles. Thus, non-precipitating ice in regions of large divergence ($> 10^{-3}$ s^{-1}) was assumed to approximate non-precipitating ice exiting the updraft. Maximum graupel area was determined by finding the largest contiguous region of graupel and hail identified by the HID out of all vertical levels within the mixed-phase region. Various reflectivity areas were calculated from the composite reflectivity field. Graupel and various dBZ maximum heights were calculated by finding the absolute maximum height of these quantities over all vertical levels of the radar domain.

2.7. FLASH COUNTING

For this study, it was necessary to accurately identify individual lightning flashes and attribute the identified flashes to storms. Lightning mapping arrays, as discussed in section 1.3, offer one of the few means to observe the location and size of most flashes that occur in a thunderstorm. To determine the location and time (x, y, z, t) of a VHF emission source caused by the lightning discharge process, the time of arrival (TOA) of the VHF radiation detected at various stations comprising an LMA network is recorded using a GPS receiver (Krehbiel et al. 2000). The distance

between the station and the emitted source is given by

$$c(t - t_i) = \sqrt{(x - x_i)^2 + (y - y_i)^2 + (z - z_i)^2} \tag{2.4}$$

where (x_i, y_i, z_i, t_i) give the known location of the station and TOA of a VHF source and c is the speed of light. Since the above equation contains four unknowns, a minimum of four different stations is required to pinpoint the time and location of an emitted VHF source (Thomas et al. 2004). Typically, LMAs are comprised of additional stations to reduce errors in estimates of VHF source locations and times. Thomas et al. (2004) found that for the 13 station LMA network operated during the STEPS campaign (Lang et al. 2004b), VHF sources could be located to within 12 m in the horizontal and 30 m in the vertical, with corresponding time errors of about 50 ns. The northern Colorado LMA (COLMA) network currently consists of 15 stations (Figure 2.1). The network has a diameter of about 100 km, allowing flashes to be reliably detected and mapped as far as 350 km from the center of the network (Rison et al. 2012).

Some previous studies (e.g. Wiens et al. 2005) have used a flash counting algorithm developed by Thomas et al. (2003) to sort detected VHF radiation sources into individual lightning flashes. This algorithm is implemented in the XLMA software (Rison et al. 1999), considered the standard tool for LMA data analysis. In other studies, such as Lang et al. (2004a), flashes were counted manually in XLMA since they were sufficiently separated in time. Given the relatively large number of case studies analyzed and the large flash frequencies known to occur in eastern Colorado thunderstorms (Fuchs 2014), this study uses an automated flash counting algorithm. This automated algorithm was developed by Dr. Eric Bruning at Texas Tech University and Brody Fuchs at Colorado State (personal communication). The algorithm is open source and uses a Density-Based

Spatial Clustering of Applications with Noise (DBSCAN) algorithm (Ester et al. 1996) implemented in the Python programming language. For LMA data, DBSCAN assigns an LMA source to a flash so long as it is sufficiently close in space and time to another source in the flash, and that source is surrounded by a sufficient number of other sources to be identified as a cluster (flash).

The DBSCAN flash clustering algorithm was first used by Fuchs (2014) to study the contrasting relationships between flash rates and environmental parameters in different regions of the United States. That study found that flash counts for selected storms were within 10-15 percent of flash counts using the XLMA software. In order for a cluster of VHF sources to be counted as a lightning flash, for the Colorado LMA dataset a minimum of 10 sources must be associated with that cluster. Additionally, all consecutive sources associated with one flash may be separated by no more than 3 km in space and 150 ms in time, thresholds advocated by MacGorman et al. (2008). The minimum source threshold was relaxed to two points for Alabama data due to the lower sensitivity of the Alabama LMA network. Since fewer LMA sources are associated with each flash in Alabama, a 3 km distance threshold tends to result in flashes being frequently broken up. For this reason, the distance threshold was increased to 6 km for clustering of Alabama LMA sources. Finally, for a source to be counted as part of a flash, it must have been detected by at least seven of the stations comprising the LMA network for Colorado, and by six for Alabama. An exception was made for the two 2013 CHILL-MIE cases (Table 2.1). Only LMA data collected in real-time were available when these cases were analyzed, and these real-time data sometimes contained VHF sources detected by only six stations.

Once lightning flashes were identified, each flash was attributed to the storm from which it originated. The flash counting algorithm was merged with the CLEAR framework to attribute identified lightning flashes to storms in an automated manner. Lightning flashes were attributed

to storms if their initiation location occurred within identified 35-dBZ regions (cells). To account for lightning flashes that occur outside of the main convective cores (e.g., in storm anvils), flashes within 10 km of an identified cell were also attributed. If an identified flash was within 10 km of more than one cell, it was attributed to the nearest cell. Since the flash attribution was done in this automated way, little hands-on work was required, and flash counting for multiple cases could be run relatively quickly.

Each gridded radar volume scan analyzed in this study was identified by the time at which the volume scan began. Typically each scan would proceed for five or six minutes through a series of elevation angles. A new volume scan would begin immediately upon completion of the previous scan. Thus, storm parameters calculated from the gridded volume scans are most representative of the storms characteristics between the beginning of a particular scan and the next one. For this reason, flashes occurring between the start of one volume scan and the subsequent scan were attributed to the first volume. The total number of flashes attributed to a given storm between two scans was divided by the intervening time to arrive at a storm-total flash rate (flashes per minute). This flash rate was assigned to the time that the first volume scan began. A representative size for each individual flash was also determined. To do this, the convex hull area, defined as the minimum area enclosing a horizontal projection of all VHF sources associated with that flash, was calculated (Bruning and MacGorman 2013). A characteristic flash extent was calculated as the square root of the convex hull area. A flash extent therefore has linear units and was taken to be representative of the flash channel length.

2.7.1. Flash counting accuracy

For two Colorado cases, 5 June 2012 and 6 June 2012 storm 1, the automated flash counting algorithm used in this study was tested against the Thomas et al. (2003) algorithm. The XLMA

software was used to identify regions of lightning activity corresponding to each storm, select proper time periods for flash counting, and then run the Thomas et al. (2003) algorithm. Figure 2.3 shows the flash counting results for the algorithm used in this study versus the Thomas et al. (2003) algorithm: for 5 June 2012, both algorithms calculated nearly identical flash rates. For 6 June storm 1, peak flash rates determined using the algorithm in this study exceeded flash rates determined using the Thomas et al. (2003) algorithm by no more than 15 percent. Running the Thomas et al. (2003) algorithm resulted in a very similar flash rate trend. For the lowest flash rates in this storm, the two algorithms were in even closer agreement. The algorithm used by this study may tend to break up some flashes, a common problem of many flash counting algorithms. However, any small decrease in accuracy should be compensated by the increased objectivity of automatically identifying storm cells and attributing flashes. Figure 2.4 is an XLMA-style plot showing all flashes identified by the flash counting algorithm used in this study and attributed to the 6 June 2012 21:15 UTC Colorado storm volume. In a qualitative sense, the flash counting algorithm appears to correctly identify flashes.

2.7.2. Summary of storm-total lightning activity

Table 2.1 provides a brief summary of lightning activity, storm mode, and any severe characteristics for each Colorado storm. Mean and maximum flash rates are reported as well as the time period over which each storm was tracked and whether a dual-Doppler analysis was performed. Each storm is referred to by the date on which it was first identified and tracked by CLEAR. Multiple cases that occurred on a single day are further labeled in chronological order based on when the analysis period began. The same quantities are presented for the Alabama storms in Table 2.2.

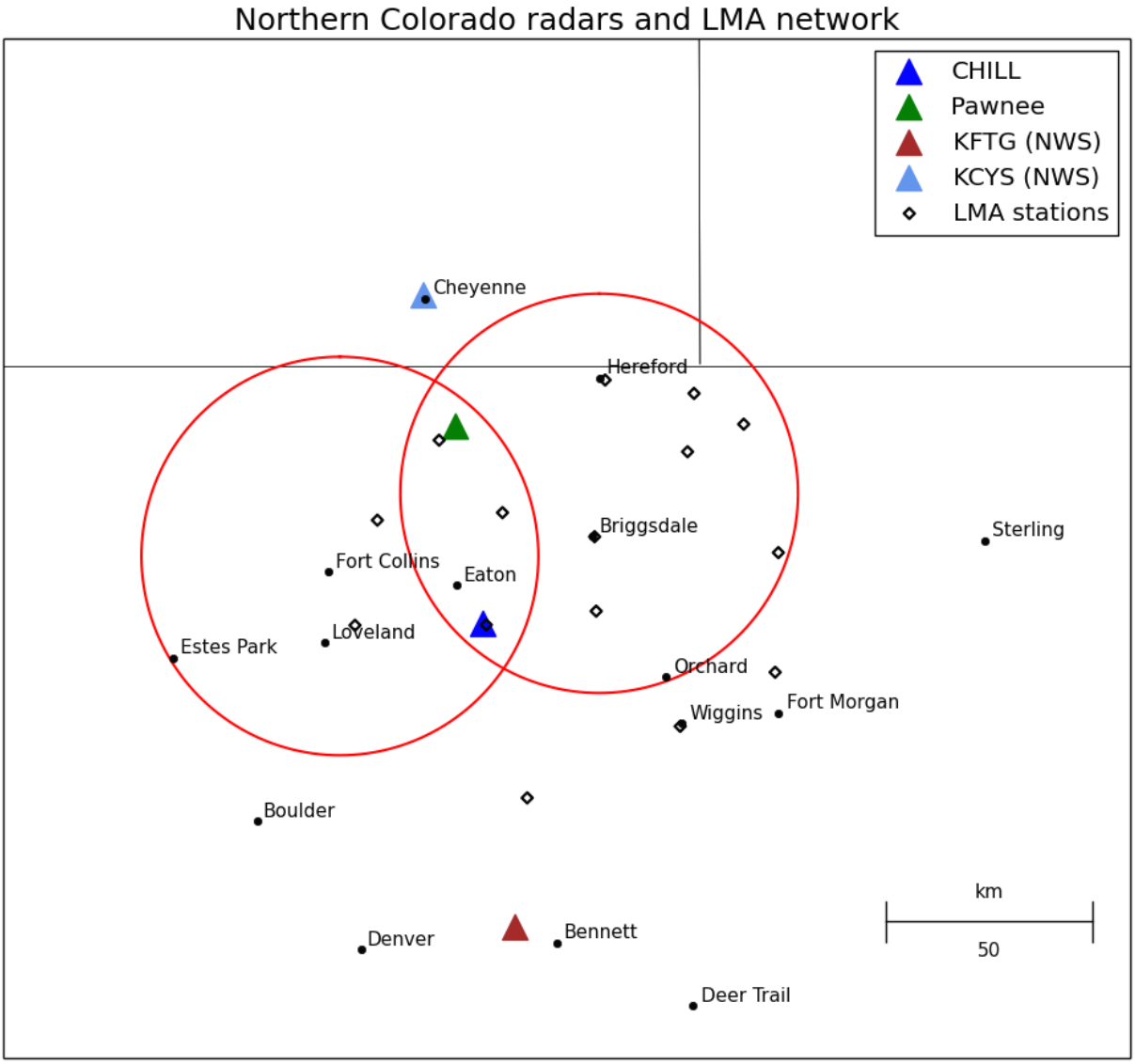

FIG. 2.1. Map of the Colorado DC3 experimental design showing the locations of the four radars that were used in this study (triangles). The CHILL-Pawnee dual-Doppler lobes (red) are also shown. Black diamonds indicate the location of stations comprising the northern Colorado LMA network. Locations of various cities and towns in northeastern Colorado are also indicated for spatial reference.

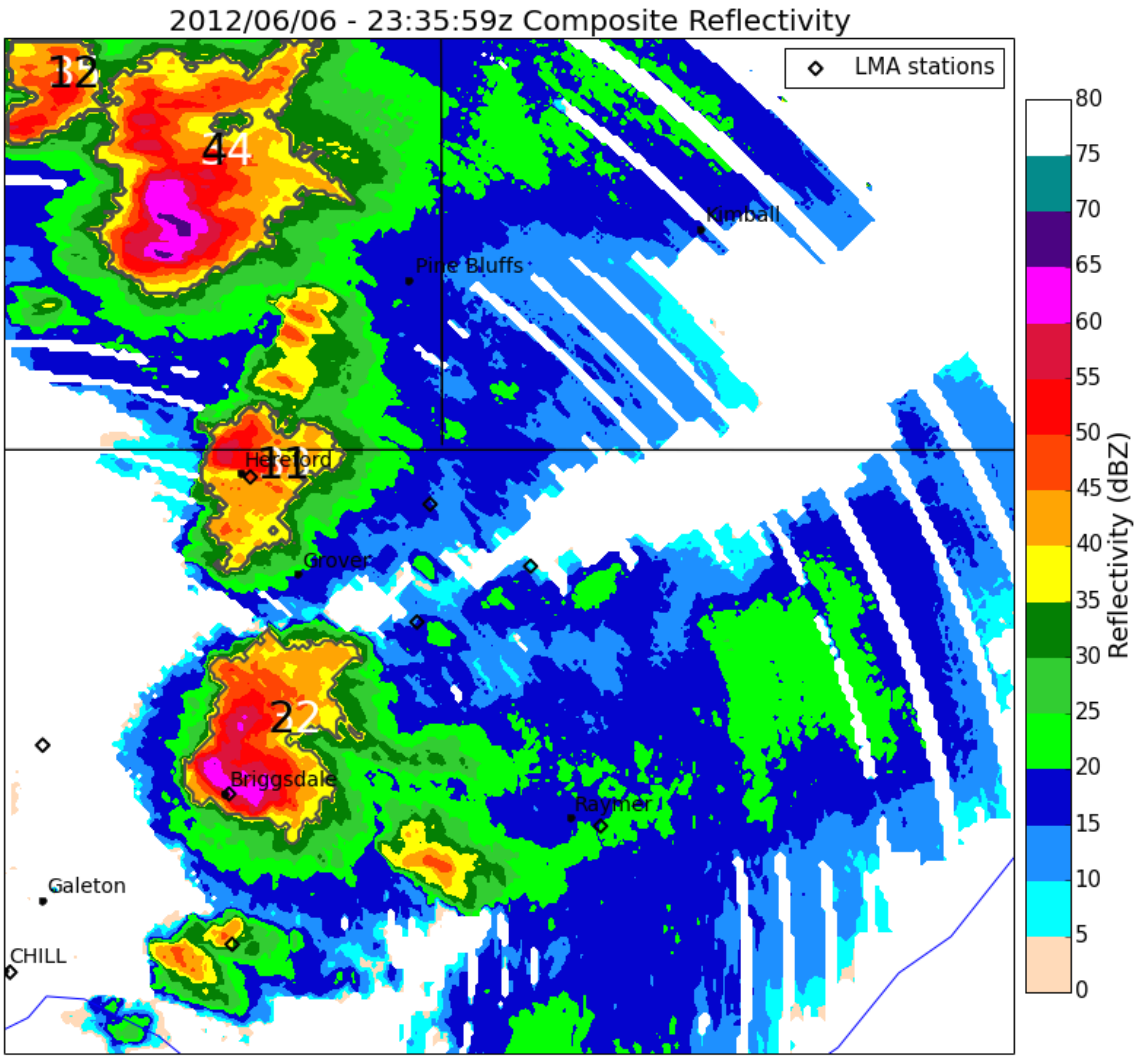

FIG. 2.2. Example of how the CLEAR cell-tracking algorithm works. Shown is a map of CHILL composite reflectivity for 6 June 2012 23:36 UTC. Large black numbers indicate identified tracks and large white numbers beneath the track numbers indicate individual cells corresponding to each track. Diamonds indicate the locations of stations comprising the northern Colorado LMA network. Also shown are the locations of the CHILL radar and various cities and towns in the northeastern Colorado domain for spatial reference.

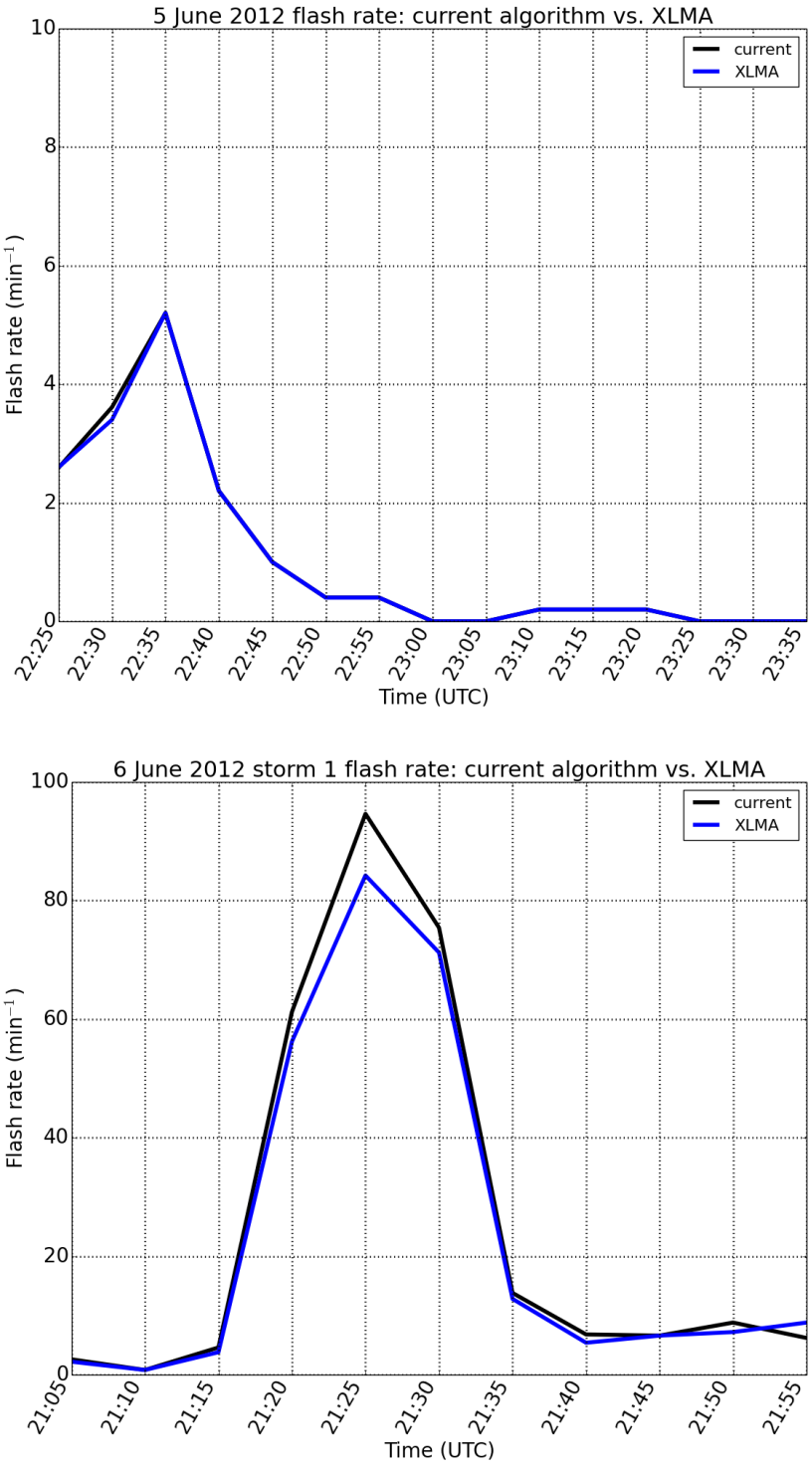

FIG. 2.3. Time series of total lightning flash rate for 5 June 2012 and 6 June 2012 storm 1 calculated with the algorithm used in this study ("current", black) and using the Thomas et al. (2003) algorithm ("XLMA", blue).

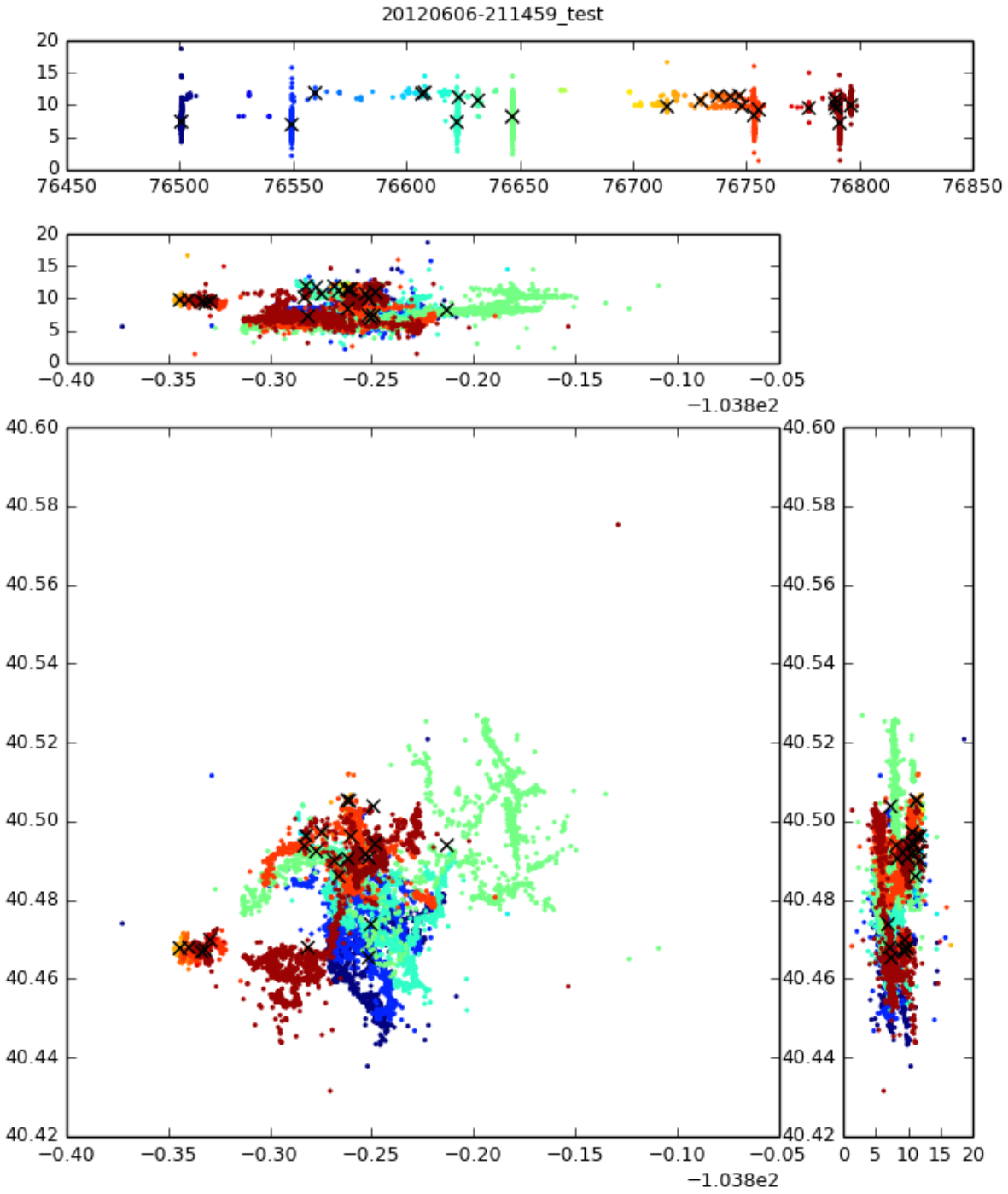

FIG. 2.4. Multi-panel plot showing VHF sources (colored points) detected by the Colorado LMA for the five-minute period beginning at 21:14:59 UTC on 6 June 2012. Sources are colored by time from blue to red. Each "×" marks a cluster of sources identified by the algorithm as a single lightning flash. The top panel is a time-height plot, with height in km and time in seconds (UTC). The panel immediately below shows an east-west vertical cross-section, with east-west distance in longitude. The bottom left panel shows all sources in a latitude-longitude projection, and the bottom-right panel shows a north-south vertical cross-section.

TABLE 2.1. Summary of storm type, severe characteristics, and total lightning activity for each Colorado storm studied. The first and second columns list the date and analysis period for each storm. The third column lists the subjectively identified storm type (single cell thunderstorm, multicell, or supercell) and any associated severe warnings or severe storm reports. Severe storm reports were obtained from the NWS Storm Prediction Center (SPC). The fourth and fifth columns list the mean and maximum total flash rates determined by the automated flash counting algorithm. The yes/no statements in the final column indicate whether dual-Doppler wind retrievals were performed. Asterisk indicates that polarimetric WSR-88DP data were used, not CHILL data.

	Analysis period HH:MM (UTC)	Storm type; severe reports	Mean total flash rate (min^{-1})	Maximum total flash rate (min^{-1})	Dual-Doppler synthesis
5 June 2012	22:25-23:35	single cell; non-severe	1.1	5.2	yes
6 June 2012 storm 1	21:05-21:55	single cell; non-severe	25.6	94.6	yes
6 June 2012 storm 2	21:30-23:30	supercell; 3.8 cm hail	107.3	169.7	no
6 June 2012 storm 3	23:00-00:18 7 June	single cell; 2.5 cm hail	48.0	92.3	yes
6 June 2012 storm 4	23:06-00:18 7 June	single cell; non-severe	40.3	87.5	yes
22 June 2012 storm 1	22:35-23:45	supercell; severe warned	115.5	223.0	no
22 June 2012 storm 2	23:55-00:50 23 June	single cell; non-severe	35.3	140.4	no
27 June 2012	21:55-22:50	single cell; non-severe	13.8	54.4	yes
28 June 2012	20:40-22:00	single cell; non-severe	8.1	26.4	yes
17 June 2013 CHILL-MIE	20:55-23:00	supercell; severe warned	29.8	58.4	yes
3 August 2013* CHILL-MIE	21:14-23:36	supercell; 4.4 cm hail, tornado	136.0	178.3	no

TABLE 2.2. As in Table 2.1, but for the four Alabama thunderstorms studied. All Alabama storms studied occurred during DC3.

	Analysis period HH:MM (UTC)	Storm type, severe characteristics	Mean total flash rate (min^{-1})	Maximum total flash rate (min^{-1})	Dual-Doppler synthesis
18 May 2012	22:15-23:50	multicell; non-severe	8.5	21.7	yes
21 May 2012	20:01-21:23	multicell; non-severe	1.2	5.4	yes
11 June 2012	18:44-19:44	multicell; non-severe	3.2	9.3	no
14 June 2012	17:10-18:14	multicell; non-severe	20.3	50.2	no

CHAPTER 3

RESULTS

3.1. EVALUATION OF EXISTING FLASH RATE PARAMETERIZATIONS

The parameterizations listed in Table 1.1 were evaluated for all Colorado cases to determine their applicability to Colorado storms observed during DC3 and CHILL-MIE. In Figures 3.1-3.3, the flash rate predicted by each storm parameter is shown along with the observed flash rate determined by the flash counting algorithm (observed flash rate time series will be denoted herein by black curves). The five flash rate parameterizations tested do not adequately predict total flash rates. There is a tendency to strongly underestimate flash rates, and some schemes (most notably the P_{flux} scheme) do not predict any flash rate variability at all. Not all predicted flash rates are shown for every case either because unphysical negative flash rates were predicted or the predicted flash rates fell above the range shown on each plot. The negative flash rates arise because of the large negative constant term in some of the parameterizations (Table 1.1). The PR92W maximum updraft scheme is relatively successful for 5 June 2012 (Figure 3.1a) and 6 June 2012 storm 4 (Figure 3.2a), although it predicts flash rates somewhat out of phase relative to observations for 6 June 2012 storm 4. PR92W is a power-law scheme, so it does not predict any negative flash rates. However, its prediction of the very strong dependence of flash rate on maximum updraft (a 4.5 power-law) is not observed. This strong dependence results in large underestimation of flash rates for moderate-flash rate storms with modest updrafts, such as 28 June 2012 (Figure 3.3a).

The coefficients of existing flash rate parameterizations must therefore be modified to accommodate the DC3/CHILL-MIE dataset. In particular, the coefficients are usually too small to predict the large flash rates observed in this study (e.g, the D08P scheme). An important caveat to using the Deierling et al. (2008) schemes is that their study used a different HID to calculate ice

masses and ice mass fluxes. The HID differences make it challenging to objectively test their PIM and P_{flux} schemes with the data used in this study. However, there should be less variability in how other quantities, such as maximum updraft and updraft volumes, are calculated, but the peak updraft and updraft volume schemes still did not predict flash rate well. In section 3.2 and 3.3, DC3/CHILL-MIE data are used to derive new coefficients for the PIM, W_{max}, $UV5$, and P_{flux} schemes. The ability of several other similar variables to predict flash rate is investigated as well. In section 3.4, various parameters related to cloud top height are combined with other quantities to develop new, multiple-parameter flash rate schemes.

3.2. Prediction of flash rates based on storm ice content

Three flash rate parameterization schemes based on 1) the volume of graupel (GEV) 2) the volume of reflectivity greater than 30 dBZ ($VOL30$), and 3) the precipitating ice mass (PIM) within the mixed-phase region of thunderstorms are developed. $VOL30$ is the simplest storm parameter out of the three to use as a predictor of flash rate, but may also perhaps have the least physical relationship to lightning activity. Whereas $GEV$and PIM explicitly account for the presence of rimed particles important to cloud electrification, there is less information about the types of particles contained within $VOL30$. To assess the validity of $VOL30$ as a predictor of flash rate, $VOL30$ was linearly regressed against both $GEV$and PIM. Figure 3.4 shows a scatterplot of $VOL30$ versus $GEV$and $VOL30$ versus PIM for each storm volume scan. $VOL30$ is very strongly correlated to the other two quantities, justifying its use as a proxy for the volume of rimed ice mass and therefore as a potential predictor of flash rate.

GEV, $VOL30$, and PIM were linearly regressed against total flash rate using a least squares technique. Scatterplots depicting each storm parameter's relationship to flash rate and the least-squares fit are shown in Figure 3.5. All three quantities were robustly correlated to flash rate,

indicated by a coefficient of determination (R^2) of 0.75, 0.80, and 0.80 for GEV, $VOL30$, and PIM, respectively. Each flash rate-storm parameter relationship was also strongly monotonic, indicated by Spearman correlation coefficients (ρ) near 0.9. Table 3.1 summarizes the results of the linear least squares fits, including the derived coefficients. For PIM, note that the constant coefficient is larger and the multiplier smaller in magnitude than in the D08P scheme. Note also that each of these flash rate parameterizations exhibited relatively large root mean square errors (RMSE). The large range of flash rates plotted in Figure 3.5 tends to mask a relatively large spread in the data around the best-fit trend lines.

Flash rate time series predicted by these schemes for the eleven Colorado cases are shown in Figures 3.6-3.8. The GEV, $VOL30$, and PIM schemes correctly predicted the general flash rate trend for most cases. Flash rate was predicted most successfully for 6 June 2012 storm 2 (Figure 3.6c) and 3 August 2013 (Figure 3.8c). Although brief, large increases in observed flash rate around 21:55 UTC for 6 June 2012 storm 2 and 22:40 UTC for 3 August 2013 were not predicted, the schemes capture the overall flash rate trend quite well. Flash rates are somewhat under-predicted for 22 June 2012 storm 1 (Figure 3.7b), but the overall flash rate trend is captured well. Interestingly, 6 June 2012 storm 2, 22 June 2012 storm 1, and 3 August 2013 were large, intense, and long-lived severe cells (Table 2.1). Flash rates were also predicted well for 6 June 2012 storm 4, an intense but much smaller storm (Figure 3.7a). Finally, although flash rates are generally over-predicted for 5 June 2012, the overall trend of low flash rates that continually decrease after an early maximum is captured somewhat well (Figure 3.6a).

Sometimes however, flash rate magnitudes were incorrectly predicted by a significant margin. The most striking example is 6 June 2012 storm 1 (Figure 3.6b), for which the GEV, $VOL30$, and PIM schemes all underestimate the peak flash rate by almost a factor of five. The extreme flash

rate variability in this storm (nearly two orders of magnitude) is not predicted. For other cases too, brief, prominent fluctuations in flash rate were not predicted well. The early flash rate maximum observed for 27 June 2012 (Figure 3.7d) is not predicted by any of the parameterizations, although the slowly decreasing flash rate trend is somewhat well predicted thereafter. For 22 June 2012 storm 2 (Figure 3.7c), flash rates were overestimated for most of the analysis period. Flash rates are correctly predicted for the majority of the 28 June 2012 analysis period, but an early flash rate peak is incorrectly predicted at 20:50 UTC (Figure 3.8a). For 17 June 2013 (Figure 3.8b), the general flash rate trend is predicted well, but magnitudes are overestimated, especially later in the analysis period. More importantly, the GEV, $VOL30$, and PIM parameterizations captured rapid temporal ($\sim$10 minute) variability in flash rate for this storm only some of the time. The 17 June 2013 observed flash rate time series exhibits several sharp local maxima and minima, while the predicted flash rate curves are smoother. Finally, the peaks in predicted flash rates for 6 June 2012 storm 3 lag the observed peak by roughly twenty minutes (Figure 3.6d). Peak flash rate for this storm is also underestimated by about one third.

The ice mass/echo volume schemes performed generally well because echo volumes and precipitating ice mass are indicators of storm size. Larger storms usually exhibit more robust mixed-phase processes (and therefore more lightning) in order to generate and maintain larger quantities of ice. However, while ice masses and echo volumes play a large role in controlling flash rate, other storm parameters or processes also appear to be important. A good example of the potential role of other processes is 17 June 2013. Over a twenty minute period from 21:55 to 22:15 UTC, flash rates increased from 25 to 58 per minute and then decreased almost as rapidly to 23 per minute (Figure 3.3b). This storm was able to maintain large quantities of precipitating ice through this period, evidenced by the large flash rate magnitudes predicted by the GEV, $VOL30$, and PIM schemes.

A number of different processes could have contributed to the observed rapid changes in flash rate. One possibility is the occurrence of brief but strong pulses in updraft intensity, found by many studies to accompany rapid increases in flash rate (e.g. Wiens et al. 2005).

3.3. PREDICTION OF FLASH RATES BASED ON UPDRAFT VARIABLES

Lightning flash rate was regressed against six indicators of updraft intensity to test whether brief pulses in updraft contributed to large changes in lightning flash rate observed in several storms. These indicators included the maximum observed updraft in the mixed-phase region (W_{max}), and the updraft volume greater than 5, 10, 15, and 20 m s^{-1} ($UV5$, $UV10$, $UV15$, $UV20$). Additionally, flash rate was regressed against the product of precipitating and non-precipitating ice mass flux (P_{flux}), to test the hypothesis of whether this flux product exhibited a control on flash rate (Deierling et al. 2008). A strong net flux of hydrometeors could lead to rapid bulk charge separation and possibly explain the transient jumps in lightning activity.

The results of the regressions are shown in Figures 3.9 and 3.10. None of these six parameters explains the variability in flash rate as well as GEV, $VOL30$, and PIM. P_{flux} is best correlated to flash rate (R^2 = 0.53) out of all the updraft parameters considered. A power-law parameterization was developed for P_{flux} since its relationship to flash rate was observed to be somewhat non-linear. A power-law relationship was also developed for W_{max} for comparison with the PR92W scheme. The modified W_{max} power-law scheme has a slope 2.4, less than the PR92W slope of 4.5. The smaller slope suggests that flash rates in Colorado storms are less sensitive to peak updraft than predicted by PR92W. These modified parameterizations were tested to understand their case-by-case behavior. Figures 3.11 and 3.12 show the predicted flash rate time series compared to observed flash rates. Generally speaking, the updraft schemes did not predict flash rate as well as the ice mass/echo volume schemes. Many similar errors were observed, including an inability to predict

large but brief flash rate fluctuations observed for 6 June 2012 storm 1 (Figure 3.11b) and 27 June 2012 (Figure 3.12a). A notable exception is 17 June 2013, for which the $UV20$ scheme predicts more of the observed flash rate variability (Figure 3.12c). Predominantly low flash rate storms (e.g. 5 June, 27 June, and 28 June 2012) were poorly predicted by the $UV15$ and $UV20$ schemes because updrafts within these storms rarely exceeded 15 m s^{-1}. Each updraft-based parameterization is summarized in Table 3.2.

A summary of the quantitative performance of the nine modified flash rate schemes discussed in this section and section 3.2 is given in Figure 3.13. The errors for each flash rate scheme are shown averaged over all Colorado storm volumes. The green bars represent normalized root mean square error (NRMSE), defined as the root mean square error divided by the range of observed flash rates. Blue bars represent normalized bias error (NBE). Immediately apparent is the superior performance of the ice mass/echo volume flash rate schemes compared to the updraft-based schemes. The GEV, $VOL30$, and PIM schemes all have NRMSE values below 15 percent; the best performing scheme is the $VOL30$ scheme with NRMSE of 11.3 percent. The updraft-based schemes ($UV5$, $UV10$, $UV15$, $UV20$, W_{max}, and P_{flux}) have average errors closer to 20 percent. The best-performing updraft-based scheme is the $UV10$ scheme, with NRMSE of 18.4 percent. The linear schemes (updraft volume, GEV, $VOL30$, and PIM) were unbiased flash rate estimators with NBE values of zero. The power-law schemes (W_{max} and P_{flux}), tended to under-predict flash rates in the mean, with NBE values between -5 and -10 percent. The power-law bias arises because while these schemes sometimes underestimated flash rate (e.g. 6 June 2012 storm 1), they rarely overestimated flash rate. The sensitivity of the power-law schemes allowed for lower flash rates to be predicted when storm parameter values were low. In contrast, the linear schemes tended to overestimate and underestimate flash rate equally.

3.4. DEVELOPMENT OF NEW FLASH RATE PARAMETERIZATIONS

Indicators of storm size (echo volumes) were found to be relatively good predictors of flash rate, but failed at times to predict rapid flash rate fluctuations. Indicators of core updraft strength ($UV15$ and $UV20$) sometimes better predicted short-term variability in lightning activity but were not useful for weaker storms lacking strong updrafts. An improved flash rate parameterization might therefore account for changes in storm size and updraft strength. This scheme must necessarily involve using two storm parameters to predict flash rate. To represent the effects of different storm processes, various combinations of storm parameters were related to flash rate using a least squares multiple linear regression technique. First, the graupel area within the mixed phase region (A_{grp}) and the maximum height of graupel detected (H_{grp}) were used to predict flash rate. A_{grp} accounts for storm size; precedent exists for examining hydrometeor areas in relation to charging processes and lightning (Lang and Rutledge 2002). Convective cloud height, represented here by H_{grp}, has been found to empirically scale with lightning activity and with peak updraft velocity (Williams 1985; Price and Rind 1992). H_{grp} and the maximum height of 30-dBZ are correlated to peak updraft for the storms analyzed in this study as well (Figure 3.14). Indicators of convective cloud height appear to relate to peak updraft because strong updrafts (> 5 m s^{-1}) exceed the terminal fall speed of graupel particles, resulting in graupel (or radar reflectivity) being lofted to high levels within a storm (Locatelli and Hobbs 1974). Graupel and reflectivity maximum heights are useful substitutes for updraft strength since they do not require knowledge of the three-dimensional wind field of a storm.

Multiple linear regression was performed between flash rate and maximum graupel area and height to develop a parameterization (referred to as A_{grp}-H_{grp}) of the form

$$f = \beta_0 \times A_{grp}^{\beta_1} \times H_{grp}^{\beta_2}, \tag{3.1}$$

where β_0, β_1, and β_2 are coefficients. Similar parameterizations were developed using various combinations of dBZ areas and maximum dBZ heights (A_{dBZ}-H_{dBZ}). These types of parameterizations will collectively be referred to as "area-height" schemes. Power-law relationships were developed so that the combined quantities A_{grp}-H_{grp} or A_{dBZ}-H_{dBZ} may together be considered as defining a "dynamic" echo volume. While GEV and $VOL30$ are single quantities with constrained dimensions, Equation 3.1 allows the area and height dimensions to evolve separately from one another, possibly exhibiting more variability in time.

A summary of the linear regression results for A_{grp}-H_{grp} and two A_{dBZ}-H_{dBZ} flash rate schemes is provided in Table 3.3. The A_{40}-H_{40} and A_{45}-H_{45} area-height schemes are shown because A_{40}-H_{40} exhibited some of the lowest errors for specific cases, and A_{45}-H_{45} had the lowest average error over all storm volumes (11.1 percent). Schemes based on other quantities, such as A_{35}-H_{35} and A_{35}-H_{30}, were also tested but are not shown because they performed similarly to the A_{grp}-H_{grp} scheme. A scheme based on graupel area and the maximum updraft (A_{grp}-W_{max}) was also developed in order to include an explicit indicator of updraft strength, but A_{grp}-W_{max} was not as good a predictor of flash rate as the other combined quantities (average error = 18.2 percent; compare to Figure 3.18). The A_{grp}-H_{grp}, A_{40}-H_{40}, and A_{45}-H_{45} storm parameter combinations were robustly correlated to total flash rate with R^2 values of 0.82, 0.78, and 0.65, respectively. Time series of flash rates predicted by these area-height schemes are shown in Figures 3.15-3.17. Flash rates predicted by the simpler GEV scheme are also shown for comparison. The multiple-parameter

schemes tend to predict flash rate trends similar to those predicted by the GEV scheme, but there are several significant improvements. The local maximum in flash rate observed at 21:55 UTC for 6 June 2012 storm 2 is well predicted, particularly by the A_{grp}-H_{grp} scheme (Figure 3.15c). A sharp increase in graupel maximum height occurred at this time (not shown), explaining why this peak was better predicted. Flash rate estimates are significantly improved for 22 June 2012 storm 2 (Figure 3.16c) and 17 June 2013 (Figure 3.17b) compared to the GEV scheme, which significantly overestimated flash rates for these two storms. For 6 June 2012 storm 3, the predicted flash rate peak still lags the observed peak by as much as 20 minutes (Figure 3.15d). However, the area-height schemes more closely estimated the magnitude of this peak than did the GEV scheme. The large flash rate peaks observed for 6 June 2012 storm 1 (Figure 3.15b) and 27 June 2012 (Figure 3.16d) are still not predicted. Aside from the flash rate peaks, however, the low flash rates observed for the majority of these storms' lifetimes are well predicted, especially by A_{40}-H_{40} and A_{45}-H_{45}.

To summarize the performance of the multiple-parameter schemes, error statistics are presented in Figure 3.18 in comparison to the average error of the GEV, PIM, and $VOL30$ schemes. The area-height schemes exhibit total average error comparable to the GEV, PIM, and $VOL30$ schemes. This result arises because although the area-height schemes performed better for many individual cases, for a few cases they introduced too much variability in predicted flash rates, resulting in larger errors. The average error of selected flash rate schemes for each individual case is plotted in Figure 3.19. From this plot, it is apparent that for some storms (e.g. 5 June 2012, 6 June 2012 storm 2, 22 June 2012 storm 2, 28 June 2012, and 17 June 2013), at least one of the area-height schemes had significantly lower error than the GEV scheme (teal bars), as well as the $VOL30$ and PIM schemes (not shown). For the 6 June storm 2, 22 June storm 2, 28 June, and 17 June 2013

cases, the average error of at least one area-height scheme was below 20 percent. For the 3 August 2013 case for which the errors were larger than for the GEV scheme, the area-height schemes predicted too much flash rate variability, but did not systematically overestimate or underestimate observed flash rates. These results suggest that the multiple-parameter schemes predict more of the temporal variability in flash rate than the simpler ice mass/echo volume schemes because the combined area and height quantities appear to more completely represent the processes controlling lightning flash rate.

It has been shown that simple, bulk storm parameters may be used to predict general flash rate behavior in most of the Colorado thunderstorms studied. Considerable modifications have been made to existing flash rate schemes (Table 1.1). In a general sense, large flash rates that persist for a long time (e.g., the second half of the 6 June 2012 storm 2 analysis period) and low flash rates (5 June 2012) are well predicted. Importantly, *transient, large flash rate maxima occurring in otherwise low to moderate flash rate storms were usually not well predicted*. Predicted flash rate time series for 6 June 2012 storm 1, 6 June 2012 storm 3, and 27 June 2012 depict good examples of this behavior. Evidently, simple indicators of storm size, robustness of mixed phase process, and updraft intensity do not explain all of the flash rate variability observed in these storms. For the purpose of the successful prediction of LNO_x on storm time scales, this temporal flash rate variability should ideally be better predicted.

3.5. Application to Alabama thunderstorms

The flash rate parameterization schemes discussed in sections 3.2, 3.3, and 3.4 were tested against observations of four Alabama storms documented during DC3 (Table 2.2). Figure 3.20 shows the average error of selected flash rate schemes for each of the Alabama cases and Figure 3.21 shows flash rate time series predicted by the GEV, $VOL30$, and PIM schemes versus

observed flash rates. For all storms except 14 June 2012, flash rates were overestimated by large margins. For each Alabama case, average errors of most of the schemes almost always reached 40 percent and sometimes exceed 60 percent. From Figure 3.21a, the PIM scheme overestimated peak flash rates by more a factor of three for 18 May 2012 and by a factor of five for 21 May 2012 (Figure 3.21b). For the 14 June 2012 storm only, flash rates were predicted well by the GEV scheme. The 18 May, 21 May, and 11 June Alabama cases produced median flash rates below 10 per minute, which has been found to be typical of many Alabama storms (Fuchs 2014). In contrast, the 14 June case produced a median flash rate of 18 per minute, atypical lightning behavior for the Alabama domain. The 14 June case was also the only storm with a maximum flash rate (50 per minute) comparable to some of the Colorado storms studied.

Figure 3.22 shows the performance of the updraft-based flash rate schemes for the 18 May and 21 May 2012 Alabama storms. Generally, updraft-based schemes overestimated flash rate as well. The W_{max} scheme predicted the later flash rate peak for 18 May (23:00 UTC) fairly well, but it predicted an un-observed flash rate peak at 20:29 UTC for 21 May 2012. The P_{flux} scheme tended to overestimate flash rate for both storms, but predicted the overall flash rate trends well. The $UV15$ and $UV20$ schemes predicted nearly constant flash rates, since updrafts in the Alabama storms infrequently exceeded 15 m s^{-1}. This result indicates that $UV15$ and $UV20$ are not ideal parameters to predict flash rate across different regions with significantly different thunderstorm characteristics. Updrafts greater than 15 m s^{-1} appear to occur frequently only in the more vigorous Colorado thunderstorms documented by this study.

Finally, the multiple-parameter flash rate schemes based on the maximum area and maximum height of graupel, and the maximum area and height of 40- and 45-dBZ, were tested (Figure 3.23). The A_{40}-H_{40} scheme overestimated peak flash rates for 18 May 2012 (Figure 3.23a) and 14 June

2012 (Figure 3.23d), but predicted flash rates generally well for the other two storms. The A_{grp}-H_{grp} schemes and A_{45}-H_{45} schemes overestimated flash rates for all Alabama storms, especially peak flash rates. These overestimated flash rate peaks are explained by the behavior of maximum graupel and dBZ heights for the Alabama storms. For 18 May 2012, there were several sudden increases in the maximum height of graupel and maximum dBZ heights corresponding in time to sharp peaks predicted by the area-height schemes (not shown). The maximum height of graupel for this storm reached 13 km, comparable to maximum height of graupel observed in many of the Colorado storms. However, these increases in graupel height were accompanied by only modest increases in flash rate. For 14 June 2012, maximum graupel height reached an astounding 16 km, resulting in over-estimation of flash rates. Importantly, however, the Alabama dataset was gridded to 1.0 km instead of 0.5 km, possibly resulting in increased uncertainty in the absolute maxima of hydrometeor and dBZ heights. This coarser vertical resolution may partly explain the sometimes-poor performance of the area-height schemes when applied to Alabama storms.

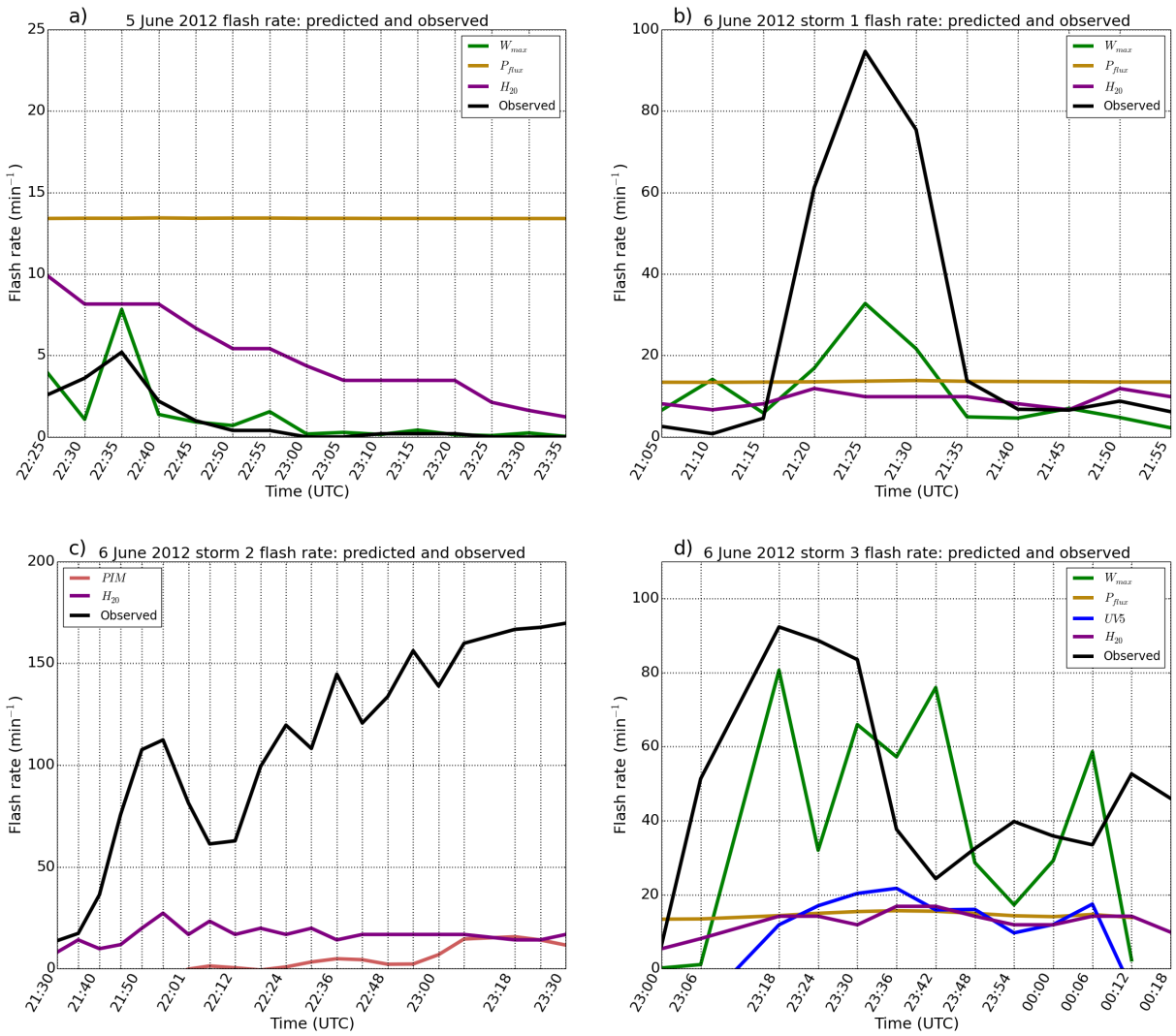

FIG. 3.1. Time series of observed total lightning flash rate (black) for a) 5 June 2012, b) 6 June 2012 storm 1, c) 6 June 2012 storm 2, and d) 6 June 2012 storm 3 compared to flash rates predicted by existing flash rate-storm parameter relationships: PR92W (green), D08 (blue), D08F (gold), D08P (pink), and PR92H (purple). Predicted flash rates for a given parameterization are only shown if they fell within the flash rate range seen on each plot.

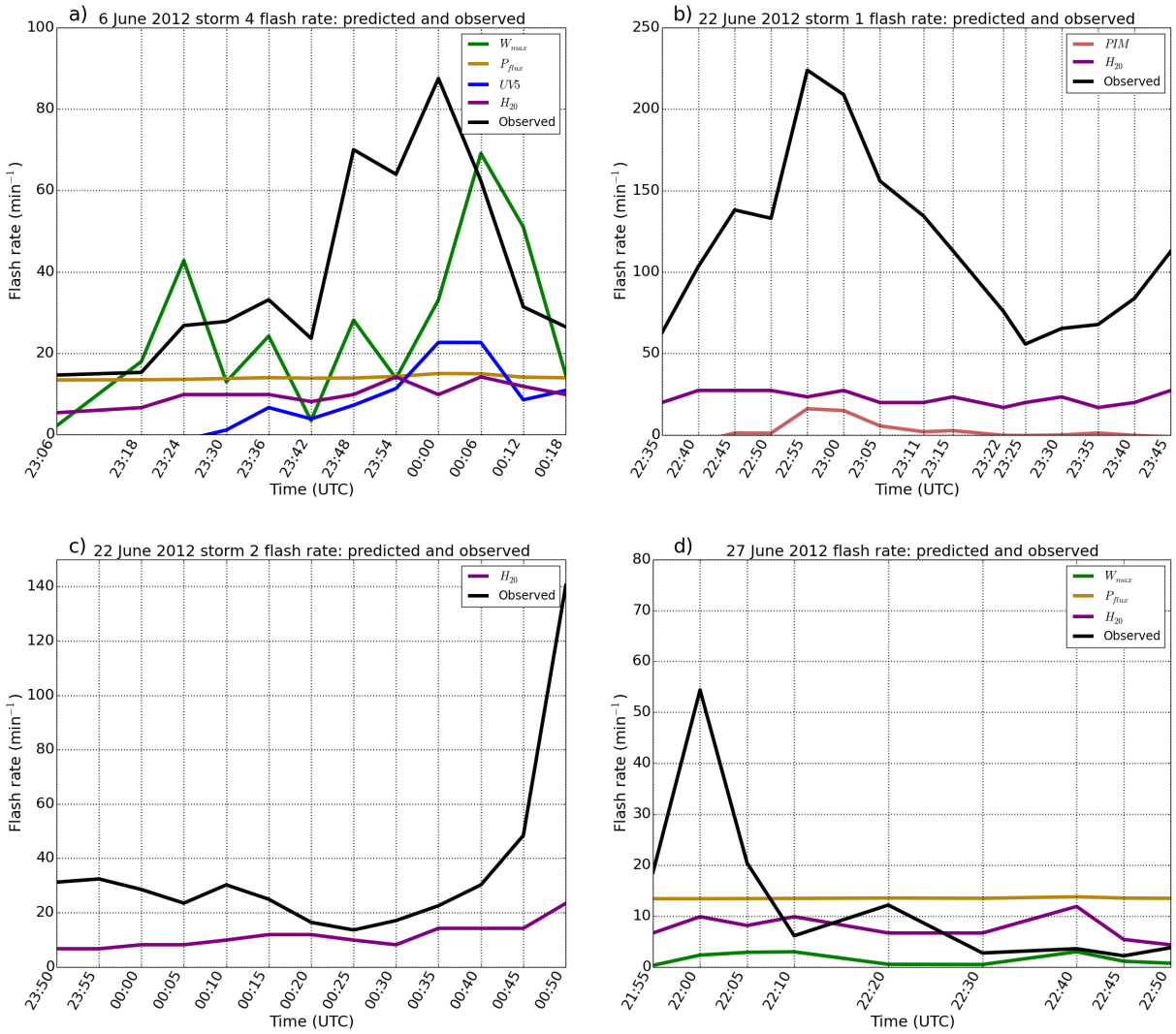

FIG. 3.2. As in Figure 3.1 but for a) 6 June 2012 storm 4, b) 22 June 2012 storm 1, c) 22 June 2012 storm 2, and d) 27 June 2012.

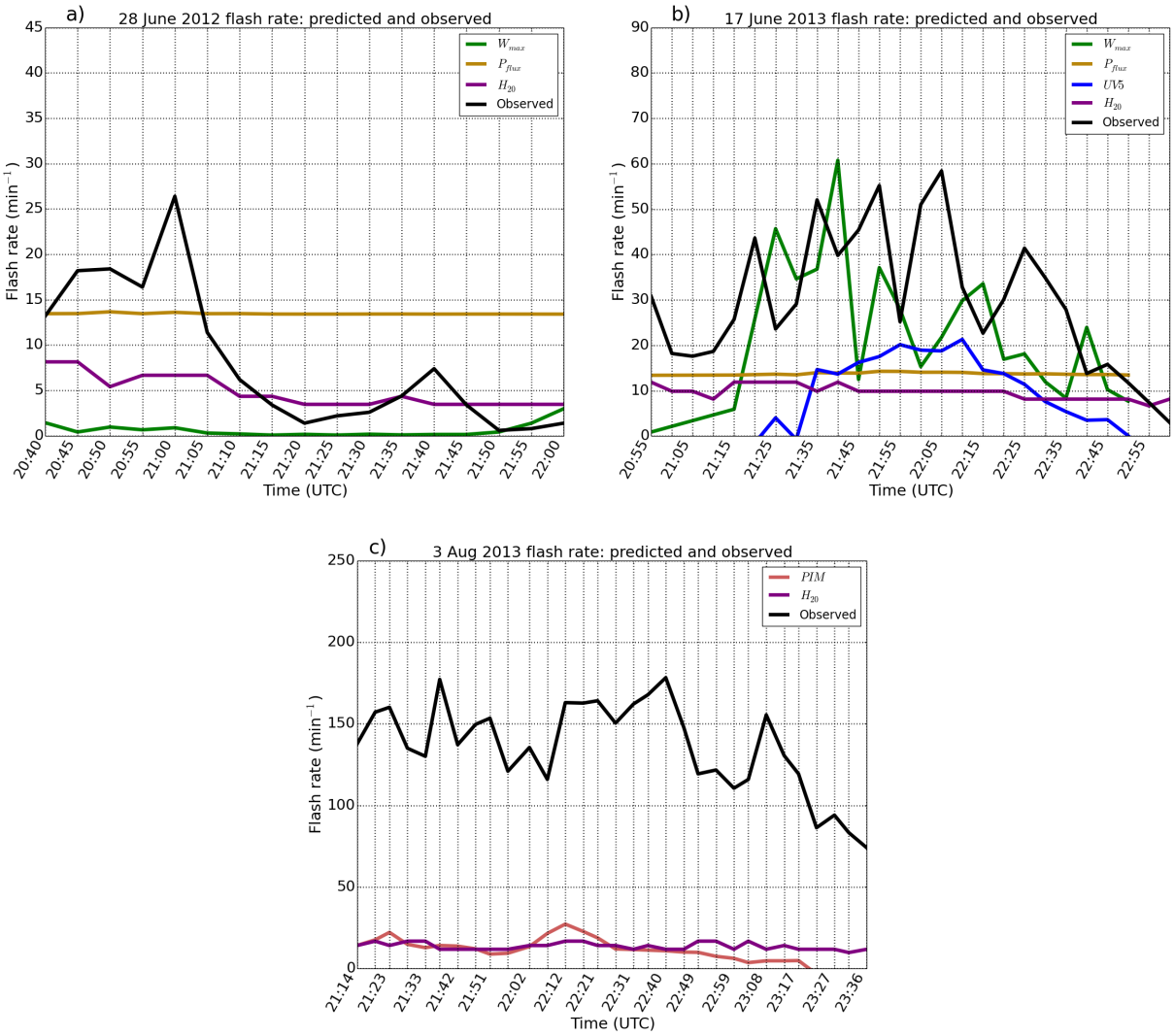

FIG. 3.3. As in Figure 3.1 but for a) 28 June 2012, b) 17 June 2013, and c) 3 August 2013.

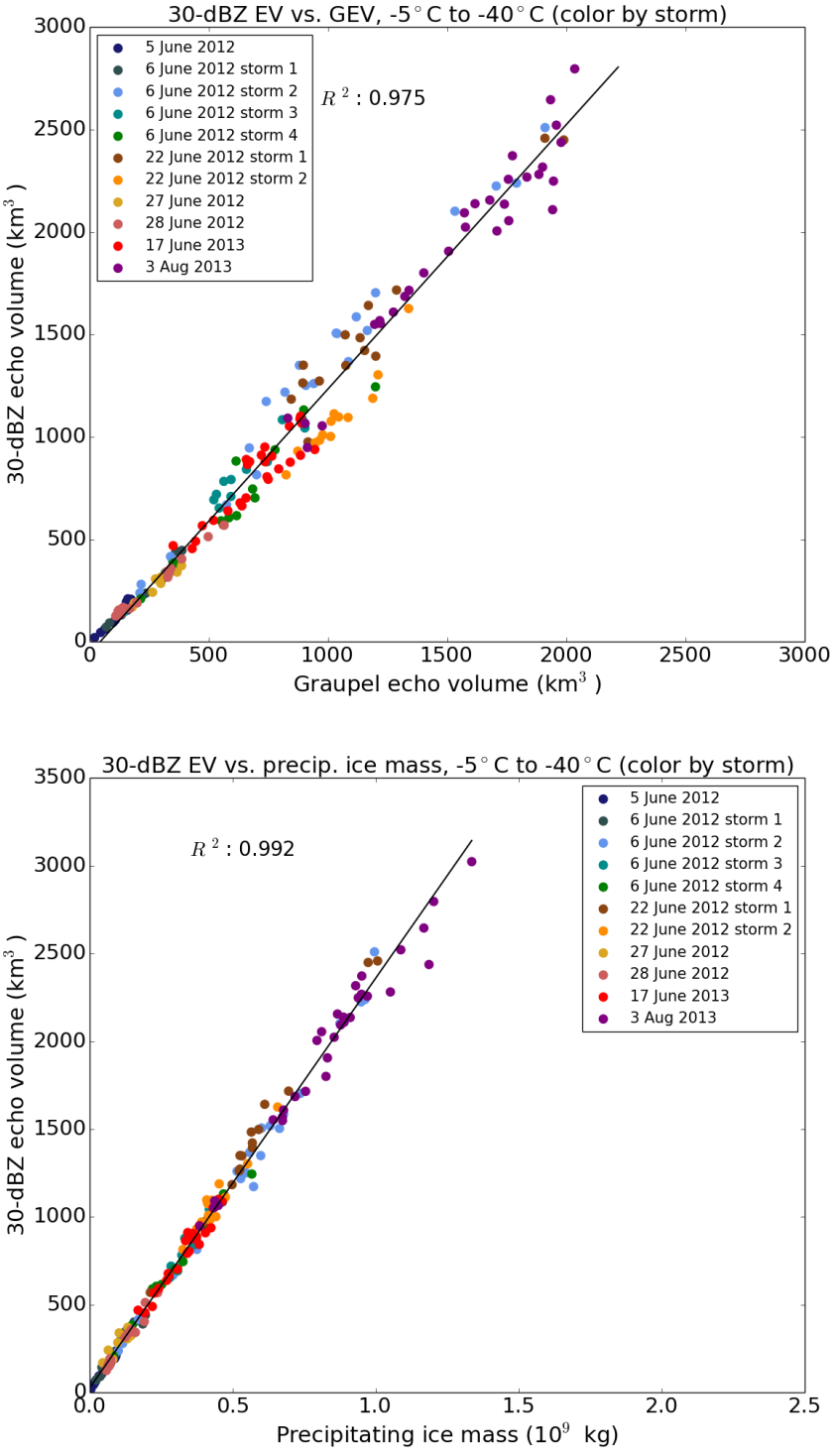

FIG. 3.4. Scatterplots of 30-dBZ echo volume versus graupel echo volume (top) and 30-dBZ echo volume versus precipitating ice mass (bottom) for all Colorado storm volumes. Points representing storm volumes are colored by the corresponding case study. These case study color conventions will be used for all subsequent scatter plots. The solutions to least squares fits are shown by the black lines. The coefficient of determination (R^2) for each fit is indicated.

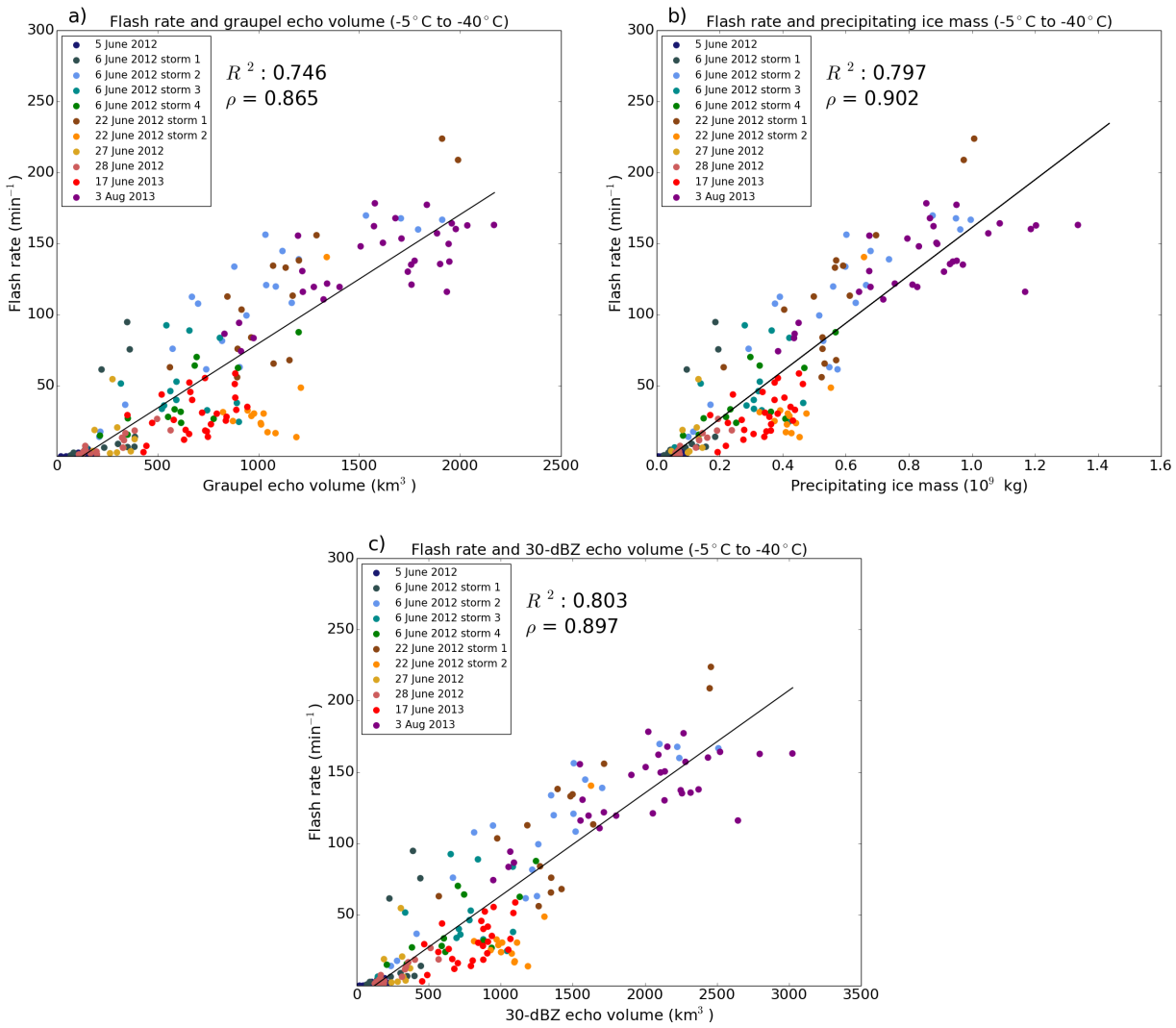

FIG. 3.5. Scatterplots of total lightning flash rate for all cases versus (a) graupel echo volume, (b) precipitating ice mass, and (c) 30-dBZ echo volume between $-5°\mathrm{C}$ and $-40°\mathrm{C}$. The solution to the least squares fits are shown by the black lines. R^2 values for each fit as well as the Spearman rank correlation coefficient (ρ) are indicated in each panel.

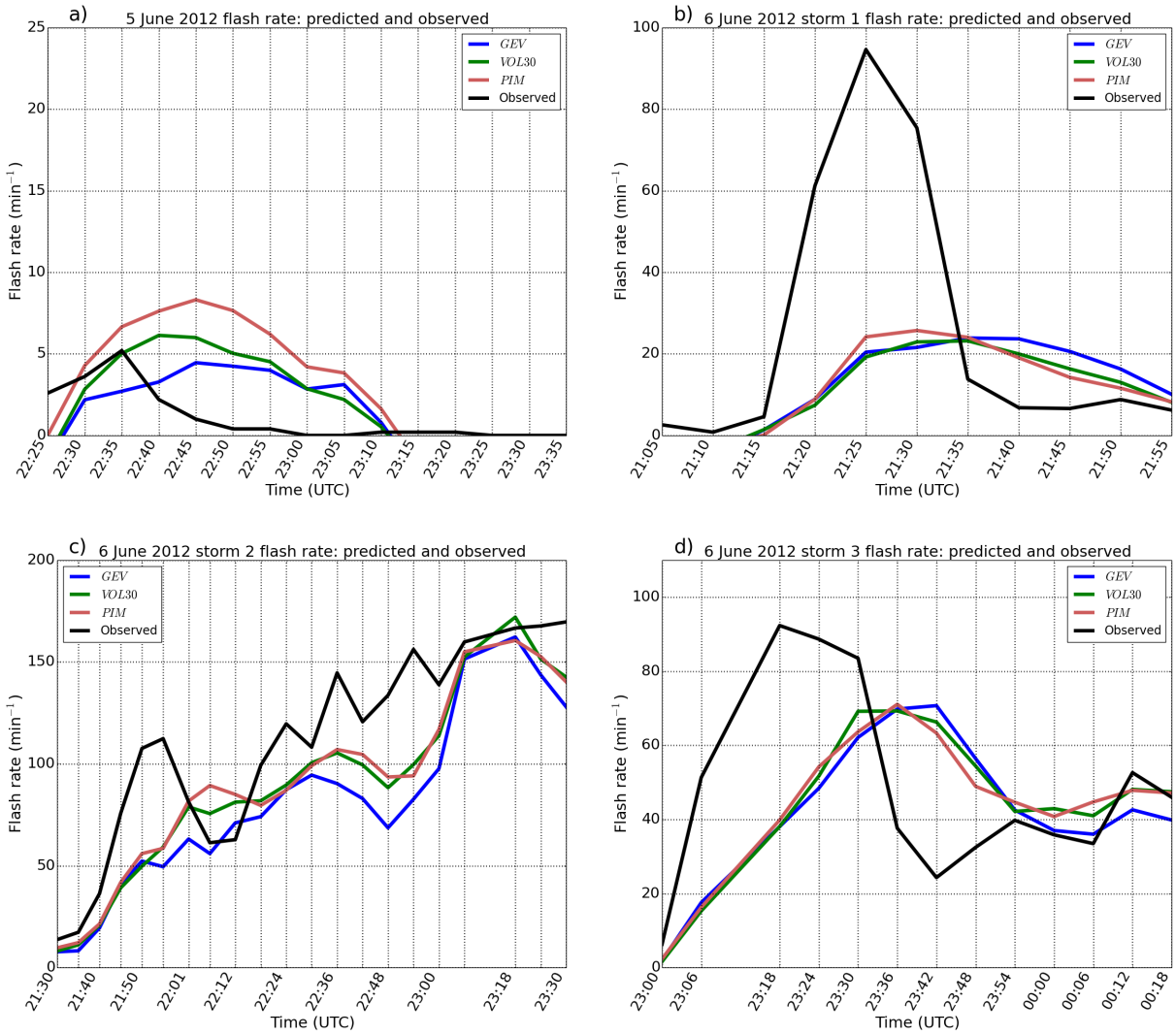

FIG. 3.6. Time series of observed total lightning flash rate (black) for a) 5 June 2012, b) 6 June 2012 storm 1, c) 6 June 2012 storm 2, and d) 6 June 2012 storm 3 compared to flash rates predicted by parameterizations based on the graupel echo volume (blue), the 30-dBZ echo volume (green) and the precipitating ice mass (pink) developed from the DC3/CHILL-MIE dataset.

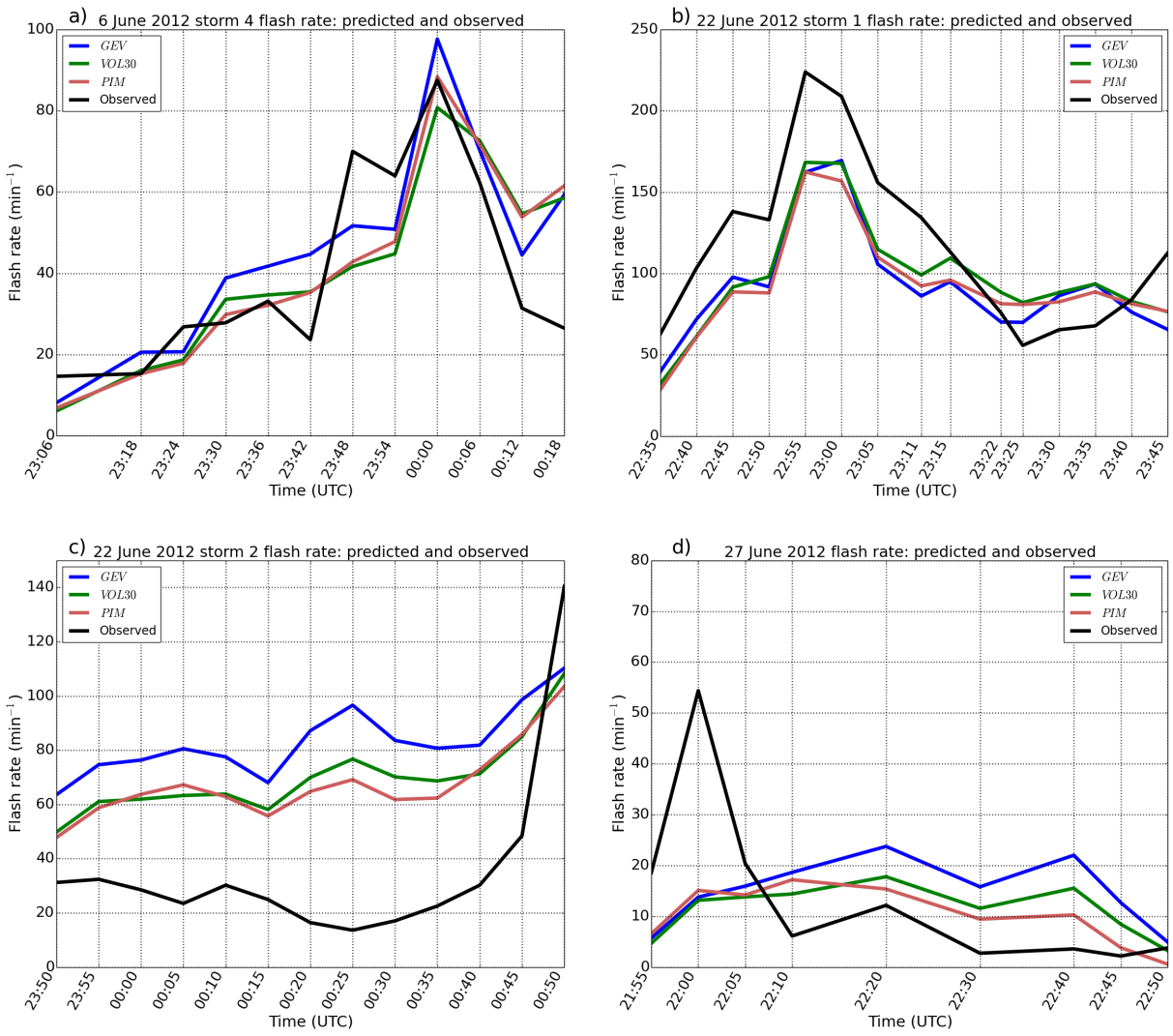

FIG. 3.7. As in Figure 3.6 but for a) 6 June 2012 storm 4, b) 22 June 2012 storm 1, c) 22 June 2012 storm 2, and d) 27 June 2012.

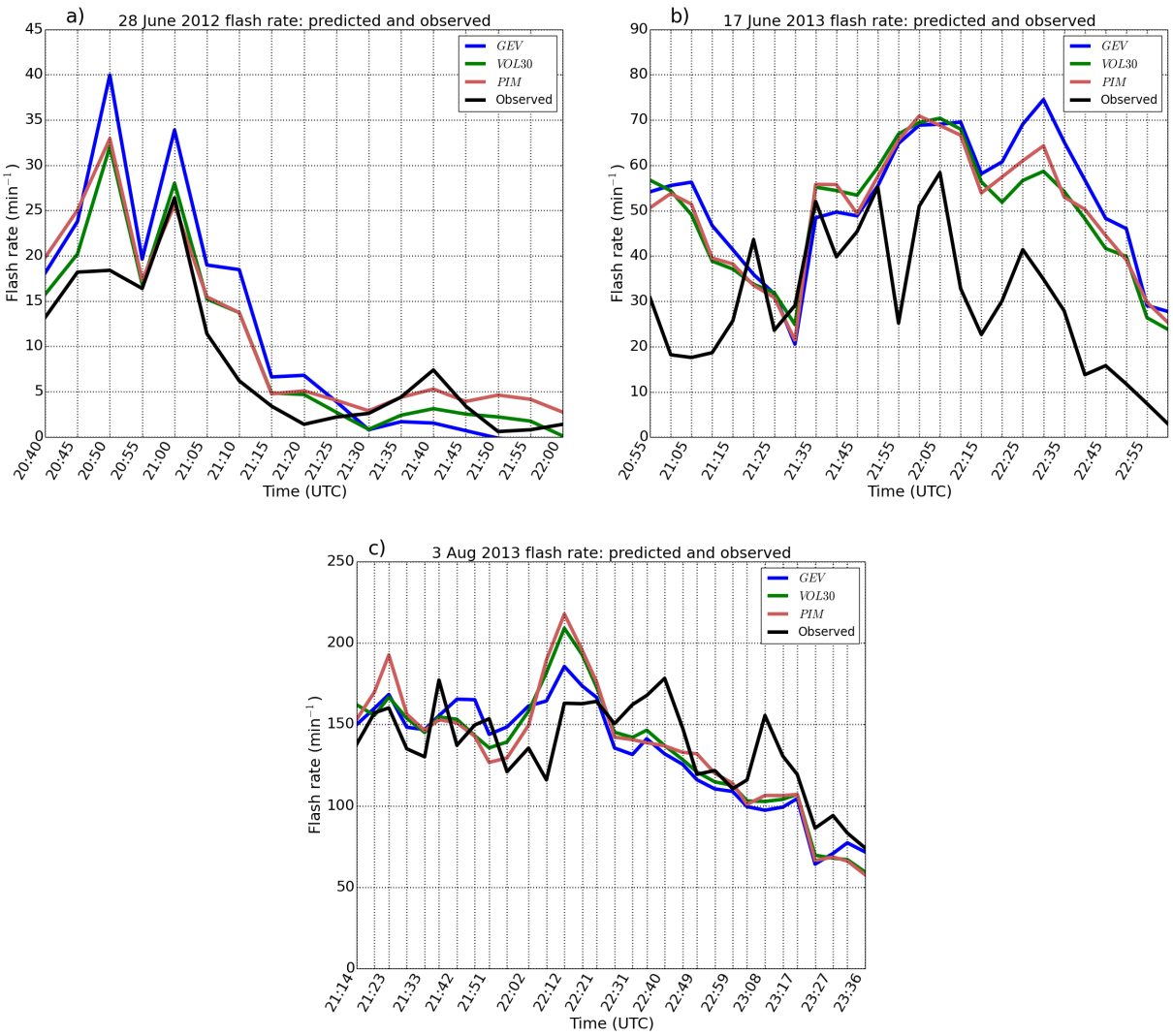

FIG. 3.8. As in Figure 3.6 but for a) 28 June 2012, b) 17 June 2013 and c) 3 August 2013.

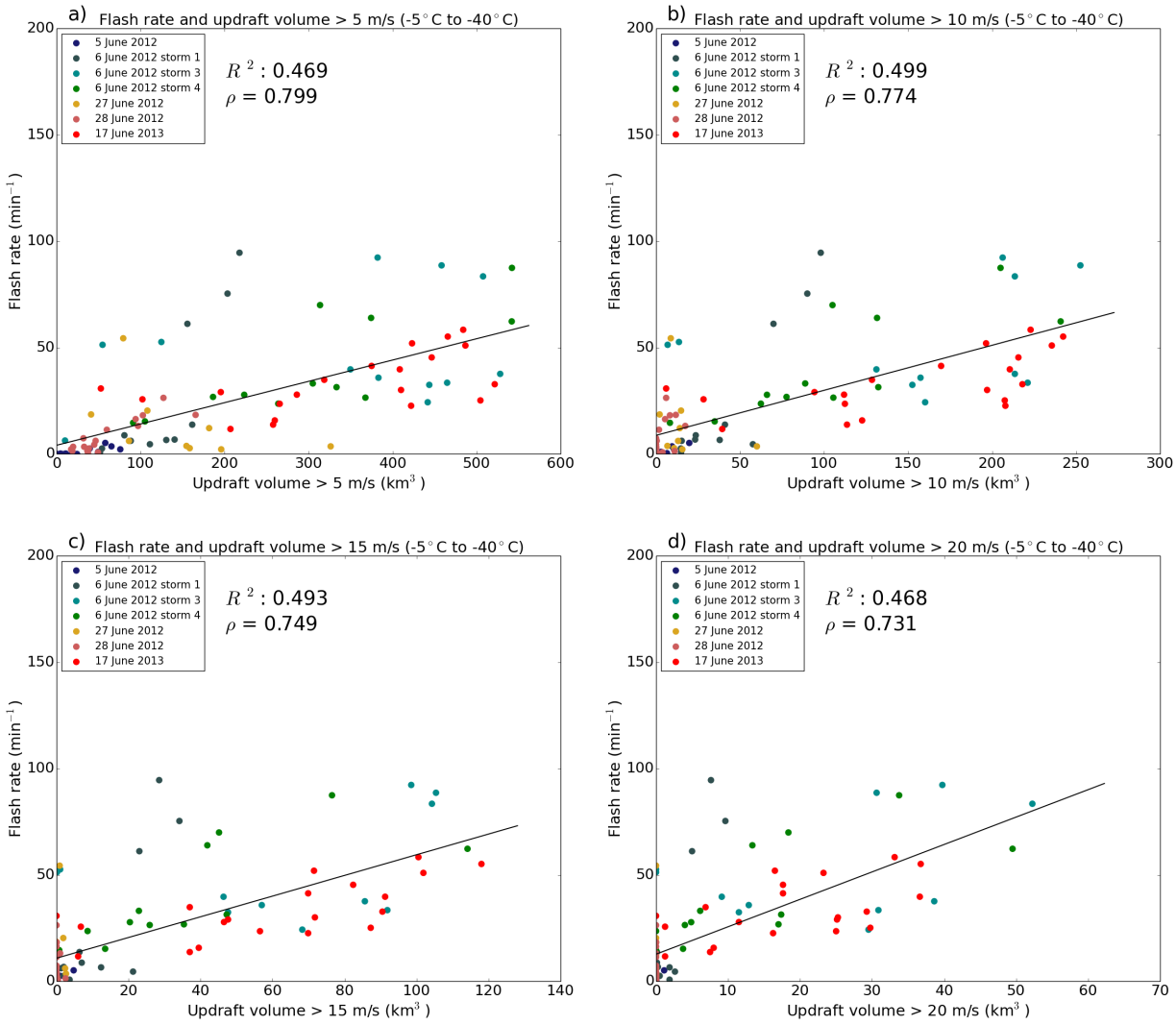

FIG. 3.9. Scatterplots of total lightning flash rate versus a) updraft volume $>$ 5 m s^{-1}, b) updraft volume $>$ 10 m s^{-1}, c) updraft volume $>$ 15 m s^{-1} and d) updraft volume $>$ 20 m s^{-1} . The solution to the least squares fits are shown by the black lines. R^2 values and the Spearman rank correlation coefficient (ρ) are indicated in each panel.

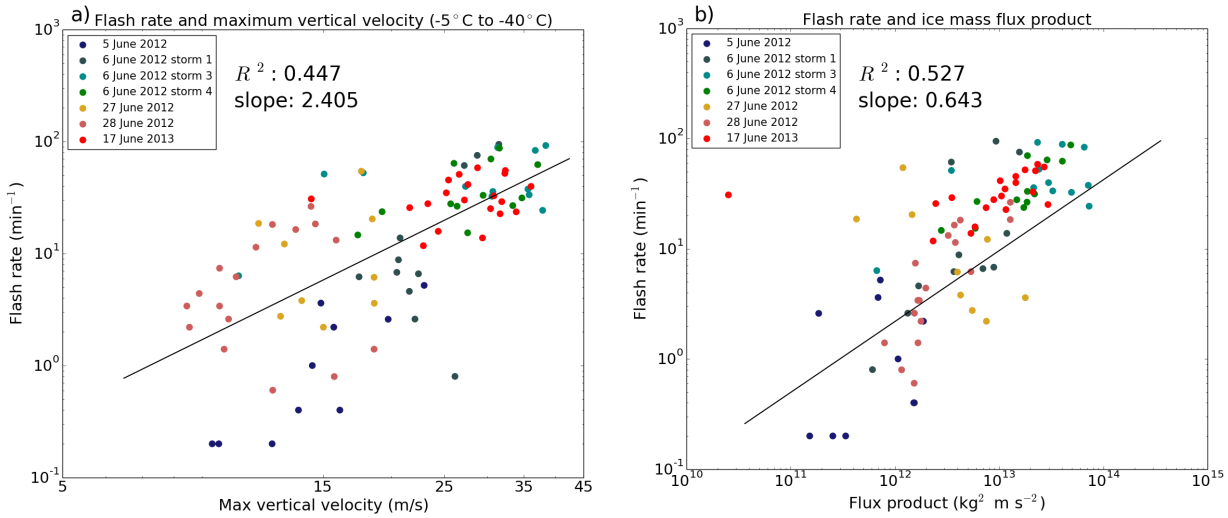

FIG. 3.10. As in Figure 3.9, but for a) maximum updraft velocity and b) the product of precipitating and non-precipitating ice mass flux. R^2 values and slopes of the power-law fits are indicated.

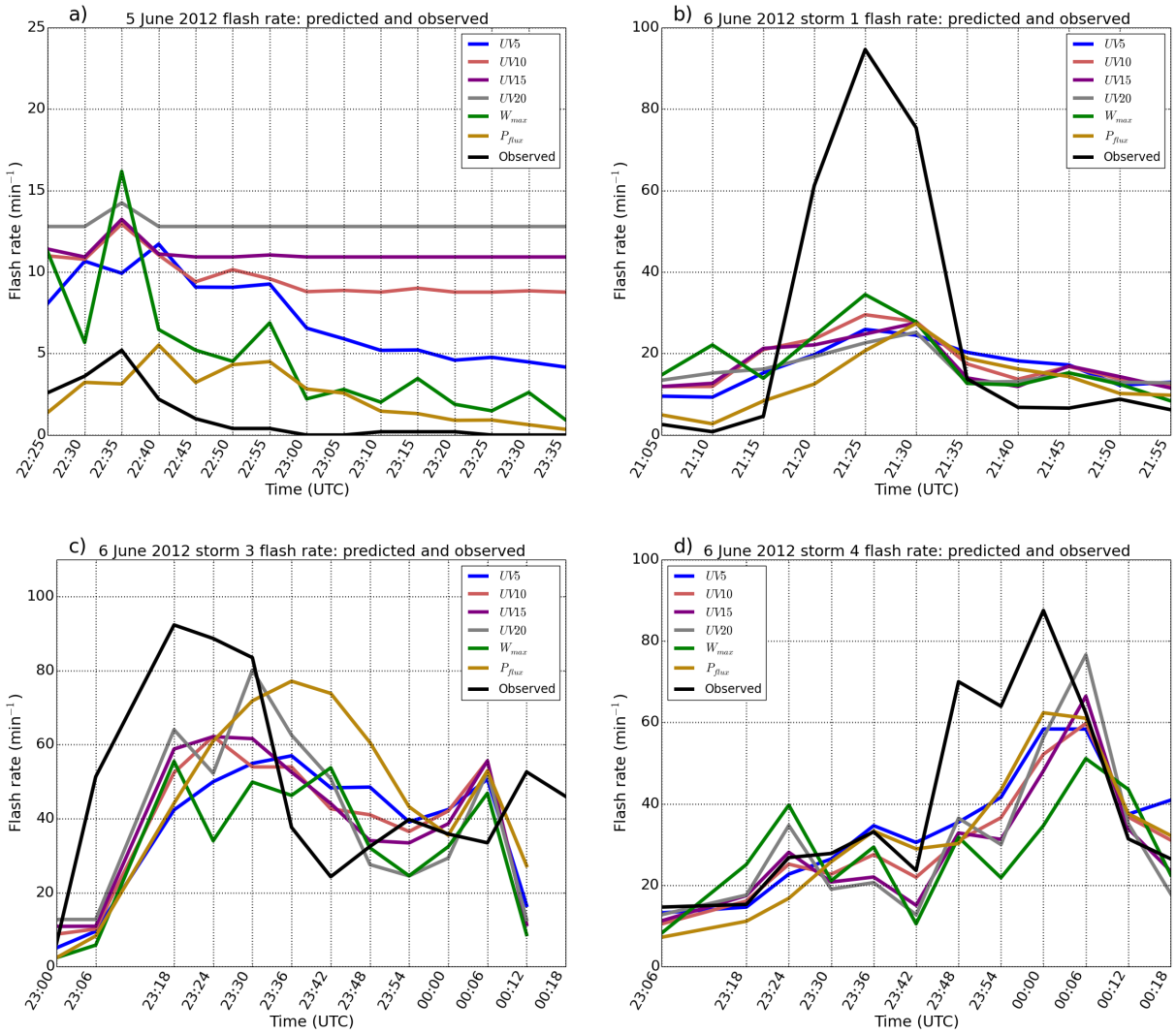

FIG. 3.11. Time series of observed total lightning flash rate (black) for a) 5 June 2012, b) 6 June 2012 storm 1, c) 6 June 2012 storm 3, and d) 6 June 2012 storm 4 compared to flash rates predicted by parameterizations based on the updraft volume > 5 m s^{-1} (blue), updraft volume > 10 m s^{-1} (pink), updraft volume > 15 m s^{-1} (purple), updraft volume > 20 m s^{-1} (gray), maximum updraft velocity (green), and the product of precipitating and non-precipitating ice mass flux (gold).

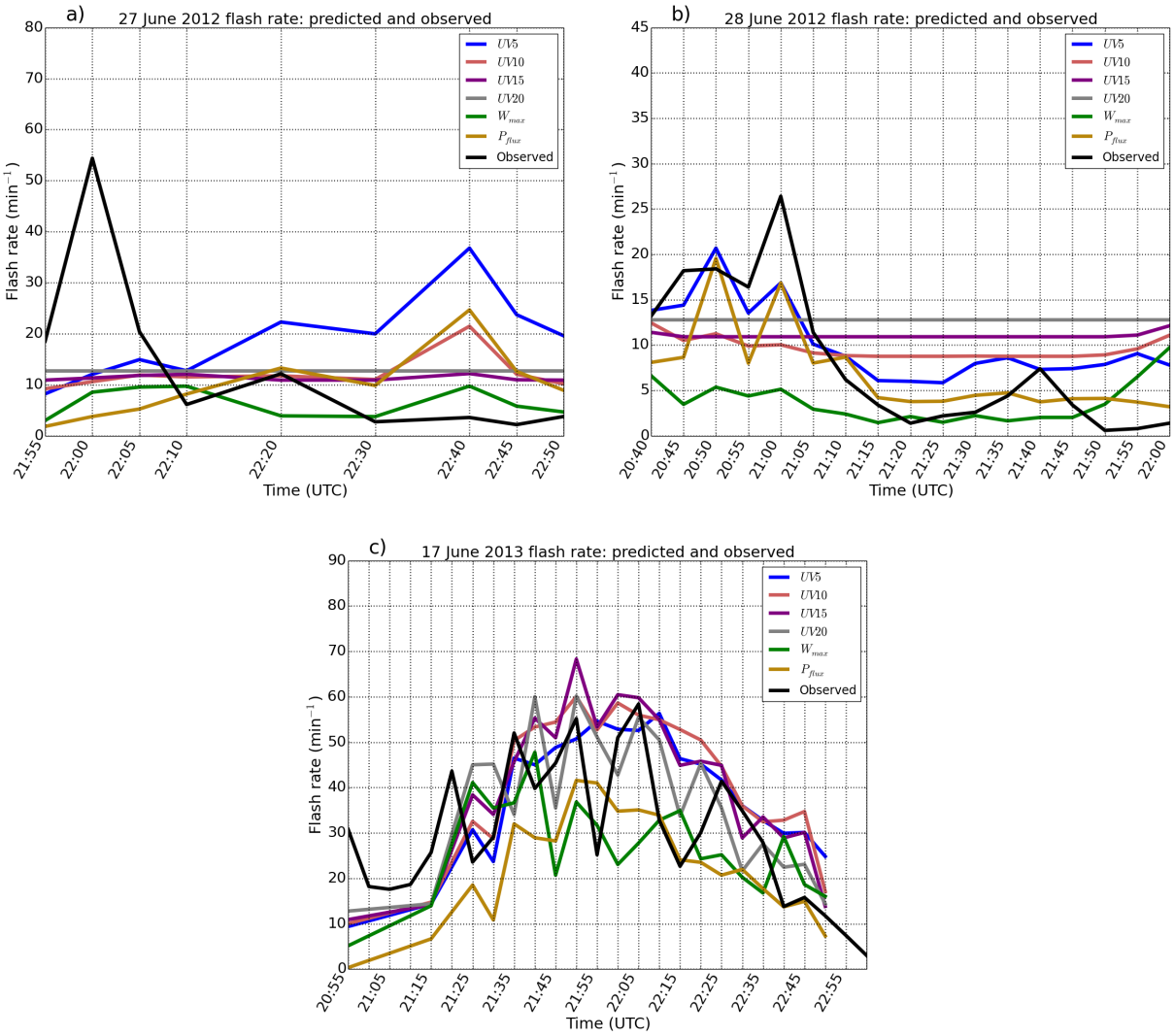

FIG. 3.12. As in Figure 3.11 but for a) 27 June 2012 b) 28 June 2012, and c) 17 June 2013.

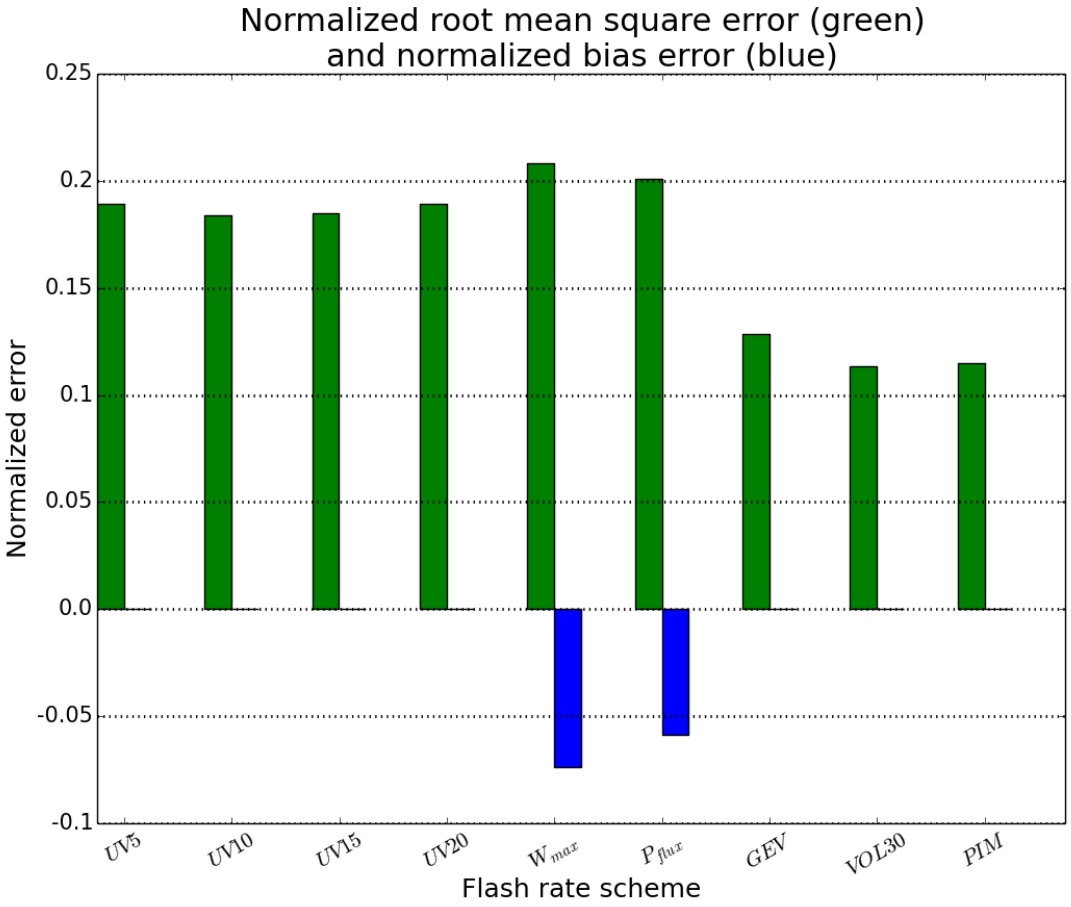

FIG. 3.13. Bar plot of normalized root mean square error (green) and normalized bias error (blue) for each modified single-parameter flash rate parameterization. The bars indicate the average error of each flash rate scheme over all Colorado storm volumes.

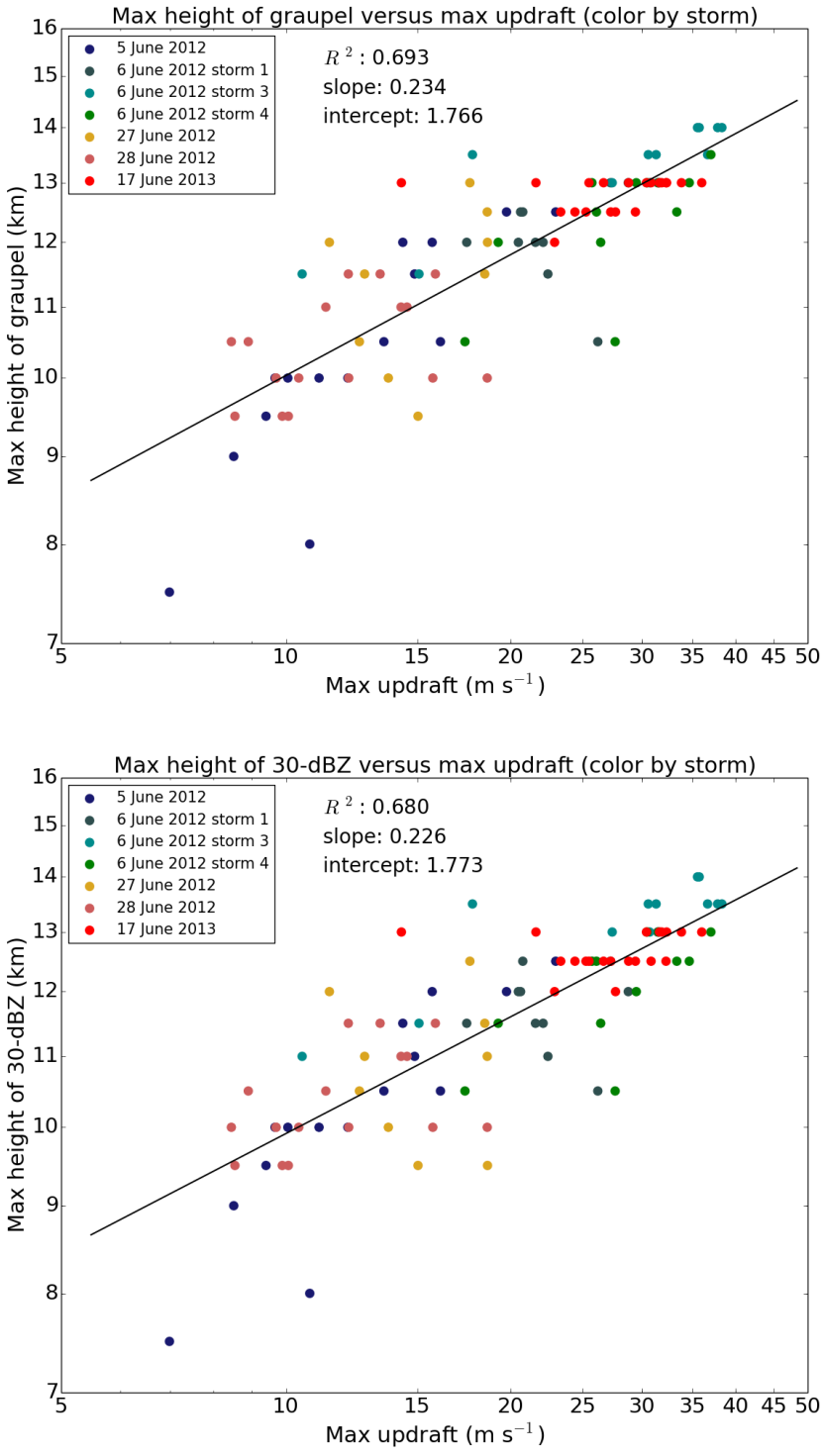

FIG. 3.14. Scatter plots of maximum height of graupel versus maximum updraft velocity (top) and maximum height of 30-dBZ versus maximum updraft velocity (bottom) for all Colorado storm volumes. The solutions to the least squares fits are shown by the black lines. The coefficient of determination (R^2), slope, and intercept of the fits are indicated in each panel.

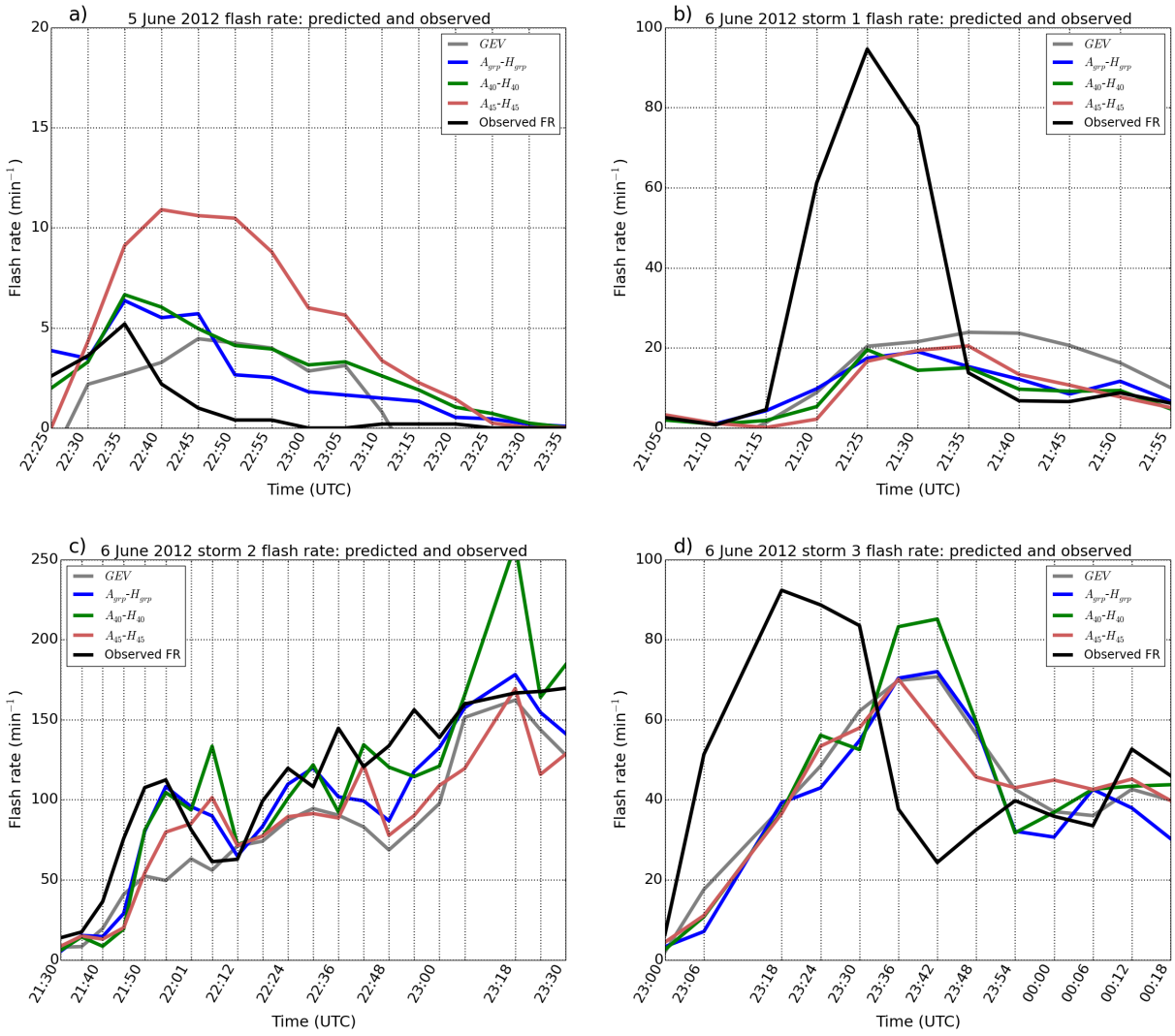

FIG. 3.15. Time series of observed total lightning flash rate (black) for a) 5 June 2012, b) 6 June 2012 storm 1, c) 6 June 2012 storm 2, and d) 6 June 2012 storm 3 compared to flash rates predicted by parameterizations based on graupel echo volume (gray), maximum graupel area and graupel height (blue), 40-dBZ area and maximum height (green), and 45-dBZ area and maximum height (pink).

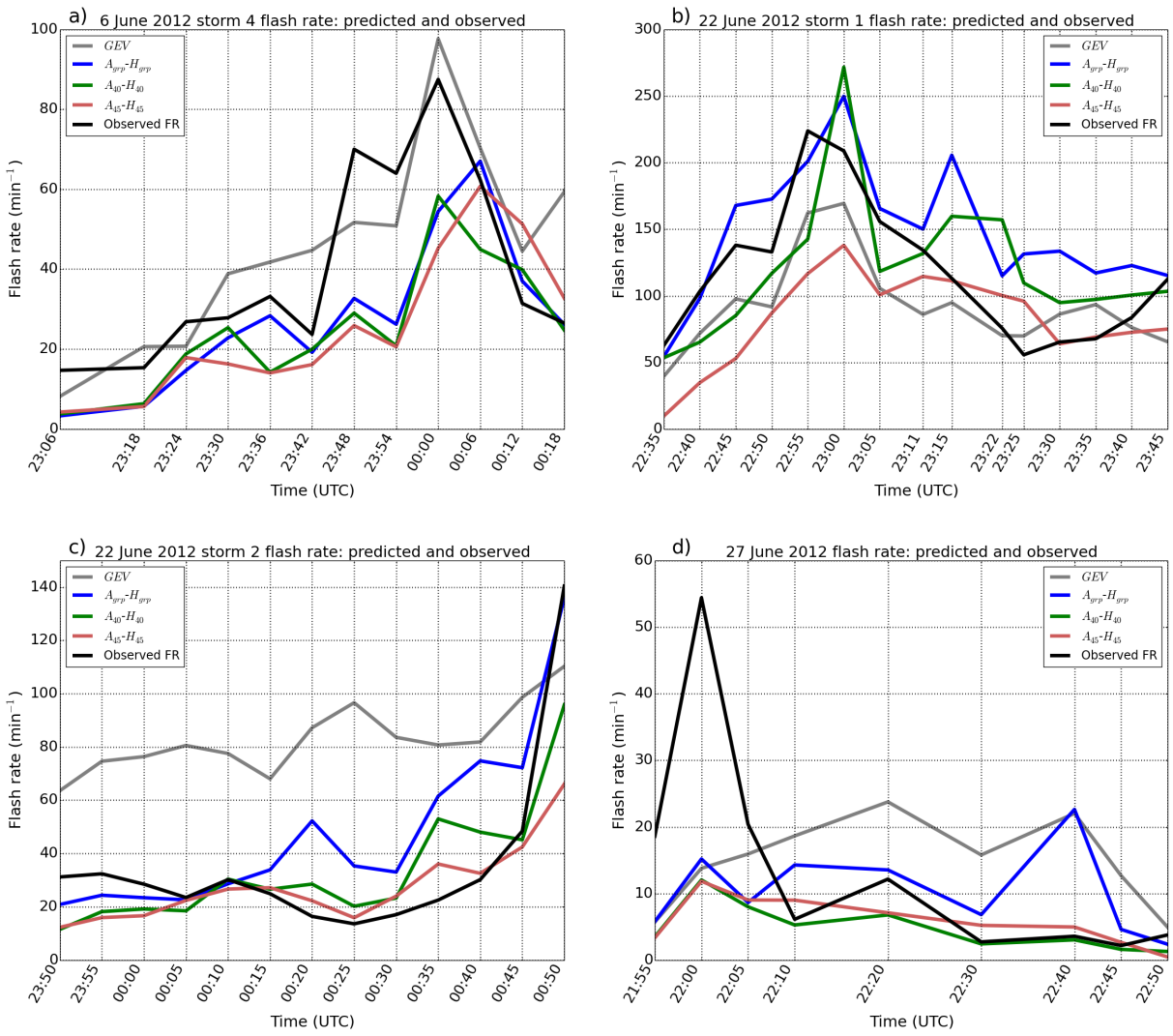

FIG. 3.16. As in Figure 3.15 but for a) 6 June 2012 storm 4, b) 22 June 2012 storm 1, c) 22 June 2012 storm 2, and d) 27 June 2012.

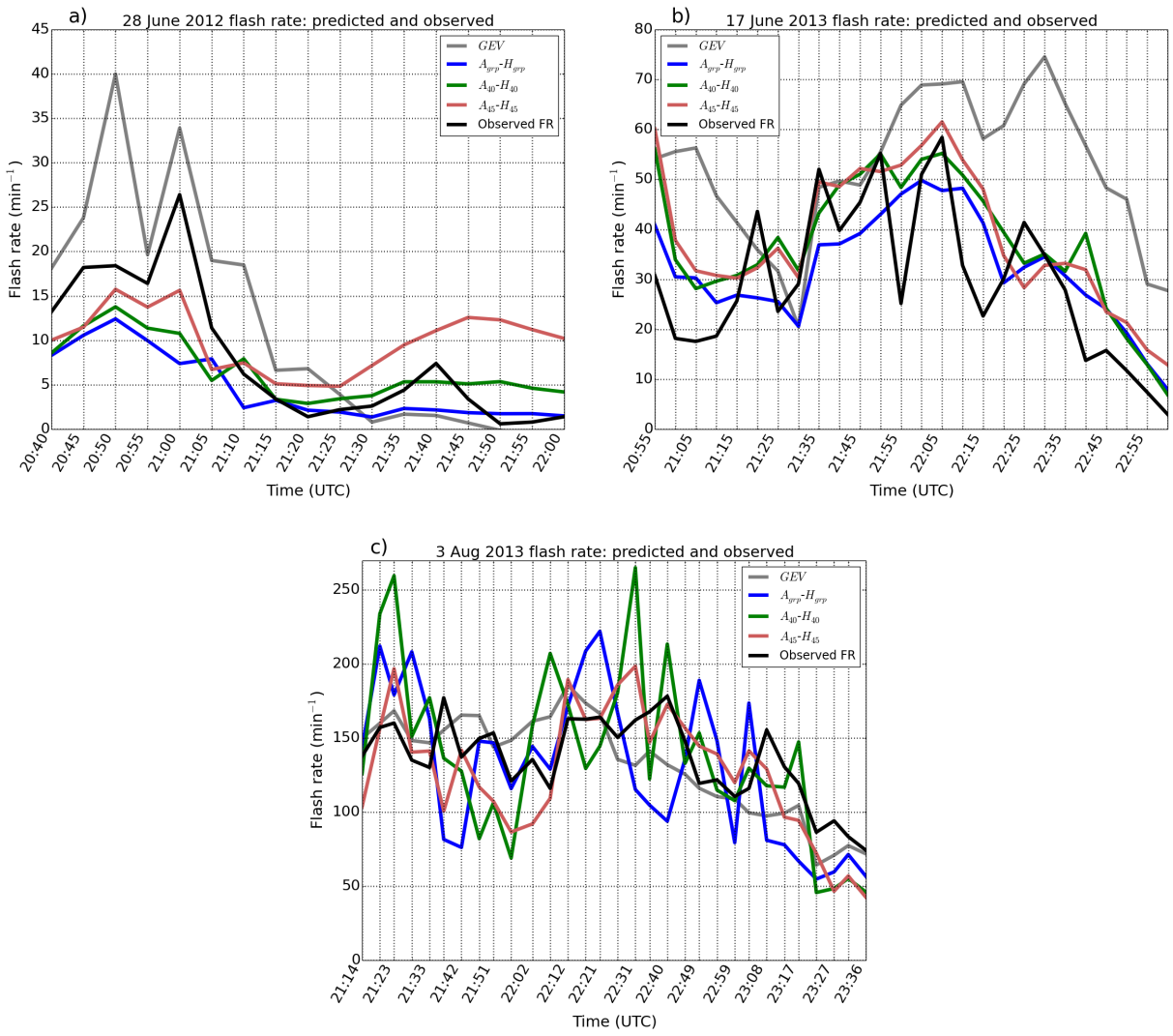

FIG. 3.17. As in Figure 3.15 but for a) 28 June 2012, b) 17 June 2013 and c) 3 August 2013.

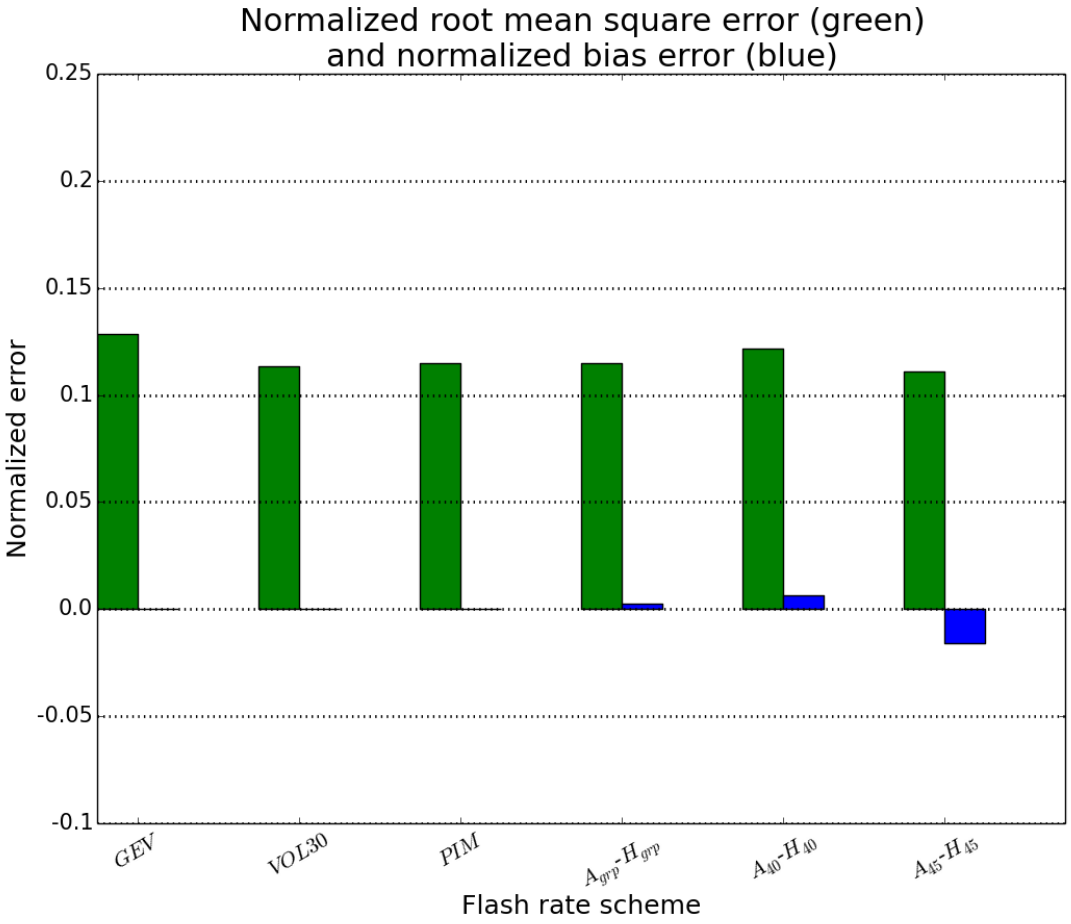

FIG. 3.18. Bar plot of normalized root mean square error (green) and normalized bias error (blue) for each modified linear flash rate parameterization based on ice mass/echo volumes (GEV, $VOL30$, and PIM) compared to error statistics for new multiple-parameter power-law schemes (A_{grp}-H_{grp}, A_{40}-H_{40}, and A_{45}-H_{45}). The bars indicate the average error for each flash rate scheme over all Colorado storm volumes.

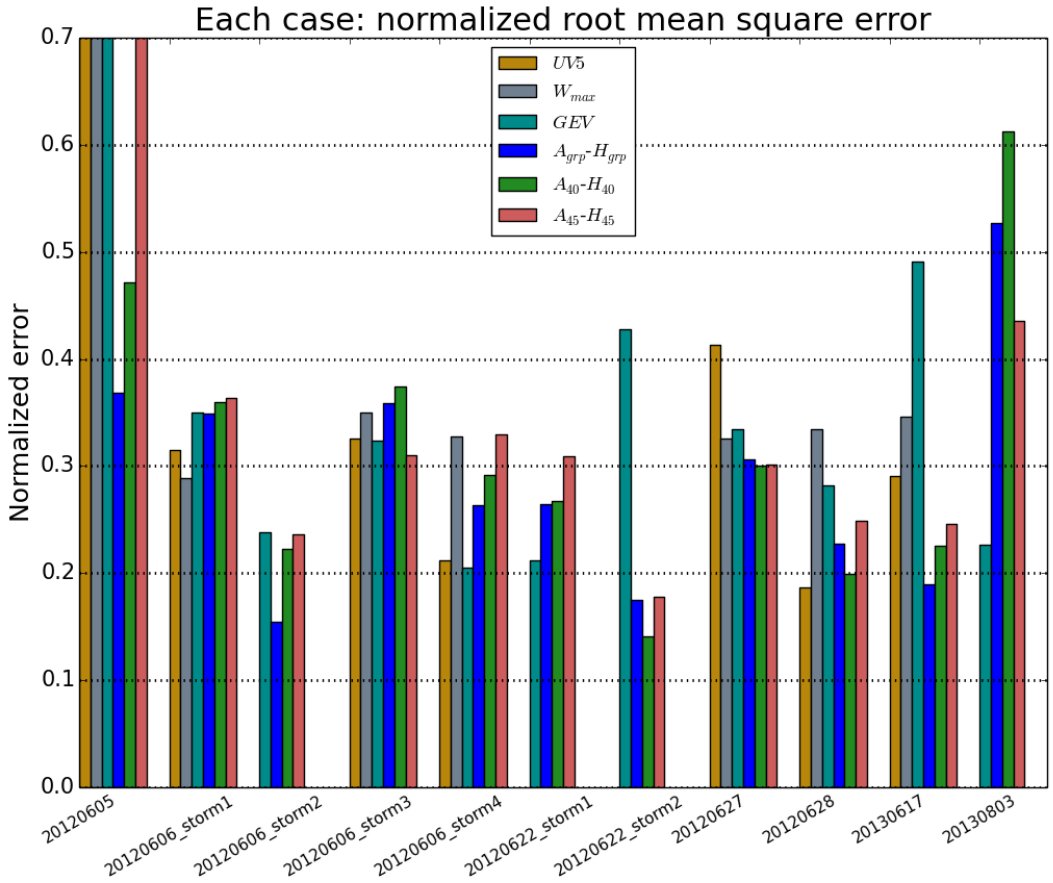

FIG. 3.19. Bar plot of normalized root mean square error (NRMSE) for six selected flash rate parameterization schemes: $UV5$ (gold), W_{max} (gray), GEV (teal), A_{grp}-H_{grp} (blue), A_{40}-H_{40} (green), and A_{45}-H_{45} (pink). Calculated average errors for each scheme are plotted for each Colorado storm.

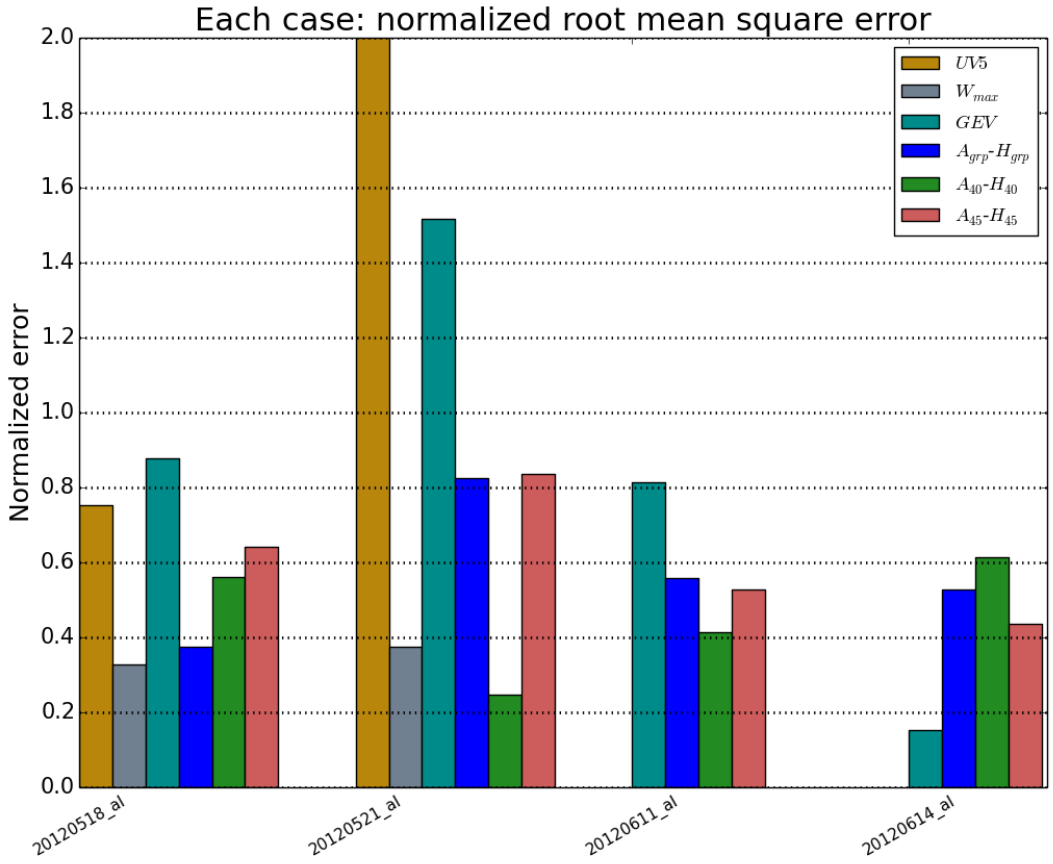

FIG. 3.20. As in Figure 3.19, but for all Alabama storms studied.

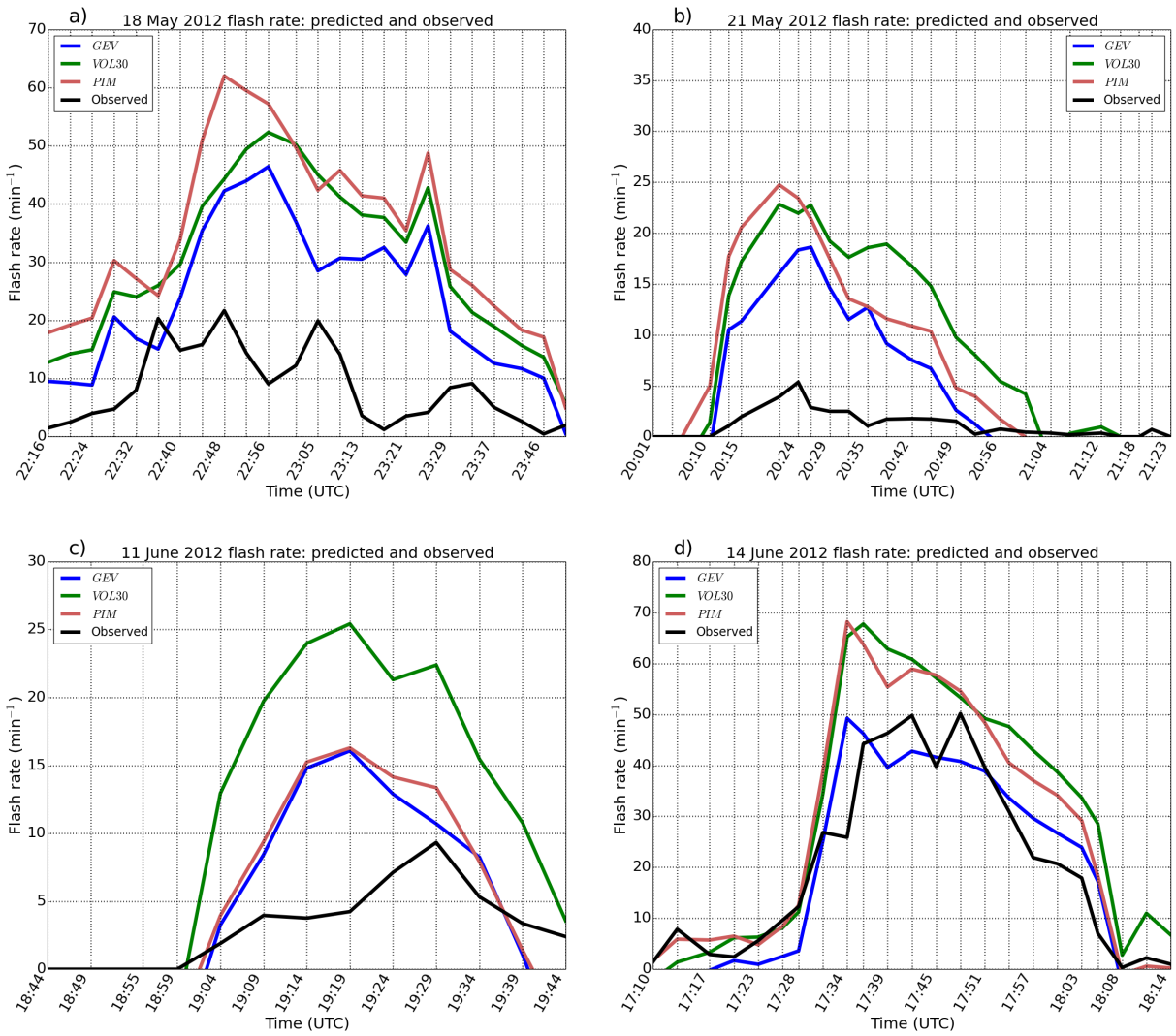

FIG. 3.21. Time series of observed total lightning flash rate (black) for a) 18 May 2012, b) 21 May 2012, c) 11 June 2012, and d) 14 June 2012 compared to flash rates predicted by parameterizations based on the graupel echo volume (blue), the 30-dBZ echo volume (green) and the precipitating ice mass (pink).

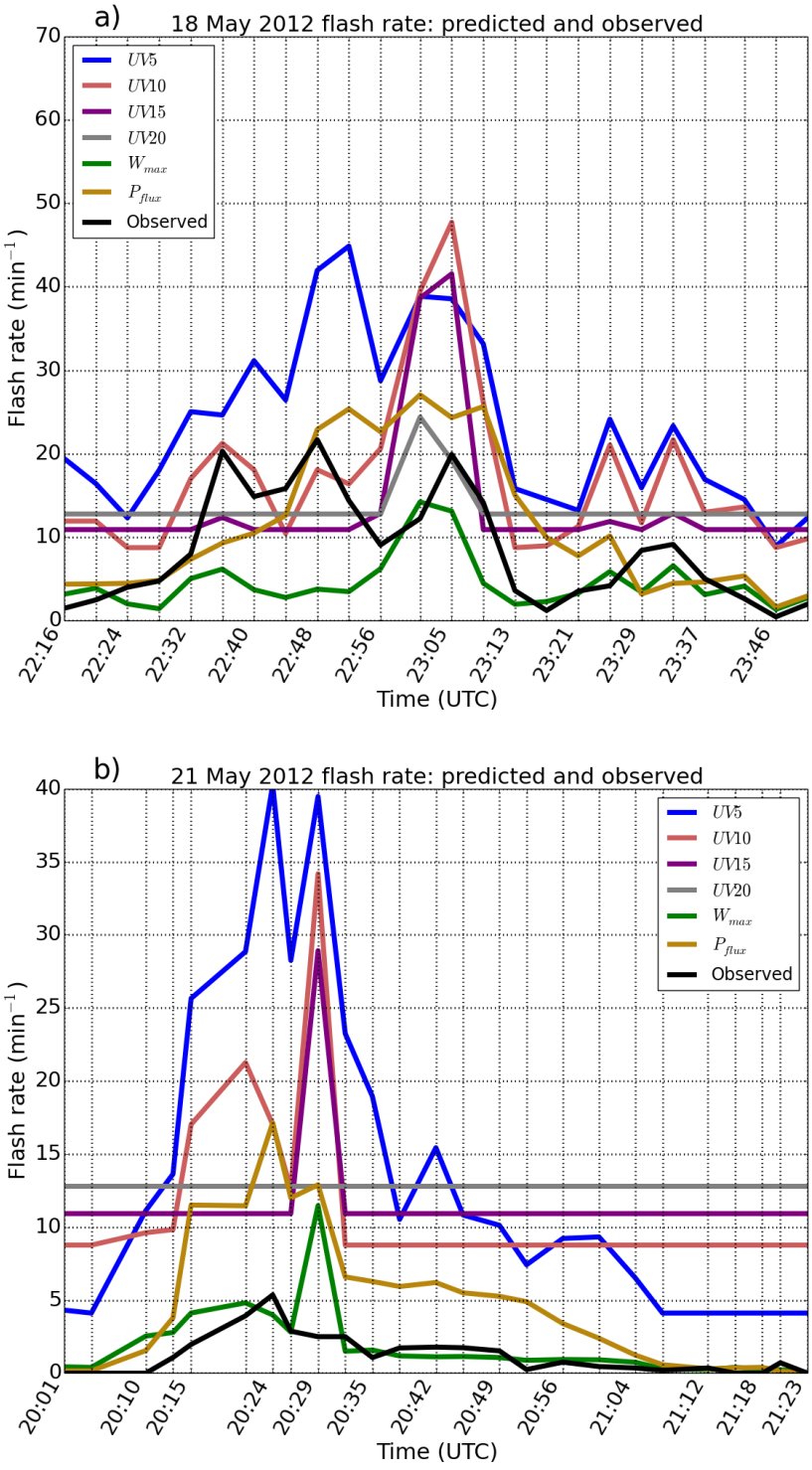

FIG. 3.22. Time series of observed total lightning flash rate (black) for a) 18 May 2012 and b) 21 May 2012 compared to flash rates predicted by parameterizations based on the updraft volume > 5 m s^{-1} (blue), > 10 m s^{-1} (pink), > 15 m s^{-1} (purple), and > 20 m s^{-1} (gray), the maximum updraft velocity (green), and the product of precipitating and non-precipitating ice mass flux (gold).

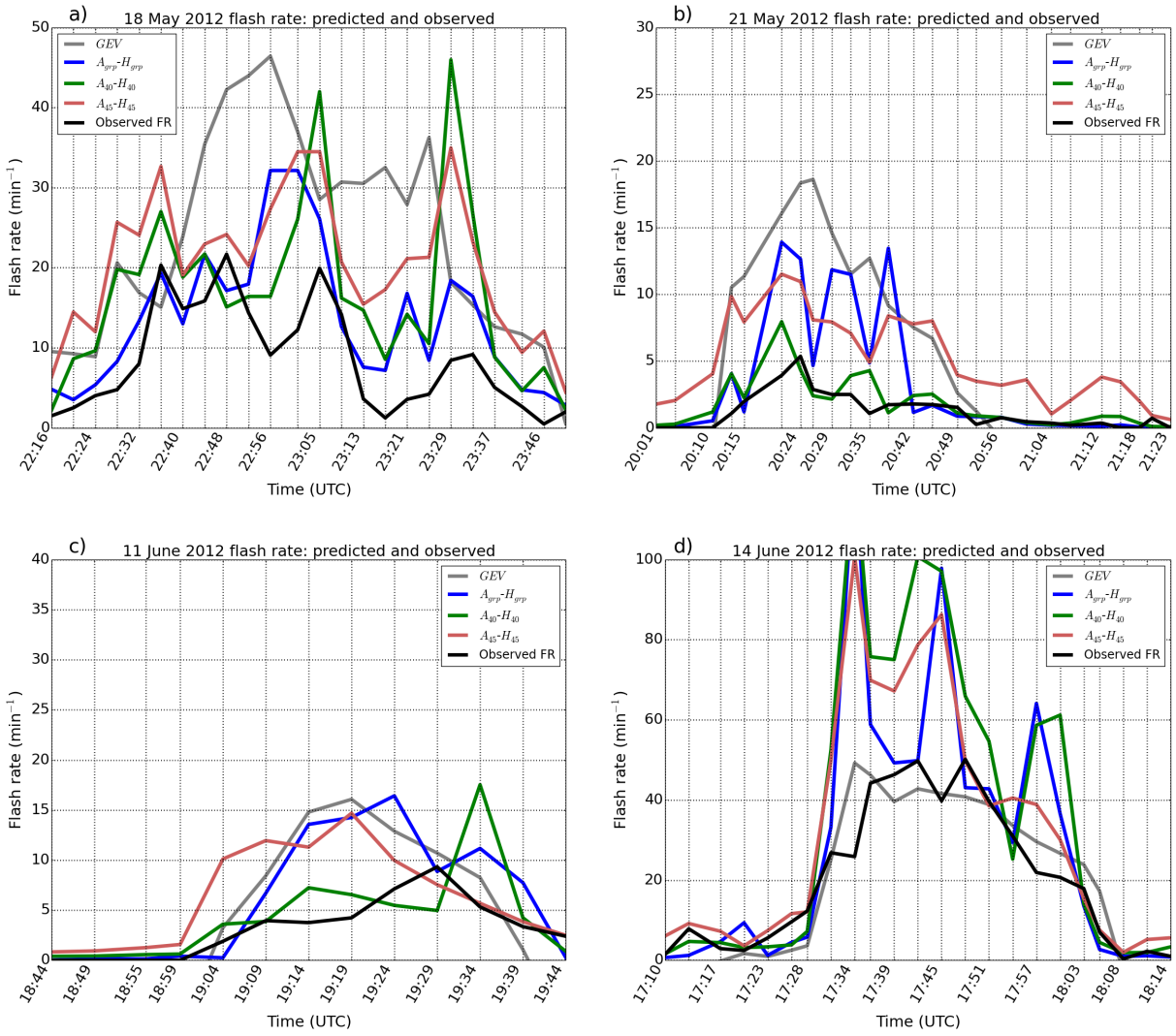

FIG. 3.23. Time series of observed total lightning flash rate (black) for a) 18 May 2012, b) 21 May 2012, c) 11 June 2012, and d) 14 June 2012 compared to flash rates predicted by parameterizations based on graupel echo volume (gray), maximum graupel area and graupel height (blue), 40-dBZ area and maximum height (green) and 45-dBZ area and maximum height (pink).

TABLE 3.1. Summary of flash rate parameterization schemes based on graupel echo volume, 30-dBZ echo volume, and precipitating ice mass within the mixed-phase region of the Colorado thunderstorms analyzed by this study. The first column lists the parameter used to predict flash rate and the second column lists the derived mathematical relationship between each parameter and flash rate (f). The final three columns list the coefficient of determination (R^2), root mean square error (RMSE), and normalized root mean square error (NRMSE) for each scheme.

Parameter used to predict flash rate (units)	Equation of Fit	Coefficient of Determination (R^2)	RMSE (min^{-1})	NRMSE
Graupel volume (km^3)	$f = (9.02 \times 10^{-2}) \times GEV - 11.38$	0.75	28.8	0.13
30-dBZ volume (km^3)	$f = (7.21 \times 10^{-2}) \times VOL30 - 8.98$	0.80	25.3	0.11
Precip. ice mass (kg)	$f = (1.68 \times 10^{-7}) \times PIM - 7.24$	0.80	25.7	0.11

TABLE 3.2. As in Table 3.1, but for flash rate parameterization schemes based on the updraft volume greater than 5, 10, 15, and 20 m s^{-1}, the maximum updraft velocity, and the product of precipitating and non-precipitating ice mass flux observed within the Colorado thunderstorms studied. Updraft volume and maximum updraft storm parameters were calculated only within the mixed phase region of storms.

Parameter used to predict flash rate (units)	Equation of Fit	Coefficient of Determination (R^2)	RMSE (min^{-1})	NRMSE
Updraft volume > 5 m s^{-1} (km^3)	$f = (1.00 \times 10^{-1}) \times UV5 + 4.12$	0.45	17.9	0.19
Updraft volume > 10 m s^{-1} (km^3)	$f = (2.12 \times 10^{-1}) \times UV10 + 8.77$	0.48	17.4	0.18
Updraft volume > 15 m s^{-1} (km^3)	$f = (4.86 \times 10^{-1}) \times UV15 + 10.92$	0.47	17.5	0.18
Updraft volume > 20 m s^{-1} (km^3)	$f = 1.29 \times UV20 + 12.79$	0.45	17.9	0.19
Maximum vertical velocity (m s^{-1})	$f = (8.60 \times 10^{-3}) \times W_{max}^{2.40}$	0.45	19.7	0.21
Ice mass flux product (kg^2 m s^{-2})	$f = (4.15 \times 10^{-8}) \times P_{flux}^{0.64}$	0.53	18.9	0.20

TABLE 3.3. As in Table 3.1, but for flash rate parameterization schemes based on the maximum graupel area and maximum graupel height, the 40-dBZ area and maximum height, and the 45-dBZ area and maximum height observed in the Colorado thunderstorms studied.

Parameter used to predict flash rate (units)	Equation of Fit	Coefficient of Determination (R^2)	RMSE (min^{-1})	NRMSE
Graupel area (km^2), graupel height (km)	$f = (6.27 \times 10^{-8}) \times A_{grp}^{1.02} \times H_{grp}^{5.76}$	0.82	25.7	0.11
40-dBZ area (km^2), 40-dBZ height (km)	$f = (1.29 \times 10^{-6}) \times A_{40}^{1.02} \times H_{40}^{4.85}$	0.78	27.2	0.12
45-dBZ area (km^2), 45-dBZ height (km)	$f = (1.90 \times 10^{-3}) \times A_{45}^{0.89} \times H_{45}^{2.41}$	0.65	24.9	0.11

CHAPTER 4

ANALYSIS AND DISCUSSION

4.1. VALIDITY OF FLASH RATE PARAMETERIZATIONS IN DIFFERENT ENVIRONMENTS

Several flash rate parameterization schemes have been developed. Though no single scheme predicts flash rate perfectly for all storms, many are generally successful. At the end of section 3.4, it was noted that very large flash rate peaks sometimes occurred for weaker Colorado storms with low flash rates in the mean. These flash rate maxima were usually not well predicted by bulk storm parameters. What other observables not represented by bulk storm quantities are important in regulating flash rate behavior? Could a certain parameterization be used selectively, if it is determined to work well for a particular storm type or environmental regime? Past studies have noted robust relationships between lightning activity and local environmental parameters (e.g. Williams et al. 2005), suggesting that the environment in which a storm develops is key to understanding its flash rate behavior. Fuchs (2014) found high flash rates to be strongly linked to large values of normalized convective available potential energy (NCAPE), where NCAPE is defined as CAPE divided by the height difference between the equilibrium level (EL) and the level of free convection (LFC) (Blanchard 1998). An environment with large NCAPE can support greater vertical acceleration at lower levels than a low-NCAPE environment, leading to stronger updrafts and increased lofting of SLW into the mixed-phase region of storms. Fuchs (2014) found the flash rate-NCAPE relationship to be significantly stronger than the flash rate-CAPE relationship.

In Figure 4.1, the NCAPE for each storm is plotted versus the surface-6 km vertical wind shear in the environment. Each point is colored by region and the size of each point represents the mean flash rate for that storm. The NCAPE-shear parameter space is demarcated by regions where the ice mass, echo volume, and/or the area-height schemes performed well, and where they tended to

incorrectly predict flash rate. Generally, storms in the upper-right quadrant of the NCAPE-shear space have flash rates well predicted by the schemes developed (6 June 2012 storm 2, 14 June 2012, 22 June 2012 storms 1 and 2, 17 June 2013, 3 August 2013). These storms are strong to severe storms with very high mean and maximum flash rates (Tables 2.1 and 2.2). In contrast, flash rates were overestimated for storms in the lower left quadrant (low NCAPE, low shear), which includes three of the four Alabama storms (18 May, 21 May, and 11 June 2012). For these storms, lower NCAPE likely contributed to weaker updrafts, less lofting of SLW into the mixed-phase region, and less lightning. It is therefore recommended that the ice mass/echo volume and area-height schemes be used only for storms with significant NCAPE (> 0.1 m s^{-2}) and vertical shear of at least 10 knots. Note that this condition does not exclude all storms in a single region, such as Alabama. The 14 June Alabama storm developed in an environment with nearly 0.2 m s^{-2} of NCAPE and 16 knots of shear, and its flash rates were predicted well, at least by the GEV scheme (Figure 3.21d).

The updraft volume schemes also overestimated flash rate for Alabama storms. The weaker Alabama storms studied appear capable of achieving broad regions of 5 m s^{-1} updrafts ($UV5$) comparable to the Colorado storms, but lack extreme updraft cores exceeding 15 m s^{-1} to produce very high flash rates (> 50 per minute). For this reason, one might expect maximum updraft speed (W_{max}) to be a more invariant measure of lightning activity across regions. Indeed, the peak updraft scheme does not systematically overestimate Alabama flash rates, as do the updraft volume schemes (Figure 3.22). However, the W_{max} scheme should be used with caution, since there was large scatter in the flash rate-W_{max} relationship (Figure 3.10a). The coefficient of determination (R^2) for this relationship was only 0.45, indicating that less than half of the total flash rate variability was explained by W_{max} alone.

There are exceptions to the successful prediction of flash rates by GEV, $VOL30$, and PIM in high NCAPE-high shear environments, including 6 June 2012 storm 1 (NCAPE = 0.18 m s^{-2}, shear = 29.6 knots), 22 June 2012 storm 2 (NCAPE = 0.26 m s^{-2}, shear = 47.5 knots), and 17 June 2013 (NCAPE = 0.12 m s^{-2}, shear = 12.6 knots). 6 June 2012 storm 1 may be an outlier storm that quickly moved into an unfavorable environment and decayed (this storm was tracked for less than one hour). In contrast to the much larger storms in the upper quadrant of Figure 4.1, 6 June storm 1 may have had insufficient time to become well organized and support large quantities of rimed ice mass. For 22 June 2012 storm 2, the ice mass/echo volume schemes overestimated flash rate. However, this storm's flash rates were better predicted by the area-height schemes. The area-height schemes predicted flash rates more accurately than the ice mass/echo volume schemes for 17 June 2013 as well.

The generally poor performance of the area-height flash rate schemes applied to low NCAPE-low shear storms (predominantly Alabama storms) warrants a comparison of storms from the Colorado and Alabama domains. While the Alabama storms exhibited weaker updrafts and much lower flash rates than their Colorado counterparts, observed maximum heights of graupel and reflectivity were similar. Figure 4.2 shows the maximum updraft velocity versus maximum height of graupel for all Alabama and Colorado storm volumes. Maximum updraft is a stronger function of maximum graupel height for the Colorado storms, meaning that the Alabama storms studied have weaker peak updrafts for similar graupel heights. Similarly, when total flash rates are plotted versus maximum graupel height (Figure 4.3), higher flash rates are produced in Colorado than Alabama for similar maximum graupel heights. Price and Rind (1992) analyzed a peak updraft-cloud

top height parameter space for continental versus oceanic thunderstorms and found similar qualitative differences between storms in these environments. The oceanic storms had similar cloud top heights to the continental storms but much weaker peak updrafts.

This echo height behavior of the Alabama storms can be understood by examining typical CAPE profiles for Colorado versus Alabama. Figure 4.4 shows an Alabama sounding from 11 June 2012 and a Colorado sounding from 6 June 2012. Whereas the CAPE in both soundings is comparable (1300 J kg^{-1} for Alabama versus 1700 J kg^{-1} for Colorado), the CAPE in the Colorado sounding is distributed over a smaller depth, resulting in nearly twice as much NCAPE. Environmental profiles similar to the 11 June 2012 sounding were observed for the 18 May and 21 May Alabama cases (but not 14 June). These narrow CAPE profiles allowed the Alabama storms to achieve high echo top heights, but their mixed-phase dynamics were weaker on account of weaker updraft accelerations, especially aloft. Figure 4.5 demonstrates the contrast in Colorado versus Alabama mixed-phase characteristics for the 18 May, 21 May, 6 June 2012 storm 2, and 6 June 2012 storm 3 cases. Updrafts for the Alabama storms on 18 and 21 May 2012 rarely exceeded 20 m s^{-1} while updrafts for 6 June 2012 storm 3 (a Colorado storm) exceeded 30 m s^{-1}. Mixed-phase reflectivity in the stronger 6 June Colorado storms exceeded 60 dBZ for significant periods of time. However, maximum heights of reflectivity upwards of 30-dBZ were comparable to the Alabama storms. Figures 4.4 and 4.5 suggest that flash rate schemes involving hydrometeor or dBZ maximum heights are not applicable across different regions with different thermodynamic environments. Price and Rind (1992) have recommended different cloud top height parameterizations for continental versus oceanic storms. That recommendation should be extended to continental storms that develop in significantly different environments. One may expect more inter-regional applicability for the A_{40}-H_{40} and A_{45}-H_{45} schemes, since Alabama storms tended to have lower

high-reflectivity maximum heights than their Colorado counterparts. Indeed, the A_{40}-H_{40} scheme predicted flash rate well for the 21 May and 11 June 2012 cases (Figure 3.23b and c). However, there was still large variability in the maximum height of 40- and 45-dBZ for the 18 May and 14 June 2012 Alabama cases. Additional case studies are necessary to confirm the possible applicability of the A_{40}-H_{40} and A_{45}-H_{45} schemes to storms in different regions.

Finally, there exists less certainty in the prediction of flash rate for moderate to low NCAPE and moderate shear storms, including the Colorado cases 6 June 2012 storms 3 and 4, 27 June 2012, and 28 June 2012. Whereas flash rates were well predicted by the ice mass/echo volume schemes for 6 June 2012 storm 4 (Figure 3.7a), the early flash rate peak observed for 6 June storm 3 (Figure 3.6d) was not predicted. Other dynamical and microphysical processes not considered by this study may be important in modulating electrical activity in low-NCAPE storms. Several low NCAPE-moderate shear storms had shallow warm cloud depths ($<$ 1 km for 6 June, 100 meters for 27 June, and zero for 28 June 2012). The lack of appreciable warm-cloud depth acts to suppress warm rain processes, allowing more supercooled liquid water into the mixed-phase region of storms and possibly enhancing cloud electrification (Williams et al. 2005). Even the relatively modest 26 per minute peak flash rate for the 28 June case was not characteristic of the peak updrafts in that storm, which did not exceed 20 m s^{-1}. The peak updraft flash rate scheme developed in this study predicts a flash rate of only 11 per minute for a 20 m s^{-1} peak updraft; the PR92W scheme predicts four flashes per minute. The area-height schemes underestimated peak flash rate for 28 June by at least 40 percent (Figure 3.17a).

The Colorado domain on 27 and 28 June was also characterized by extreme surface temperatures ($>$ 35°C) and a mixed-layer extending above 600-hPa. The high cloud bases characteristic of these conditions are thought to lead to wider mixed-phase updrafts with liquid water contents

closer to adiabatic values, which would also support more robust cloud electrification (Williams et al. 2005). It is therefore possible that additional environmental characteristics must be considered when using a particular lightning parameterization. However, based on the 15 cases analyzed by this study, there is low confidence for imposing further environmental constraints on the use of the flash rate parameterizations developed. The NCAPE and shear thresholds noted above for the use of the ice mass, echo volume, and area-height schemes should be considered by modeling studies. Future studies may wish to populate the NCAPE-shear parameter space with additional cases to better evaluate the environmental constraints that have been proposed.

4.2. IMPROVED PARAMETERIZATION OF LNO_X

A possible means to incorporate predicted flash rates into an improved LNO_x parameterization scheme is now discussed. In order to successfully parameterize LNO_x, a number of variables must be known or predicted. Many recent studies have made the assumption of constant NO_x production per CG flash, typically based on an assumed amount of NO_x produced per unit energy dissipated by a flash (section 1.1). A P_{IC}/P_{CG} ratio and assumed vertical distribution of IC and CG flashes is then used in order to prescribe LNO_x in cloud-resolving chemical transport simulations (e.g. DeCaria et al. 2005; Ott et al. 2010; Cummings et al. 2013). However, NO_x production per flash being insensitive to flash characteristics is suspect for several reasons. Wang et al. (1998) found that for a given peak current, NO_x production per unit discharge length was relatively constant for artificial laboratory sparks. In contrast, NO_x produced per unit energy dissipated was found to be more variable. The Wang et al. (1998) results suggest that the size of an individual lightning discharge may be an important control on NO_x produced. Physically, a bigger flash exposes more air to its superheated channel, thereby generating more NO_x. If total LNO_x produced within a

storm depends on the size of individual flashes, then predicting flash rate alone is insufficient to constrain NO_x production. A distribution of flash sizes must be known in addition to flash rate.

Fortunately, the LMA flash counting algorithm provides a means to calculate not only flash rate but also representative flash sizes (flash extents, see section 2.7). Bruning and MacGorman (2013) have put forward physical arguments and observational evidence for an anti-correlation between flash rate and a mean or representative flash extent. In Figure 4.6, the flash rate (black curve) is compared to a box-and-whisker times series showing the median (red lines) and interquartile range of flash extents (blue boxes) for 6 June 2012 storms 1 and 3. Flash extents, discussed in section 2.7, are interpreted as a representative flash size. The time series of non-precipitating ice mass (ice crystals and aggregates) is plotted in green. Both 6 June storms demonstrate an anti-correlation between flash rates and the median and range of flash extents. Non-precipitating ice mass peaks along with the increase in flash extent range and after the maximum in flash rate. Since non-precipitating ice was examined in regions of strong divergence aloft, it is reasonable to expect an increase in non-precipitating ice following a strong updraft pulse. As the updraft weakens following the pulse, bigger flashes are favored as opposed to small discharges occurring in the turbulent regions adjacent to strong updrafts (Bruning and MacGorman 2013). Non-precipitating ice may therefore be a useful parameter to track, or even parameterize, changes in flash extents. Carey et al. (2014) found a similar flash rate-flash extent anti-correlation and similar non-precipitating ice behavior in several Alabama thunderstorms.

The observed relationship between flash rate and flash extent was apparent to some degree for all cases, but the strength of the relationship was variable. The flash size distribution also appeared to be affected by changes in storm size. For example, storm mergers tended to accompany large increases in flash rate *and* flash extent range, since there were simply more flashes of all sizes.

However, it may not be necessary to predict a single flash extent quantity. Instead, if NO_x production depends most strongly on flash size (extent), then storm-total NO_x production should scale with the *total* flash extent summed over all flashes in the storm. Figure 4.7 shows the results of correlating total flash extent values in each storm volume to total flash rates. A robust *positive* correlation is observed, indicating that the total number of flashes strongly controls total flash extent. In light of this correlation, a NO_x parameterization may involve the following steps:

(1) Predict flash rate using a flash rate scheme based on bulk storm parameter(s)

(2) Use the observed correlation between flash rate and total flash extent (Figure 4.7) to determine a total flash extent for this predicted flash rate

(3) Multiply the total flash extent by a value of NO_x produced per unit channel length. Values of NO_x per channel length as a function of peak current are suggested by Wang et al. (1998) based on their studies of artificial sparks in the laboratory.

This relatively simple argument ignores the complications of the pressure dependence of NO_x production, and a characteristic flash peak current may still have to be assumed when applying a NO_x per unit channel length value (Wang et al. 1998). Additionally, flash extent is only a characteristic flash size; whether it is a consistent indicator of true flash channel length is uncertain, given the tortuous and intricately branched structure of observed lightning flashes (Hill 1968; Krehbiel et al. 2002). Once total NO_x is predicted, is must also be properly distributed within the storm, an important topic for future work. The loss of NO_x to downdrafts must be considered as well (Dye et al. 2000). Future studies could also compare values of total NO_x produced per channel length multiplied by total flash extent and the NO_x produced by assuming a fixed NO_x production per flash to evaluate assumptions of constant NO_x production per flash.

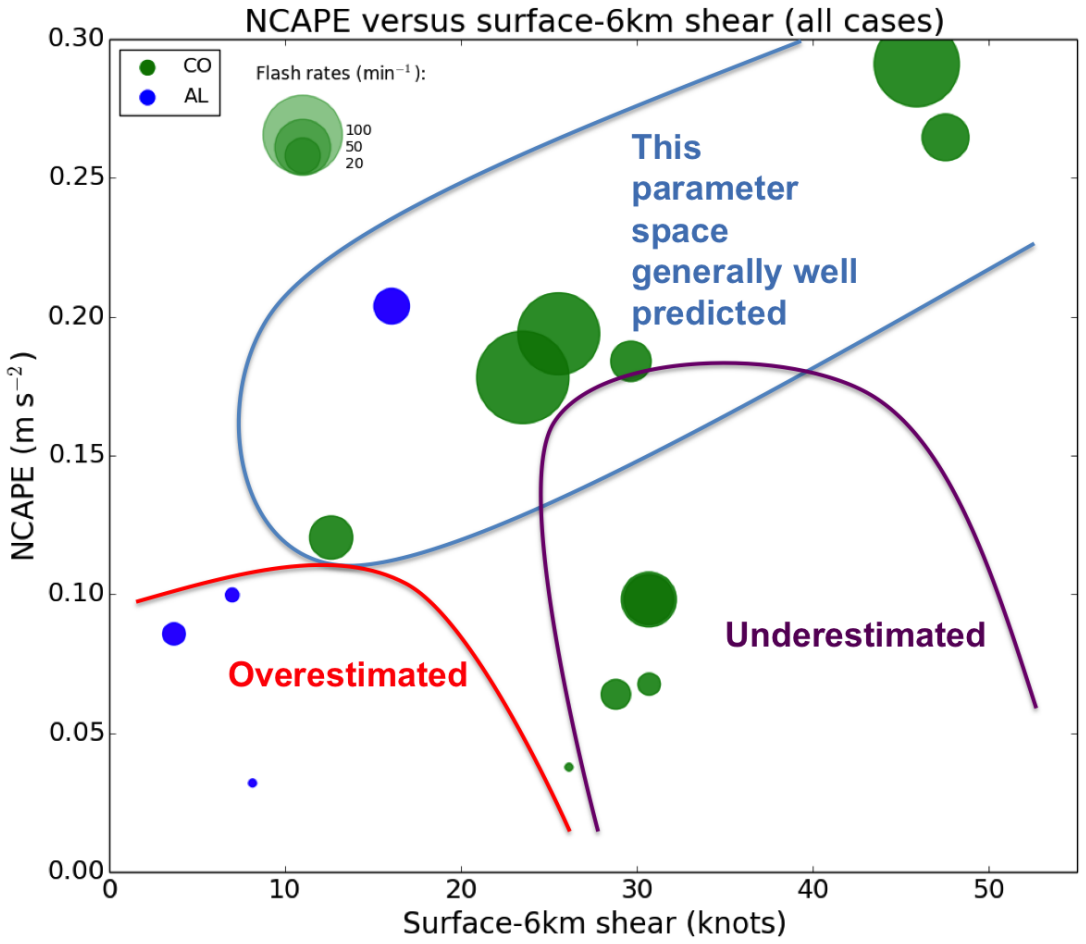

FIG. 4.1. Scatterplot of NCAPE versus surface-6 km vertical wind shear for each Colorado and Alabama case analyzed. The color of each point indicates the region (green for Colorado, blue for Alabama); the size of each point represents that storm's mean flash rate. The same NCAPE and shear values were used for 6 June 2012 storms 3 and 4 (NCAPE $= 0.1$ m s^{-2}, shear $= 30.7$ knots) because these storms developed nearly simultaneously and in a similar environment. These storms had similar mean flash rates, so their points overlap each other. The blue curve encloses points representing storms whose flash rates were predicted well (6 June 2012 storm 2, 14 June 2012, 22 June 2012 storms 1 and 2, 17 June 2013, and 3 August 2013). The red curve encloses storms whose flash rates were overestimated (18 May 2012, 21 May 2012, and 11 June 2012). The purple curve encloses storms whose (peak) flash rates were underestimated (6 June 2012 storms 1, 3, and 4, 27 June 2012, and 28 June 2012). The 5 June 2012 storm (NCAPE ~ 0.03 m s^{-2}, shear ~ 26 knots) lies between the "overestimated" and "underestimated" regions of the parameter space because its flash rates were overestimated only by some schemes.

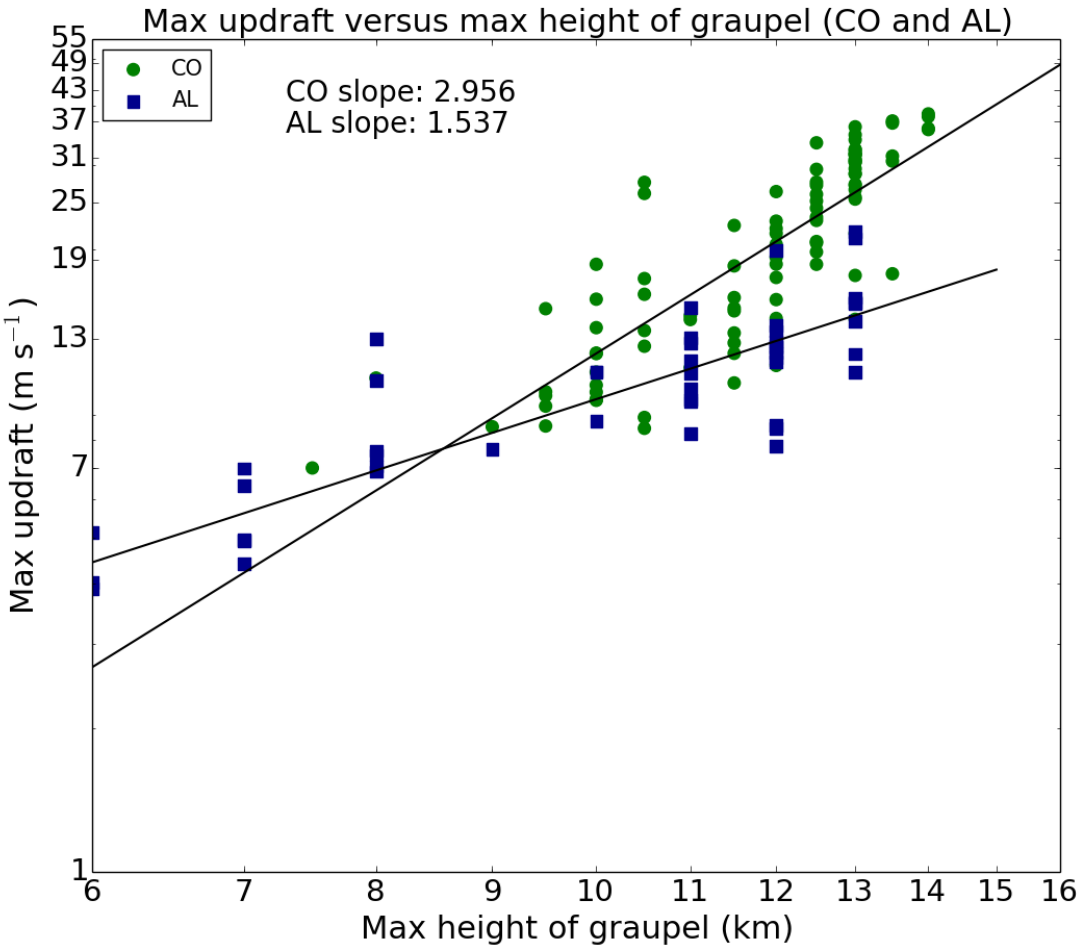

FIG. 4.2. Scatterplot of maximum updraft velocity versus maximum height of graupel for all storm volumes in Colorado (green circles) and Alabama (blue squares) for which the 3-D wind field was retrieved. The power-law fits for Colorado and Alabama are shown by the black curves. The slope of each fit is indicated as well.

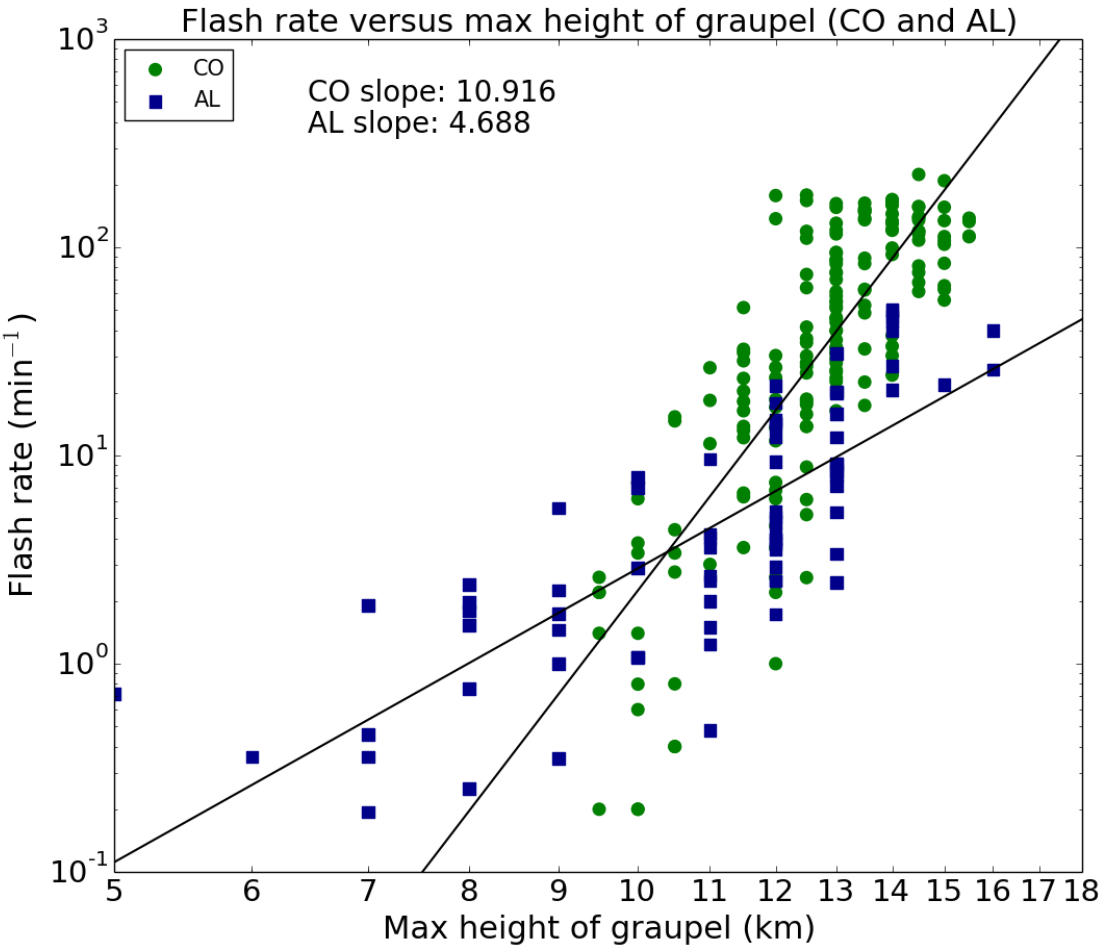

FIG. 4.3. Scatterplot of total lightning flash rate versus maximum height of graupel for all storm volumes in Colorado (green circles) and Alabama (blue squares). The power-law fits for Colorado and Alabama are shown by the black curves. The slope of each fit is indicated as well.

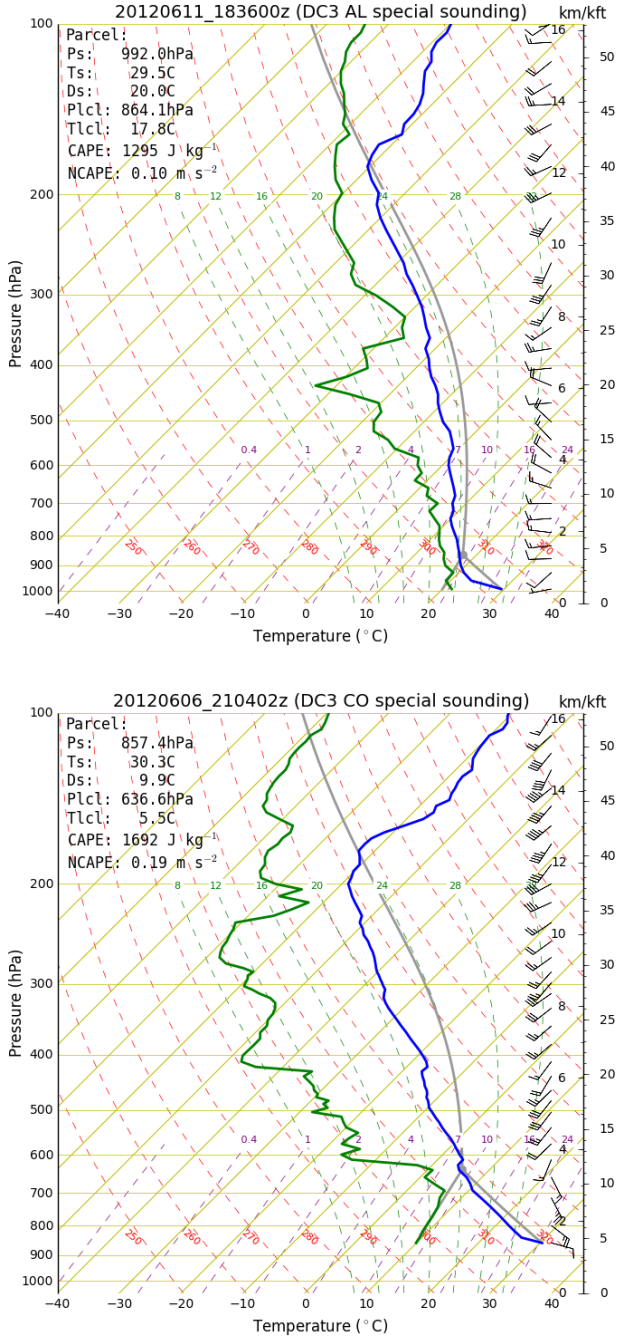

FIG. 4.4. SkewT-ln(P) plots of soundings taken on 11 June 2012, 18:36 UTC in Alabama (top) and 6 June 2012, 21:04 UTC in Colorado (bottom). The temperature and dewpoint profiles are indicated by the blue and green curves, and an idealized parcel path is indicated in gray. CAPE and NCAPE values for each sounding are indicated.

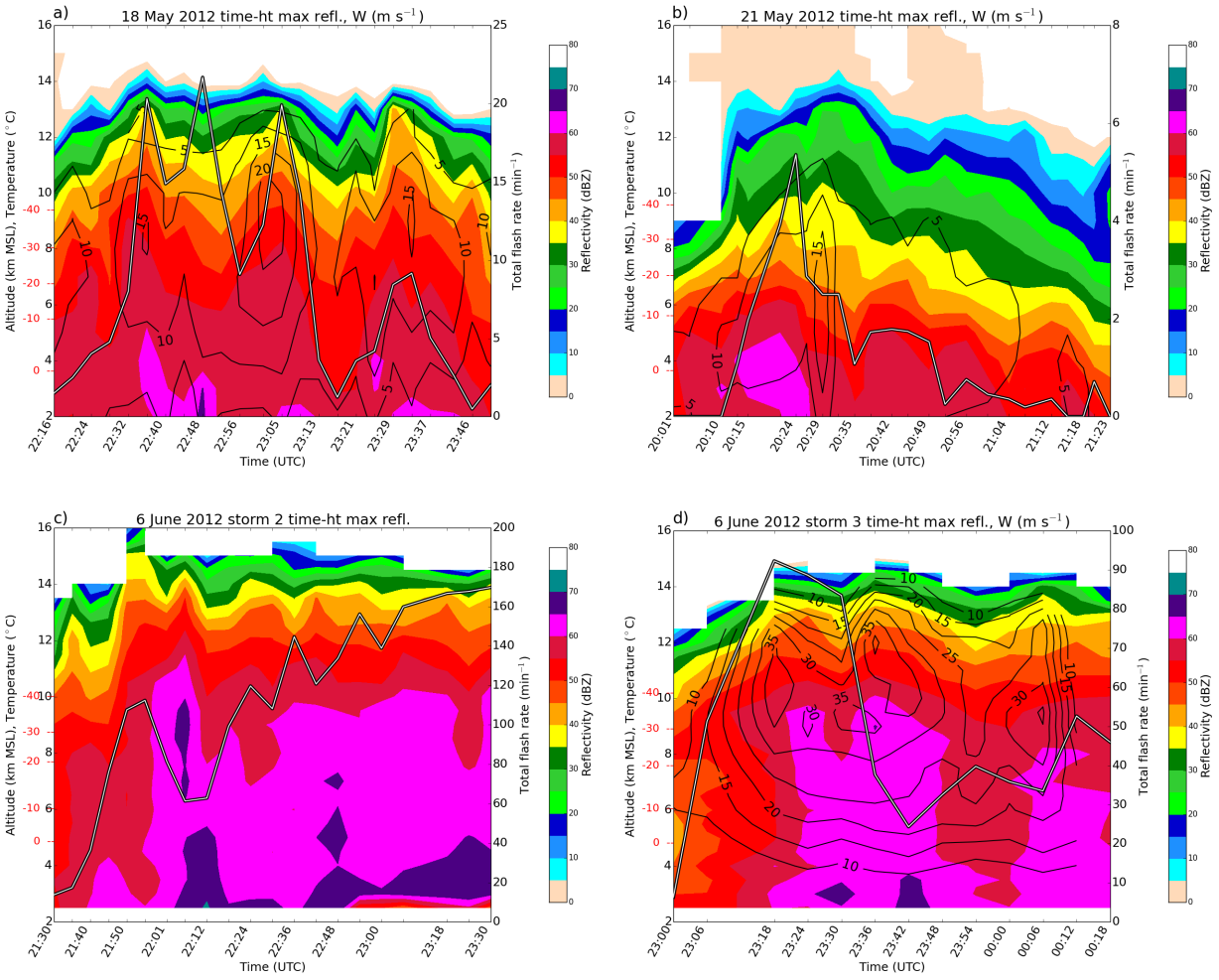

FIG. 4.5. Time-height maximum reflectivity and maximum updraft contour plots for a) 18 May 2012 (Alabama) b) 21 May 2012 (Alabama), c) 6 June 2012 storm 2 (Colorado) and d) 6 June 2012 storm 3 (Colorado). At each height and each time is plotted the maximum reflectivity (filled contours, color scale at right of each subplot), and the maximum updraft (black contours, labels every 5 m s^{-1}). Yellow contour is greater than 35 dBZ; magenta contour is greater than 60 dBZ. The vertical wind field was not retrieved for 6 June 2012 storm 2. The time series of total lightning flash rate (right axes) are indicated by the white curves outlined in black. Altitudes and sounding-derived temperature levels are provided on the left axes.

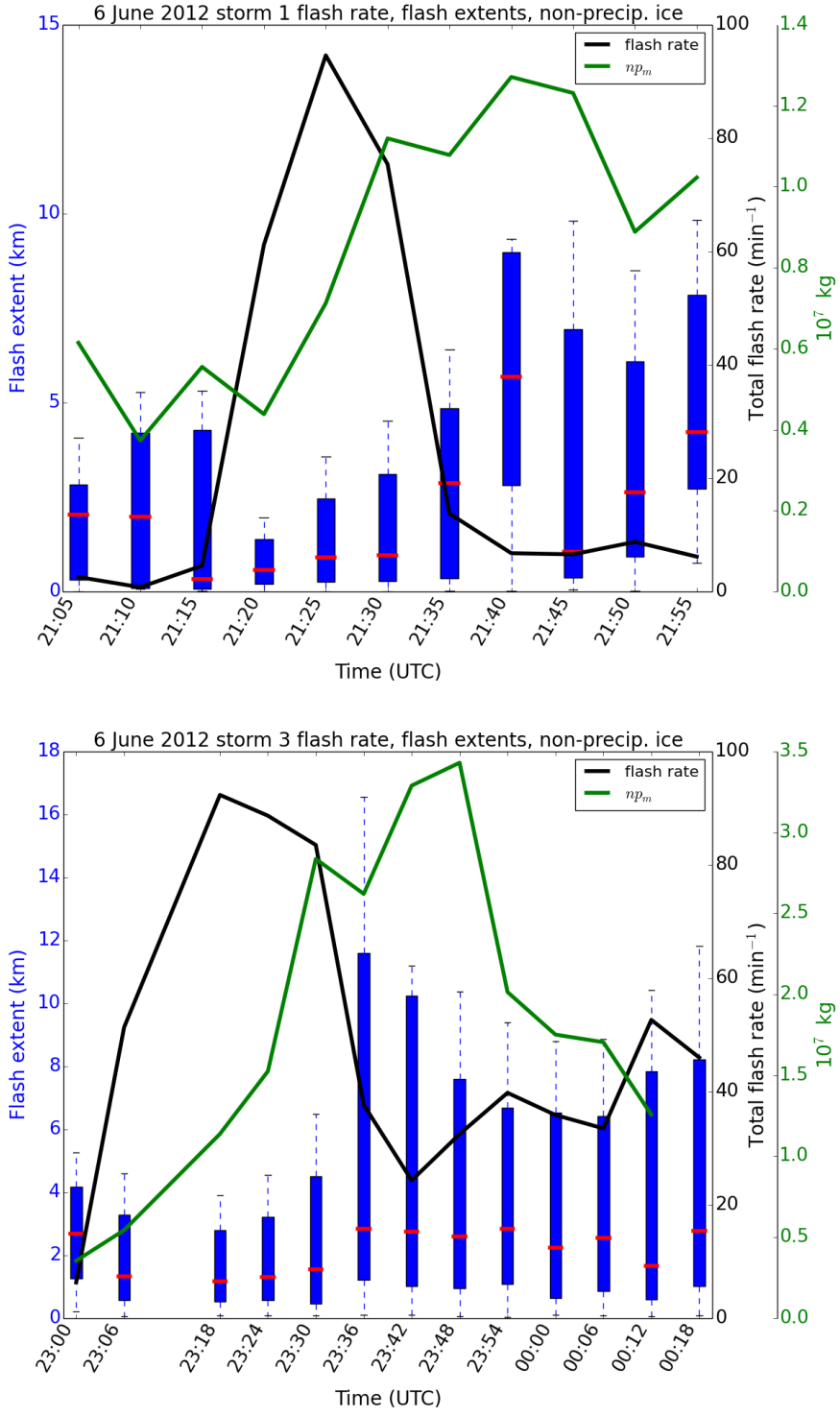

FIG. 4.6. Time series of total lightning flash rate (black), median flash extent (red lines) and interquartile range (IQR, blue boxes), and non-precipitating ice mass (green) for 6 June 2012 storm 1 (top) and 6 June 2012 storm 3 (bottom). The whiskers of each box-and-whisker plot extend to the most extreme flash extent observed within 0.5 times the IQR.

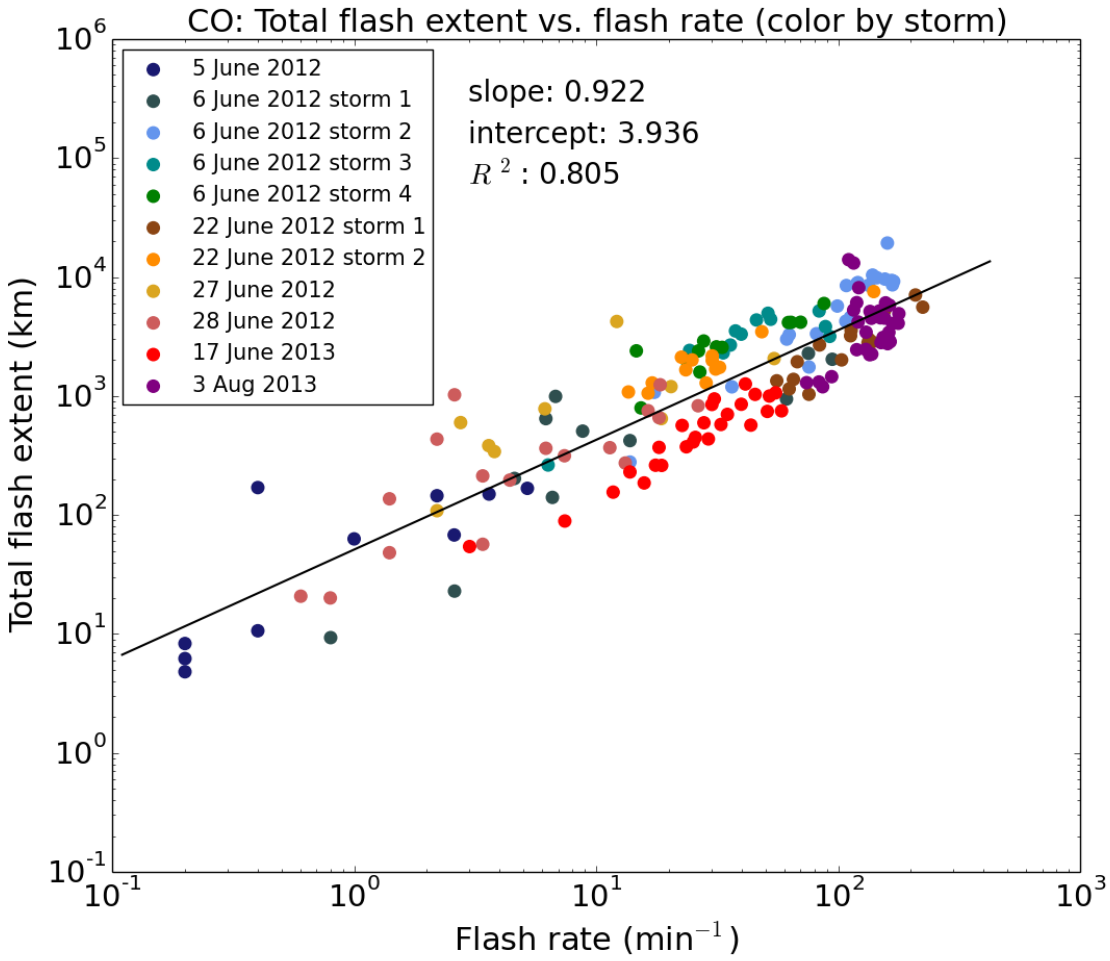

FIG. 4.7. Scatter plot of total lightning flash extent versus total flash rate for all Colorado storm volumes. Total flash extent is calculated by summing all the individual flash extents within a given storm volume. The least squares fit is shown by the black line. The slope and intercept as well as the R^2 value of the fit are indicated.

CHAPTER 5

SUMMARY AND CONCLUSIONS

This study developed several flash rate parameterization schemes based on the relationships between total lightning flash rate and bulk quantities representative of storm dynamics and microphysics. The flash rate parameterization schemes developed are intended for use in cloud-resolving chemical transport models, to aid in the prediction of LNO_x. Although no flash rate scheme worked equally well for all storms, the overall error of the best-performing schemes was between 11 and 12 percent. This study confirmed the work of earlier studies that simple, bulk storm parameters such as precipitating ice mass were reliable indicators of lightning activity. However, the coefficients of the relationships observed herein are different from the coefficients published in earlier work (e.g Deierling et al. 2008). Additionally, unique flash rate parameterizations based on multiple storm parameters have been proposed, and these schemes appear to predict flash rate variability better than single-parameter schemes. Finally, preliminary evidence was put forward suggesting that different flash rate parameterization schemes are necessary depending on a thunderstorm's environment, and an observed relationship between flash rate and total flash extent was discussed in terms of an improved LNO_x parameterization.

The flash rate schemes developed here appear ideally suited for thunderstorms occurring in the Central-High Plains of the United States, characterized by large NCAPE, substantial vertical wind shear, and high total flash rates. The flash rate parameterization schemes were able to successfully predict extreme flash rates exceeding 150 per minute that were occasionally observed in the Colorado storms analyzed. Impressively, the schemes were also able to predict periods of low flash rate activity in these Colorado storms (less than 20 per minute). However, for Alabama storms with similarly low flash rates, the schemes overestimated flash rate when compared to observations. It

was inferred that the Alabama storms studied had much weaker mixed-phase dynamics and microphysics than the Colorado storms, leading to less lightning. Although region-independent flash rate parameterizations are attractive from a modeling standpoint, region- or environment-specific schemes likely provide more accurate estimates of total flash rates. Carey et al. (2014) found that flash rate parameterizations developed using only Alabama data predicted flash rates generally well for Alabama storms. That study analyzed the same 18 May 2012 storm analyzed here. Flash rate schemes developed by Carey et al. (2014) based on the graupel echo volume, 30-dBZ volume, and graupel mass (similar to the precipitating ice mass used in this study) predicted the overall flash rate trend and magnitude well in contrast to the GEV, $VOL30$, and PIM schemes developed by this study. As expected, the Carey et al. (2014) parameterizations had different coefficients more suitable for the Alabama storms.

The parameterization schemes developed by this study did not predict flash rates well in Colorado storms with relatively weak dynamics (e.g., peak updraft speeds below 20 m s^{-1}) but vigorous lightning activity (peak flash rates exceeding 50 per minute). Generally speaking, these storms were characterized by low NCAPE and moderate vertical wind shear. Due to the incongruence of flash rate and storm parameter values, these storms' peak flash rates were underestimated. Notably, the large flash rate peaks in these storms were transient, lasting on the order of 10 minutes. Aside from brief flash rate peaks, these weaker storms had flash rates generally well predicted. The relatively limited sample size of this study precludes knowledge of whether weak storms commonly exhibit transient, high flash rates in Colorado. It is possible that the flash rate behavior observed in these storms was uncommon, and thus it is not necessary to consistently predict these storms' flash rates. Indeed, Fuchs (2014) found that over half of Colorado storms produced median flash rates

less than 10 per minute. However, if brief, large flash rate peaks in weaker storms are a frequent occurrence, then this weaker storm mode could contribute significantly to LNO_x.

Future studies should examine sub-gridscale processes to better understand the physical links between flash rate and dominant storm microphysical and dynamical processes. Processes not able to be represented by bulk storm parameters may be important in modulating flash rate. For example, is the majority of graupel inferred to be actively riming, or does it exist in largely glaciated regions, thereby reducing charging rates? A simple graupel echo volume is ignorant of such differences. High-resolution X-band polarimetric radar observations taken during the recent CHILL-MIE field project provide the ability to possibly classify the dominant processes occurring in and near thunderstorm updrafts. Kumjian et al. (2012) have begun work on inferring microphysical processes through a combination of polarimetric radar observations and modeling. Additional case studies from both DC3 and CHILL-MIE can also be used to further test the flash rate parameterizations developed by this study, and to further populate Figure 4.1 to understand the environmental constraints on certain flash rate schemes.

REFERENCES

Bain, A. L., 2013: Polarimetric Doppler radar and electrical observations of deep moist convection across northern Alabama during the Deep Convective Clouds and Chemistry Experiment, M.S. thesis, 148 pages, Department of Atmospheric Science, University of Alabama, Huntsville, AL.

Baker, B., M. B. Baker, E. R. Jayaratne, J. Latham, and C. P. R. Saunders, 1987: The influence of diffusional growth rates on the charge transfer accompanying rebounding collisions between ice crystals and soft hailstones. *Q.J.R. Meteor. Soc.*, **113**, 1193–1215.

Baker, M. B. and J. G. Dash, 1994: Mechanism of charge transfer between colliding ice particles in thunderstorms. *J. Geophys. Res.*, **99 (D5)**, 10 621–10 626.

Barth, M. C., et al., 2014: The Deep Convective Clouds and Chemistry (DC3) field campaign. *Bull. Amer. Meteor. Soc.*

Barthe, C., W. Deierling, and M. Barth, 2010: Estimation of total lightning from various storm parameters: A cloud-resolving model study. *J. Geophys. Res.*, **115 (D24202)**.

Benjamin, S. G., et al., 2007: From the radar-enhanced RUC to the WRF-based Rapid Refresh. *22nd Conf. Wea. Analysis Forecasting/ 18th Conf. Num. Wea. Pred.*

Blanchard, D. O., 1998: Assessing the vertical distribution of convective available potential energy. *Weather and Forecasting*, **13**, 870–877.

Boccippio, D. J., K. L. Cummins, H. J. Christian, and S. J. Goodman, 2001: Combined satellite- and surface-based estimation of the intracloud-cloud-to-ground lightning ratio over the continental United States. *Mon. Weather Rev.*, **129**, 108–122.

Bruning, E. C. and D. R. MacGorman, 2013: Theory and observations of controls on lightning flash size spectra. *J. Atmos. Sci.*, **70**, 4012–4029.

Bruning, E. C., S. A. Weiss, and K. M. Calhoun, 2014: Continuous variability in thunderstorm primary electrification and an evaluation of inverted-polarity terminology. *Atmospheric Research*, **135–136**, 274–284.

Carey, L. D., A. L. Bain, and R. Matthee, 2014: Kinematic and microphysical control of lightning in multicell convection over Alabama during DC3. *23rd International Lightning Detection Conference/5th International Lightning Meteorology Conference*.

Carey, L. D. and S. A. Rutledge, 1996: A multiparameter radar case study of the microphysical and kinematic evolution of a lightning producing storm. *Meteorol. Atmos. Phys.*, **59**, 33–64.

Carey, L. D. and S. A. Rutledge, 2003: Characteristics of cloud-to-ground lightning in severe and nonsevere storms over the central United States from 1989 to 1998. *J. Geophys. Res.*, **108 (D15)**.

Carey, L. D., S. A. Rutledge, and W. A. Petersen, 2003: The relationship between severe storm reports and cloud-to-ground lightning polarity in the contiguous United States from 1989 to 1998. *Month. Wea. Rev.*, **131**, 1211–1228.

Cressman, G. P., 1959: An operational objective analysis system. *Mon. Wea. Rev.*, **87**, 367–374.

Cummings, K. A., et al., 2013: Cloud-resolving chemistry simulation of a Hector thunderstorm. *Atmos. Chem. Phys.*, **13**, 2757–2777.

Davies-Jones, R. P., 1979: Dual-Doppler radar coverage area as a function of measurement accuracy and spatial resolution. *J. Appl. Meteor.*, **18 (9)**, 1229–1233.

DeCaria, A. J., K. E. Pickering, G. L. Stenchikov, and L. E. Ott, 2005: Lightning generated NO_x and its impact on tropospheric ozone production: A three-dimensional modeling study of a Stratosphere-Troposphere Experiment: Radiation, Aerosols, and Ozone (STERAO-A) thunderstorm. *J. Geophys. Res.*, **110 (D14303)**.

DeCaria, A. J., K. E. Pickering, G. L. Stenchikov, J. R. Scala, J. L. Stith, J. E. Dye, B. A. Ridley, and P. Laroche, 2000: A cloud-scale model study of lightning generated NO_x in an individual thunderstorm during STERAO-A. *J. Geophys. Res.*, **105 (D9)**, 11 601–11 616.

Deierling, W. and W. A. Petersen, 2008: Total lightning activity as an indicator of updraft characteristics. *J. Geophys. Res.*, **113 (D16210)**.

Deierling, W., W. A. Petersen, J. Latham, S. Ellis, and H. J. Christian, 2008: The relationship between lightning activity and ice fluxes in thunderstorms. *J. Geophys. Res.*, **113 (D15210)**.

Dolan, B. and S. A. Rutledge, 2009: A theory-based hydrometeor identification algorithm for X-band polarimetric radars. *J. Atmos. Oceanic Technol.*, **26**, 2071–2088.

Dolan, B., S. A. Rutledge, S. Lim, V. Chandrasekar, and M. Thurai, 2013: A robust C-band hydrometeor identification algorithm and application to a long-term polarimetric radar dataset. *J. Appl. Meteor. Climatol.*, **52**, 2162–2186.

Dye, J. E., et al., 2000: An overview of the Stratospheric-Tropospheric Experiment: Radiation, Aerosols, and Ozone (STERAO)-Deep Convection experiment with results for the July 10, 1996 storm. *J. Geophys. Res.*, **105 (D8)**, 10 023–10 045.

Ester, M., H.-P. Kriegel, J. Sander, and X. Xu, 1996: A density-based algorithm for discovering clusters in large spatial datasets with noise. *KDD-96 Proceedings*, 226–231.

Fehr, T., H. Holler, and H. Huntrieser, 2004: Model study on production and transport of lightning-producted NO_x in a EULINOX supercell storm. *J. Geophys. Res.*, **109 (D09102)**.

Fierro, A. O., E. R. Mansell, D. R. MacGorman, and C. L. Ziegler, 2013: The implementation of an explicit charging and discharge lightning scheme within the WRF-ARW model: Benchmark

simulations of a continental squall line, a tropical cyclone, and a winter storm. *Mon. Wea. Rev.*, **141**, 2390–2415.

Fuchs, B. R., 2014: Factors affecting lightning behavior in various regions of the United States, M.S. thesis, 174 pages, Department of Atmospheric Science, Colorado State University, Fort Collins, CO.

Giangrande, S. E., S. Collis, J. Straka, A. Protat, C. Williams, and S. Krueger, 2013: A summary of convective-core vertical velocity profiles using ARM UHF wind profilers in Oklahoma. *J. Appl. Meteor. Climatol.*, **52 (10)**, 2278–2295.

Heymsfield, A. J. and K. M. Miller, 1988: Water vapor and ice mass transported into the anvils of CCOPE thunderstorms: Comparison with storm influx and rainout. *J. Atmos. Sci.*, **45 (22)**, 3501–3514.

Hill, R. D., 1968: Analysis of irregular paths of lightning channels. *J. Geophys. Res.*, **73 (6)**, 1897–1906.

Holmes, C. R., M. Brook, P. Krehbiel, and R. McRory, 1971: On the power spectrum and mechanism of thunder. *J. Geophys. Res.*, **76 (9)**, 2106–2115.

Jayaratne, E. R., C. P. R. Saunders, and J. Hallett, 1983: Laboratory studies of the charging of soft-hail during ice crystal interactions. *Q.J.R. Meteor. Soc.*, **109**, 609–630.

Jourdain, L., S. S. Kulawik, H. M. Worden, K. E. Pickering, J. Worden, and A. M. Thompson, 2010: Lightning NO_x emissions over the USA constrained by TES ozone observations and the GEOS-CHEM model. *Atmos. Chem. Phys.*, **10**, 107–119.

Krehbiel, P. R., T. Hamlin, Y. Zhang, J. Harlin, R. Thomas, and W. Rison, 2002: Three-dimensional total lightning observations with the lightning mapping array. *2002 International Lightning Detection Conf.*

Krehbiel, P. R., R. J. Thomas, W. Rison, T. Hamlin, J. Harlin, and M. Davis, 2000: GPS-based mapping system reveals lightning inside storms. *EOS. Trans. AGU*, **81 (3)**, 21–32.

Kumjian, M. R., A. V. Ryzhkov, S. Tromel, and C. Simmer, 2012: Taking the microphysical fingerprints of storms with dual-polarization radar. *The Seventh European Conference on Radar in Meteorology and Hydrology*.

Lang, T. J. and S. A. Rutledge, 2002: Relationships between convective storm kinematics, precipitation, and lightning. *Mon. Wea. Rev.*, **130**, 2492–2506.

Lang, T. J. and S. A. Rutledge, 2011: A framework for the statistical analysis of large radar and lightning datasets: Results from STEPS 2000. *Mon. Wea. Rev.*, **139**, 2536–2551.

Lang, T. J., S. A. Rutledge, and K. C. Wiens, 2004a: Origins of positive cloud-to-ground lightning flashes in the stratiform region of a mesoscale convective system. *Geophys. Res. Lett.*, **31 (L10105)**.

Lang, T. J., et al., 2004b: The Severe Thunderstorm Electrification and Precipitation Study. *Bull. Amer. Meteor. Soc.*, **85**, 1107–1125.

Liu, S. C., M. Trainer, F. C. Fehsenfeld, D. D. Parrish, E. J. Williams, D. W. Fahey, G. Hubler, and P. C. Murphy, 1987: Ozone production in the rural troposphere and the implications for regional and global ozone distributions. *J. Geophys. Res.*, **92 (D4)**, 4191–4207.

Locatelli, J. D. and P. V. Hobbs, 1974: Fall speeds and masses of solid precipitation particles. *J. Geophys. Res.*, **79 (15)**, 2185–2197.

MacGorman, D. R., et al., 2008: TELEX: The Thunderstorm Electricity and Lightning Experiment. *Bull. Amer. Meteor. Soc.*, **89**, 997–1013.

McCaul, E. W., S. J. Goodman, K. M. LaCasse, and D. J. Cecil, 2009: Forecasting lightning threat using cloud-resolving model simulations. *Weather and Forecasting*, **24**, 709–729.

Mohr, C. G., L. J. Miller, R. L. Vaughan, and H. W. Frank, 1986: The merger of mesoscale datasets into a common Cartesian format for efficient and systematic analyses. *J. Atmos. Oceanic Technol.*, **3**, 143–161.

Ott, L. E., et al., 2010: Production of lightning NO_x and its vertical distribution calculated from three-dimensional cloud-scale chemical transport model simulations. *J. Geophys. Res.*, **115 (D04301)**.

Pickering, K. E., A. M. Thompson, R. R. Dickerson, W. T. Luke, D. P. McNamara, J. P. Greenberg, and P. R. Zimmerman, 1990: Model calculations of tropospheric ozone production potential following observed convective events. *J. Geophys. Res.*, **95 (D9)**, 14 049–14 062.

Pickering, K. E., Y. Wang, W.-K. Tao, C. Price, and J.-F. Muller, 1998: Vertical distributions of lightning NO_x for use in regional and global chemical transport models. *J. Geophys. Res.*, **103 (D23)**, 31 203–31 216.

Potvin, C. K., K. L. Elmore, and S. J. Weiss, 2010: Assessing the impacts of proximity sounding criteria on the climatology of significant tornado environments. *Weather and Forecasting*, **25**, 921–930.

Price, C., J. Penner, and M. Prather, 1997: NO_x from lightning: 1. Global distribution based on lightning physics. *J. Geophys. Res.*, **102 (D5)**, 5929–5941.

Price, C. and D. Rind, 1992: A simple lightning parameterization for calculating global lightning distributions. *J. Geophys. Res.*, **97 (D9)**, 9919–9933.

Rakov, V. A. and M. A. Uman, 2003: *Lightning: Physics and Effects*. Cambridge University Press.

Reynolds, S. E., M. Brook, and M. F. Gourley, 1957: Thunderstorm charge separation. *Journal of Meteorology*, **14**, 426–436.

Ridley, B., et al., 2004: Florida thunderstorms: A faucet of reactive nitrogen to the upper troposphere. *J. Geophys. Res.*, **109 (D17305)**.

Rinehart, R. E., 2010: *Radar for Meteorologists (fifth edition)*. Rinehart Publications.

Rison, W., P. R. Krehbiel, R. J. Thomas, D. Rodeheffer, and B. Fuchs, 2012: The Colorado lightning mapping array. *American Geophysical Union fall meeting, December 2012 (poster)*.

Rison, W., R. J. Thomas, P. R. Krehbiel, T. Hamlin, and J. Harlin, 1999: A GPS-based three-dimensional lightning mapping system: Initial observations in central New Mexico. *Geophys. Res. Lett.*, **26 (23)**, 3573–3576.

Saunders, C. P. R., W. D. Keith, and R. P. Mitzeva, 1991: The effect of liquid water on thunderstorm charging. *J. Geophys. Res.*, **96 (D6)**, 11 007–11 017.

Schumann, U. and H. Huntrieser, 2007: The global lightning-induced nitrogen oxides source. *Atmos. Chem. Phys.*, **7**, 3823–3907.

Seinfeld, J. H. and S. N. Pandis, 2006: *Atmospheric chemistry and physics: From air pollution to climate change (second edition)*. John Wiley and Sons, Inc.

Takahashi, T., 1978: Riming electrification as a charge generation mechanism in thunderstorms. *J. Atmos. Sci.*, **35 (8)**, 1536–1548.

Thomas, R. J., P. R. Krehbiel, W. Rison, J. Harlin, T. Hamlin, and N. Campbell, 2003: The LMA flash algorithm. *Proceedings of the 12th International Conference on Atmospheric Electricity, Versailles, France*, 655–656.

Thomas, R. J., P. R. Krehbiel, W. Rison, S. J. Hunyady, W. P. Winn, T. Hamlin, and J. Harlin, 2004: Accuracy of the lightning mapping array. *J. Geophys. Res.*, **109 (D14207)**.

Toumi, R., J. D. Haigh, and K. S. Law, 1996: A tropospheric ozone-lightning climate feedback. *Geophys. Res. Lett.*, **23 (9)**, 1037–1040.

Wallace, J. M. and P. V. Hobbs, 2006: *Atmospheric science: An introductory survey (second edition)*. Elsevier, Inc.

Wang, Y., A. W. DeSilva, and G. C. Goldenbaum, 1998: Nitric oxide production by simulated lightning: Dependence on current, energy, and pressure. *J. Geophys. Res.*, **103 (D15)**, 19 149–19 159.

Wiens, K. C., S. A. Rutledge, and S. A. Tessendorf, 2005: The 29 June 2000 supercell observed during STEPS. Part II: Lightning and charge structure. *J. Atmos. Sci.*, **62 (12)**, 4151–4177.

Williams, E. R., 1985: Large-scale charge separation in thunderclouds. *J. Geophys. Res*, **90 (D4)**, 6013–6025.

Williams, E. R., 1989: The tripole structure of thunderstorms. *J. Geophys. Res.*, **94 (D11)**, 13 151–13 167.

Williams, E. R., 1994: Global circuit response to seasonal variations in global surface air temperature. *Mon. Wea. Rev.*, **122**, 1917–1929.

Williams, E. R., 2005: Lightning and climate: A review. *Atmospheric Research*, **76**, 272–287.

Williams, E. R., V. Mushtak, D. Rosenfeld, S. Goodman, and D. Boccippio, 2005: Thermodynamic conditions favorable to superlative thunderstorm updraft, mixed phase microphysics and lightning flash rate. *Atmospheric Research*, **76**, 288–306.

Williams, E. R., R. Zhang, and J. Rydock, 1991: Mixed-phase microphysics and cloud electrification. *J. Atmos. Sci.*, **48 (19)**, 2195–2203.

Wilson, C. T. R., 1920: Investigations of lightning discharges and on the electric field of thunderstorms. *Philosophical transactions of the Royal Society of London*, **221**, 73–115.

Zhao, C., Y. Wang, Y. Choi, and T. Zeng, 2009: Summertime impact of convective transport and lightning NO_x production over North America: Modeling dependence on meteorological simulations. *Atmos. Chem. Phys.*, **9**, 4315–4327.